Ministry of Science, Research and Technology
**Institute for Color
Science &Technology**

Progress in Color, Colorants and Coatings

P

C

C

C

Progress in Color, Colorants and Coatings

The Progress in Color, Colorants and Coatings Journal is an international research peer reviewed Journal covers a wide range of the highly interdisciplinary field of color science and technogy, including (i) Color Imaging and Image Processing, (ii) Color Physics (Color Control and Measurement, Color Imaging and Color Image Processing), (iii) Environmental Aspect on Color and Coating Science and Technology, (iv) Ink and Printing Science and Technology, (v) Inorganic Pigments and Glazes including their applications, (vi) Novel Technologies in Color and Coating Science and Technology (Nano Technology, Bio Technology), (vii) Organic Colorants and Their applications, (viii) Resin and Additives, (ix) Surface Coatings & Corrosion (Materials / Applications), (x) Inorganic Coatings their applications, (xi) Outlook, Market and Technology Trend, (xii) Standardization.

Please follow the Instructure for Authors at www.pccc.icrc.ac.ir

In the Name of God

Progress in Color,
Colorants and Coatings

CONTENTS

Study on the Effect of Pomegranate Peel and Walnut Green Husk Extracts on the Antibacterial and Dyeing Properties of Wool Yarn Treated by Chitosan/Ag, Chitosan/Cu Nano-particles

M. Sadeghi-Kiakhani[*1], E. Hashemi[2]

[1.] Department of Organic Colorants, Institute for Color Science and Technology, P.O. Box: 16765-654, Tehran, Iran

[2.] Department of Chemistry, Faculty of Sciences, Shahid Rajaee Teacher Training University, P.O. Box: 16785-163, Tehran, Iran

ABSTRACT

*T*he growth of microorganisms on textiles can reduce mechanical properties, color changing, and disease spreading. Hence, natural antibacterial agents have developed dramatically and are important in the textile industry. In this study, the role of pomegranate peels and walnut green husk extracts on the antibacterial, dyeing, and fastness properties of wool yarn treated with chitosan-Cu and chitosan-Ag nanoparticles (Ch-Cu NPs and Ch-Ag NPs) are investigated. It was found that pomegranate peel and walnut green husk extracts could increase the antibacterial activities (almost 100 %) of samples in lower concentrations (1 % o.w.f.) treated with Ch-Cu and Ch-Ag NPs. Furthermore, the durability of the antibacterial activity of dyed samples was acceptable after 10 repeated washing times. Ag and Cu on the wool samples provided varied shades, which can be related to form complexation/coordination between them and natural dyes. The obtained results clearly showed that the extracts of used natural dyes could be proposed as the green method for decreasing the consumption of Ch-NPs, consequently, the costs of antibacterial finishing. Prog. Color Colorants Coat. 16 (2023), 221-229© Institute for Color Science and Technology.

1. Introduction

Research and development about natural antibacterial agents in the textile industry have attracted the attention of researchers [1, 2]. Many antibacterial agents such as copper naphthenate and numerous mercury compounds and formalin have been utilized in former that are nowadays firmly banned owing to their hazardous and toxicity potential for ecological [3, 4]. Metallic salts or oxides as alternate antibacterial agents have been used in textiles, but their danger to humans and aquatic life is still a problem [5, 6]. Also, the bioactivity of these materials on textiles is reduced substantially; therefore, more amounts are required to preserve their property [7]. The trend of research indicates that natural antibacterial agents have become more widely used. Various natural sources may be used as an alternative to conventional antibacterial agents for dyeing and finishing textiles [8, 9]. Simultaneous dyeing and finishing of textiles by natural antibacterial dyes can reduce production costs, water effluent, and environmental problems.

The walnut (*Juglans regia L.*) tree is cultivated in different regions of the world, and in terms of food, it has a very high consumption and is useful [10, 11]. 5-hydroxy-1,4-naphthoquinone is present in the fruits and leaves of this plant. This compound, with the original name C.I. Natural Brown 7, is a natural dye that can be used for dyeing of textiles [12, 13]. Many papers have

been reported about the extraction, dyeing, and different uses of a walnut shell. Various fibers can be dyed with this dye, and antibacterial and antioxidant activities have also been described in extracted species from this plant owing to high phenolic contents [14, 15].

Pomegranate is a small tree named (*Punica granatum*) in the family *Lythraceae*, a native plant of Iran and nearby regions, and its height varies between 5 and 10 meters. Pomegranate peel is a waste of fruit juice processing. They can be used as natural colorants with antioxidant, anticarcinogenic, and antibacterial activities due to the presence of flavonoids and polyphenols and alkaloids such as N-methyl granatonin [16, 17]. Pomegranate peel has various uses in different fields and textile dyeing. Also, different textiles can be dyed with the antibacterial and antioxidant activities of pomegranate peel [18-20].

Chitosan, a biopolymer, is obtained from chitin as the second natural polysaccharide after cellulose [21, 22]. The unique properties of chitosan, such as antibacterial, biodegradability, and non-toxicity, have led to the development of its various applications. It is possible to enhance the inherent properties of chitosan by grafting different metal/metal oxides and generating novel functionalities on it [23, 24]. The antibacterial activity of chitosan can improve 10-20-fold by metals, so silver ions increase the antibacterial activity of chitosan up to 20-fold other than chitosan [25].

Natural dyes are green materials that increase the antibacterial efficiency of chitosan on textile fibers [26, 27]. Shin et al. reported that the dye uptake and antibacterial activity were increased with the increase in chitosan concentration. Chitosan pretreatment effectively develops eco-friendly, functional, natural-dyed blend fabrics [28]. The cotton fabric successfully printed with natural dyes in fine powder form using chitosan as an eco-friendly mordant [29]. The chitosan showed good colorimetric data and antibacterial activity in the printed samples [30]. The combination of chitosan and henna dye was studied by Bhuiyan et al. They suggested that the antibacterial activity of jute fiber against the bacteria can considerably improve by chitosan and henna dye [31]. These outcomes recommend that the use of chitosan and natural dye from henna onto jute fiber is an approach to get the desired dyeing and antibacterial property.

In this study, the treated samples with Ch loaded by Cu and Ag ions were dyed with extracts of walnut green husks and pomegranate peels as two natural

dyes. Moreover, the antibacterial activities, durability, colorimetric data, and color fastness of treated samples against wash and light were investigated.

2. Experimental

2.1. Material and methods

AgNO$_3$ and Cu$_2$O were purchased from Merck Co. (Germany). Mahtani Chitosan PVT LTD Chitin India supplied chitosan with molecular weight>600kD and a degree of deacetylation of 98 %. The walnut green husks and pomegranate peels were provided from a local dyeing workshop in Ardakan (Iran). The chemical structures of colorants in the mentioned dyes are given in Figure 1. The wool yarns with the specification of 200Tex/4fold were scoured with nonionic detergent (Lotensol, Hansa). The other solvents and chemicals were analytical grade and utilized without any purification.

2.2. Wool treatment

The synthesis, characterization, and application of Ch-Cu and Ch-Ag NPs on the wool yarns have been reported in detail in our previous paper [32, 33]. Briefly, various concentrations of AgNO$_3$ and Cu$_2$O salts (1, 5, and 10 % o.w.f.) were prepared in 30 mL water containing citric acid (4 % o.w.f.) and sodium hypophosphite (4 % o.w.f.) at pH 4. Then, the wool sample (1 g) was added to the prepared solution and was shaken at 120 rpm at 50 °C for 2 h. Finally, the samples were rinsed and dried at room temperature.

2.3. Antibacterial test

A quantitative test AATCC 100-2004, was used to evaluate the bacterial reduction of dyed samples against gram-positive *S.aureus* and gram-negative *E.coli* bacteria. In summary, samples were autoclaved at 121 °C for 15 min. 100 μL of prepared suspension of bacteria (10^6 bacteria) was added into 10 mL prepared nutrient broth and incubated at 37±2 °C for 18 h. The reduction percent in the number of bacterial colonies of the wool samples was calculated by Eq. 1:

$$Antibacterial\ effect\ (\%) = \frac{A - B}{A} \times 100 \qquad (1)$$

Where A is the number of bacteria colonies in the solution containing the wool sample, and B is the number of bacteria colonies in the solution containing the dyed samples.
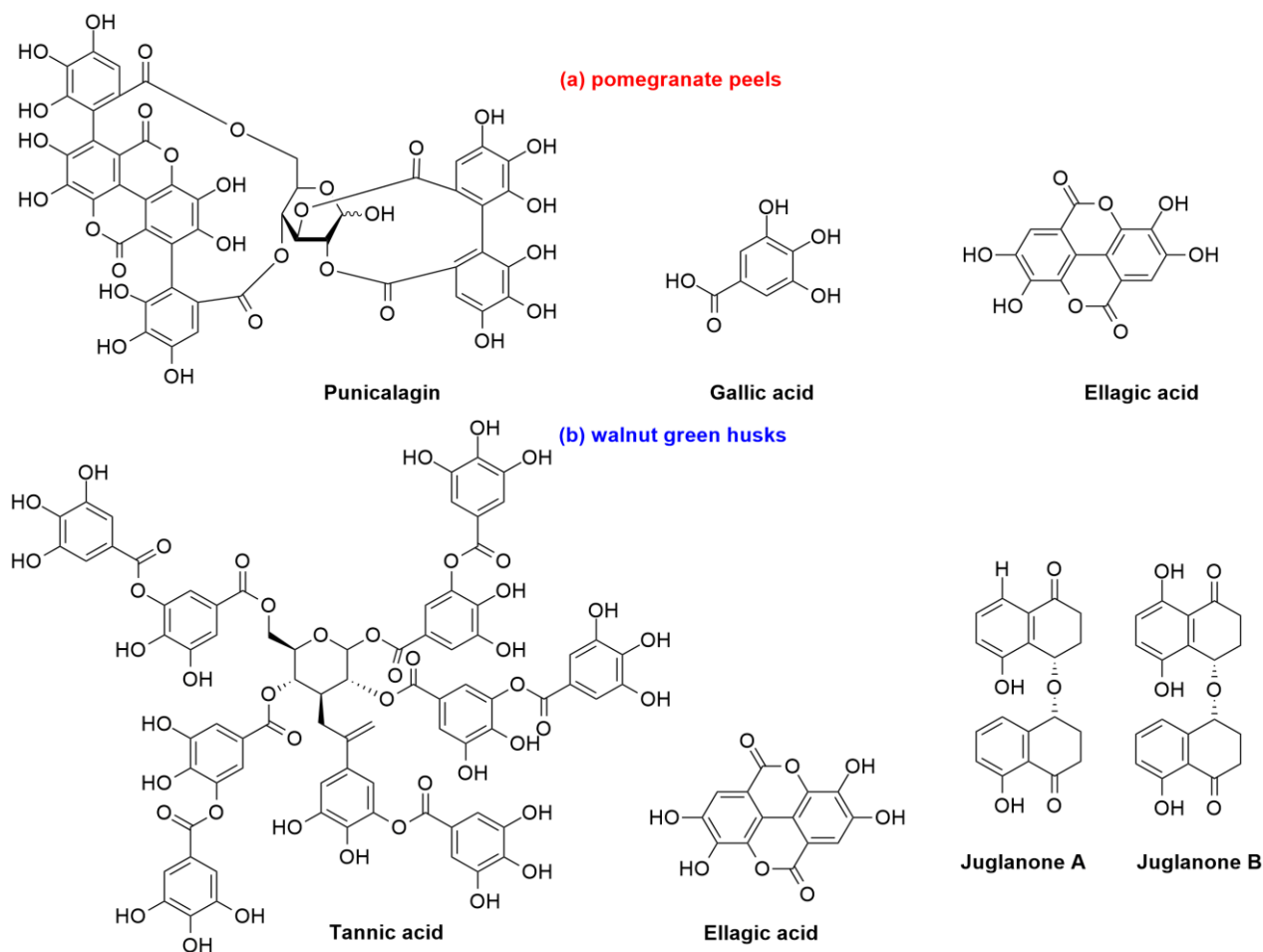
Figure 1: The chemical structure of colorants in the (a) pomegranate peels and (b) walnut green husks.

2.4. Dyeing procedure

The walnut green husks and pomegranate peels were extracted in 30 % o.w.f. Concentration through the conventional method at boiling temperature for 2h. All samples were dyed with acetic acid at 100 °C for 60 minutes at a liquor ratio of 1:40, at a pH of 5 [32]. Finally, dyed samples were washed and dried.

A reflective spectrophotometer used to determine the colorimetric analysis of dyed samples through the Kubelka-Munk function (Eq. 2).

$$\frac{K}{S} = \frac{(1-R)^2}{2R} \tag{2}$$

Where K and S are the absorbance and scattering coefficients, respectively. R is the reflectance ratio at maximum absorbance wavelength. The measurements were performed at three places on the sample, and their averages were reported.

2.5. Color fastness

The wash fastness of dyed samples was determined by ISO 105 C06 C2S:1994 (E) manner. The dyed samples were placed between a piece of undyed wool and cotton adjacent fabrics so that three samples were stitched together to form composite specimens. The samples were washed at 60 °C for 30 min, then rinsed and dried at room temperature. The grey scales were used for measurements. The rates of 1 and 5 indicate severe staining and no staining on adjacent fabrics, respectively.

The xenon arc lamp considered the fastness to light of dyed samples via the standard ISO 105 B02:1988 (E). The samples and eight standard patterns of the blue wool fabric of various light fastness ratings were placed inside the light fastness tester. The samples were evaluated after 100 h of exposure to a xenon lamp so that the rates of 1 and 8 indicate weak and excellent light fastness of dyed samples, respectively.

3. Results and Discussion

3.1. FTIR analysis

Figure 2 shows the FTIR spectra of natural dyes and untreated, treated wool fibers. In Figure 2a, the O-H stretching and C=C or C=O functional groups of polyphenols in natural dyes were observable in the range of 3300 cm^{-1} and 1630-1640 cm^{-1}, respectively [28, 30]. Also, a peak at 1024-1041 cm^{-1} corresponds to C-O-C vibration in natural dyes [32, 33]. Colorants available in pomegranate peel and walnut husk extracts are shown in Figure 1. Many -O.H., C=O, -C-C-, -C-H- bonds, and -C=C- aromatic rings are visible in the spectra. The FTIR spectra showed that the obtained data are consistent with the previously reported results [14, 26].

FTIR spectroscopy of raw and treated wool samples is shown in Figure 2b. Results showed a strong peak at 3400 cm^{-1}, related to the wool's different amines and hydroxyl functional groups. The C-H stretching vibration peak at 2923 cm^{-1} confirmed the presence of -CH$_2$ groups of wool samples. The polypeptides and proteins have various amide peaks, usually 1600-1700 cm^{-1} [26, 28]. Since the functional groups in chitosan and woolen yarn are similar and the amount of Ch-Ag and Ch-Cu NPs used is insignificant (5 % o.w.f.), the FTIR spectrum of treated samples is not much different from raw woolen yarn. However, the difference in the intensity of the peak and the presence of new peaks in the spectra of the treated wool sample can indicate the presence of Ch-Ag and Ch-Cu NPs on the wool yarn.

3.2. Antibacterial activity of wool yarn

The effects of natural dye extracts and Ch-NPs on the antibacterial activity of wool samples are shown in Table 1. Results indicated that bacterial growth was significantly inhibited as the concentration of Ch-NPs increased. Since both chitosan and NPs are each antibacterial alone, Ch-NPs hybrids have an acceptable antibacterial activity, which can be related to disrupting the nutrient to cells via interactions of cell membranes with the positively charged of Ch-NPs producing the reactive oxygen species (ROS). Consequently, the growth of the cells stops [33-35]. The highest antibacterial activity belongs to treated wool yarns with Ch-Ag, and the higher amounts are attained by increasing Ch-NPs. Results indicated that suitable antibacterial activities were obtained in 5 % o.w.f. of Ch-NPs, and this concentration was chosen as the optimal amount for wool modification.
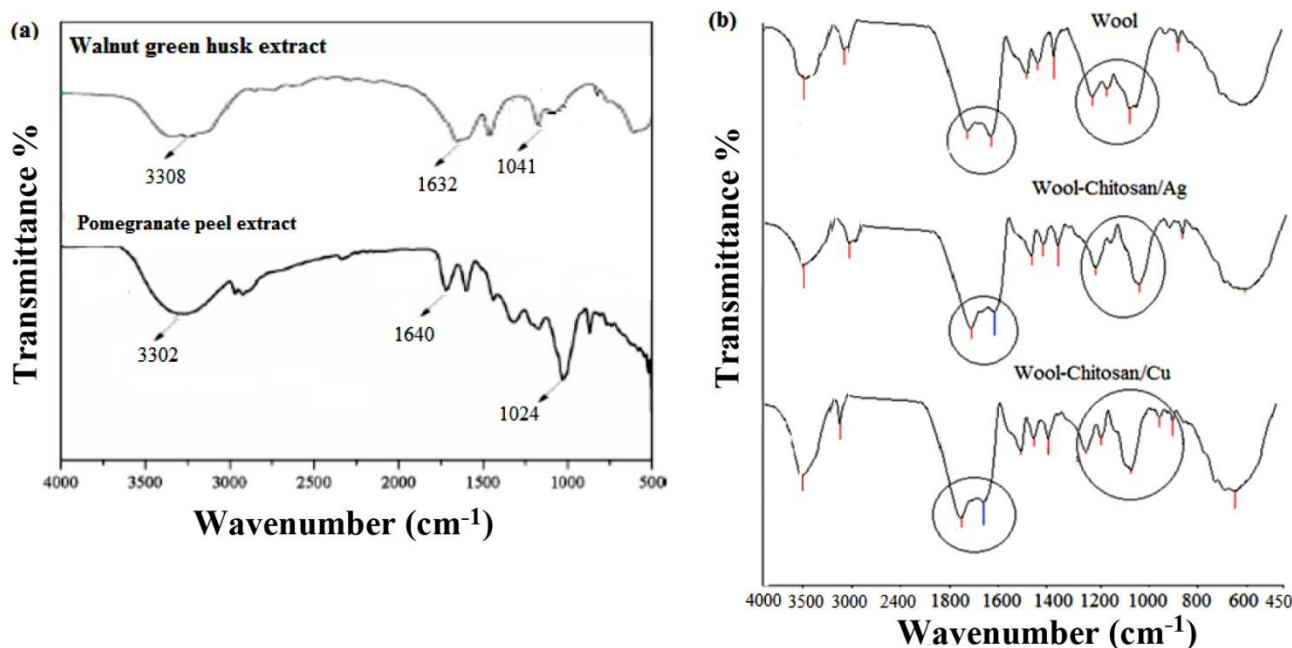

Figure 2: The FTIR spectra of (a) natural dyes and (b) untreated and treated wool samples.

Table 1: Antibacterial activity of wool samples treated by Ch-NPs at various concentrations.

Sample	%(o.w.f.)	Antibacterial activity (%)					
		Un-dyed samples		Walnut		Pomegranate	
		E. coli	*S.aureus*	*E. coli*	*S.aureus*	*E. coli*	*S.aureus*
Wool	-	-	-	63.33	55.19	70.65	64.72
Wool-Ch -Ag	1	36.11	32.08	80.40	74.17	87.68	81.41
	5	100	100	100	100	100	100
	10	100	100	100	100	100	100
Wool-Ch -Cu	1	74.61	71.81	79.27	72.38	80.16	75.32
	5	75.04	71.70	100	100	100	100
	10	80.90	74.63	100	100	100	100

Because of high ellagitannins, polyphenols, gallic acid, ellagic acid, and some flavonoids, walnuts, and Pomegranates have good antibacterial activity [14, 15, 19, 20]. Results indicated that dyeing of wool-treated samples with Walnut and Pomegranate improved the reduction of bacteria to 63 and 70 % against *E. Coli* bacterium, respectively. The obtained data against *E. Coli* bacterium were relatively better than *S. aureus* because the cell wall structures of the two bacteria are diverse, and *E. Coli* has an outer layer comprising lipopolysaccharide, which inhibits the diffusion of the antibacterial agent via the cell wall. Therefore, the most natural sources hardly kill the external membrane of the gram-negative bacterium [15, 20]. Results indicate that the dyeing of wool yarn with both natural dyes can reach higher antibacterial activities by decreasing the consumption of Ch-Cu NPs. It is possible to produce antibacterial wool yarn via a cheaper and greener process.

In Table 2, the antibacterial of wool samples was studied against repeated washing via ISO 6330-1984 standard. The washing durability of Ch-NPs on the wool fibers is affected by the strength of bonding between them. The samples dyed with walnut green husks and pomegranate peels and treated with Ch-NPs exhibited less than 10 % decrease in antibacterial activity after 10 repeated washing cycles. Furthermore, the antibacterial values of undyed samples diminished to 5-25 % after repeated washing cycles. Results showed that the antibacterial activity of dyed samples with natural dyes improved against repeated washing times, which can be related to the more and stronger linkages between the Ch-NPs-natural dyes-wool yarn systems [35, 36]. The antibacterial activities were reduced by ~ 8 % and ~25 % when Ch-Ag and Ch-Cu were used, respectively. The citric acid as a cross-linking agent in the grafting process can improve the durability of Ch-NPs on the wool samples, and the antibacterial activity was preserved. Indeed, the antibacterial activities can reduce without using citric acid [15].

Table 2: The antibacterial durability of treated samples against repeated washings.

Sample	Repeated Washing Cycles	Antibacterial activity (%)					
		Un-dyed samples		Dyed with *Walnut*		Dyed with pomegranate	
		E. coli	*S.aureus*	*E. coli*	*S.aureus*	*E. coli*	*S.aureus*
Ch-Ag	-	100	100	100	100	100	100
	5	98.40	97.31	98.40	97.31	98.51	97.06
	10	95.60	92.57	95.60	92.57	94.67	93.42
Ch-Cu	-	100	100	100	100	100	100
	5	91.81	88.80	91.81	88.80	93.06	88.90
	10	86.36	82.23	86.36	82.23	92.77	84.54

3.3. The color strength and coordinates

The colorimetric data of dyed samples with two natural dyes and treated with the Ch-NPs are shown in Table 3. a* and b* of all samples have been changed after dyeing with walnut and pomegranate. So, some samples have a different hue. The large color difference (ΔE^*) confirmed the obtained results and indicated that the treatment was effective on the final color of the samples. The color change of the dyed samples shows that a complexation/coordination bond has been established between the dye and the wool treated with Ch-NPs [37, 38]. So, it can be mentioned that no significant variation was observed in K/S values of dyed samples via these treatments, but it was possible to produce the different hues on the wool samples (Table 4). The proposed mechanism for the interaction of wool fiber and natural dyes is shown in Scheme 1. Ch-NPs can be attached to the wool via physical adsorption or chemical bonding. Also, various active sites in the protein chains of the wool fibers can improve the linkages of Ch-NPs on the wool. As a result, the number of dye absorptive sites on the wool increases, and more dye molecules can be absorbed into the treated samples [39, 40].

3.4. Color fastness properties

Table 4 shows the color fastness rates of dyed samples with natural dyes against wash and light. The wool dyed with both natural dyes has moderate wash fastness (3) and good light fastness (5-6). The rates of color fastness of dyed samples pretreated with Ch-NPs improved and were acceptable. So, treated samples with Ch-NPs showed excellent light fastness, which was improved to 7 rates. Also, The more linkages between natural dyes and Ch-NPs on the wool samples cause to increase in the washing fastness [38, 40].

Table 3: Colorimetric data of dyed samples with natural dyes and treated by Ch-NPs concentration 5 % o.w.f.

Dye	treated with	Before dyeing process					After dyeing process				
		L^*	a^*	b^*	K/S	ΔE^*	L^*	a^*	b^*	K/S	ΔE^*
Walnut	-	37.65	8.32	17.78	11.216	-	37.65	8.32	17.78	11.216	–
	Ch-Ag	33.07	9.34	17.743	15.820	24.24	30.85	9.8	19.523	16.690	16.27
	Ch-Cu	32.42	9.42	17.776	16.860	29.02	27.90	9.143	17.86	24.280	8.38
Pomegranate	-	62.82	5.91	17.78	7.785	-	62.82	5.91	17.78	7.785	–
	Ch-Ag	40.22	5.977	21.697	12.510	12.64	56.69	7.1	26.07	13.070	7.44
	Ch-Cu	55.16	5.726	24.906	11.400	14.88	56.41	7.58	27.036	13.650	7.86

Table 4: Colorfastness of dyed samples and treated with 5 % o.w.f. of Ch-NPs.

Dye	Sample	Treatment before dyeing				Treatment after dyeing			
		Light fastness	Wash fastness			Light fastness	Wash fastness		
			CC^*	SW^*	SC^*		CC^*	SW^*	SC^*
Walnut	-	5-6	3	4	4	5-6	4	4	4
	Ch-Ag	8	5-4	5-4	5-4	7	4	5-4	5-4
	Ch-Cu	7-8	5-4	4-5	4-5	7	4-5	4-5	5
Pomegranate	-	6	3-4	4	4-5	6	4	4	5
	Ch-Ag	6	5-4	5	5-4	6-5	4	5-4	4
	Ch-Cu	6	4-5	4-5	4-5	6-5	4	4-5	4-5
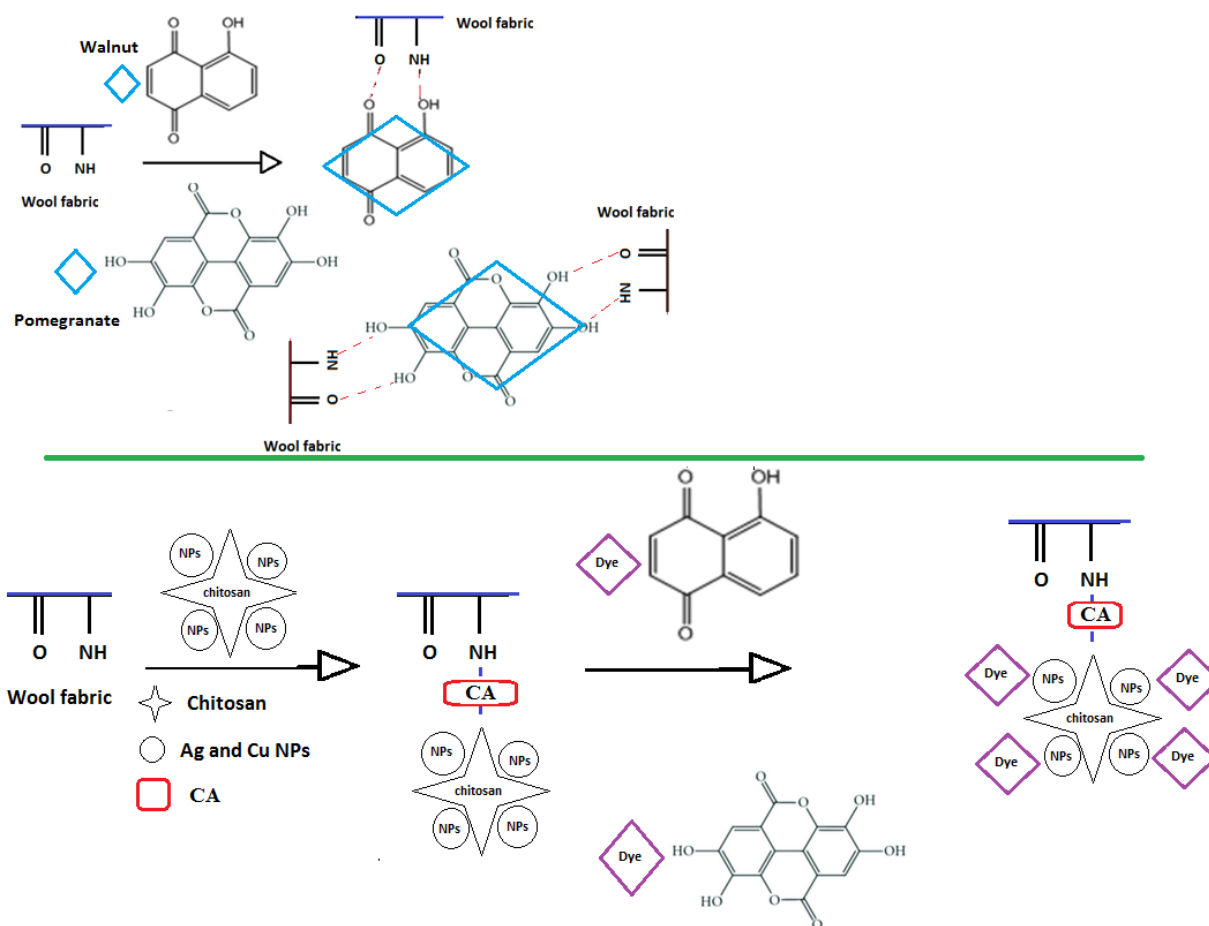
Scheme 1: The proposed mechanism for the interaction of wool fiber and natural dyes.

4. Conclusions

The antibacterial wool yarn was produced via an eco-friendly method using extracts of walnut green husks and pomegranate peels and Ch-Ag and Ch-Cu NPs. The wool yarns treated with Ch-NPs increase the inhibition of bacteria. The antibacterial activity of treated samples with Ch-Ag NPs and dyed by walnut husk was above 95 % against *E.coli* after 10 repeated washing times. In addition to producing acceptable antimicrobial activity on the wool, this treatment improves the color absorption of pomegranate peel and walnut husk extract by up to 6 and 13 units, respectively. It may be due to the increase in the number of absorptive dye sites on the wool, and consequently, more dye molecules can be absorbed in the treated samples. The color fastness properties of wool samples were enhanced after treatment with Ch-NPs, which can be related to the more and stronger linkages between natural dyes-Ch-NPs-wool fibers system. This study's results clearly showed that walnut green husks and pomegranate peels could raise the antibacterial activity of wool yarns treated by Ch-NPs So, the antibacterial of the sample was treated with 10 % o.w.f. Ch-NPs was 70-80 %, while natural dye extracts can increase the antibacterial; activities up to 100 % at the concentration of 5 % o.w.f. of Ch-NPs. So, the consumption of Ch-NPs for antibacterial finishing is reduced, and the antibacterial finishing of the wool yarns can be performed via an economical and green technique.

5. References

1. B. Tawiah, W. Badoe, and S. Fu, Advances in the development of antimicrobial agents for textiles: The quest for natural products. Review, *Fibres Text. East. Eur.*, 24(2016), 3-136.

2. N. Afraz, F. Uddin, U. Syed, and A. Mahmood, Antimicrobial finishes for textiles, *Curr Trends Fashion Technol Textile Eng*, 4(2019), 87-94.

3. G. Shalini, and D. Anitha, Antimicrobial property of textiles. *Int. J. Sci. Res.*, 5(2016), 766-768.

4. A. Reshma, V.B. Priyadarisini, and K. Amutha, Sustainable antimicrobial finishing of fabrics using natural bioactive agents-a review, *Int. J. Life Sci. Pharma Res*, 8(2018), 10-20.

5. N. Iheaturu, B. Aharanwa, K. Chike, U. Ezeamaku, O. Nnorom, C. Chima, O. Nnorom, advancements in textile finishing, *J. Polymer. Text. Eng.*, 6(2019), 23-31.

6. A. Haji, S. Ashraf, M. Nasiriboroumand, C. Lievens , Environmentally friendly surface treatment of wool fiber with plasma and chitosan for improved coloration with cochineal and safflower natural dyes, *Fibers Polym.*, 21(2020), 743-750.

7. A. L. Mohamed, A.G. Hassabo, S. Shaarawy, A. Hebeish, Benign development of cotton with antibacterial activity and metal sorpability through introduction amino Triazole moieties and agnps in cotton structure pre-treated with periodate, *Carbohydr. Polym.*, 178(2017), 251-259.

8. D. Radhika, Review study on antimicrobial finishes on textiles-plant extracts and their application, *Int Res J Eng Technol.*, 6(2019), 3581-3588.

9. P. Pandit, M.D. Teli, G.T. Nadathur, green synthesis of nanoparticle and its application on cotton fabric using sterculia foetida fruit shell extract, *J. Text. Eng. Fash. technol.*, 6(2020), 257-265.

10. T. Bechtold, R. Mussak, Handbook of natural colorants, John Wiley & Sons, New York, NY, USA, 2009.

11. A. Fernández-Agulló, E. Pereira, M.S. Freire et al., Influence of solvent on the antioxidant and antimicrobial properties of walnut (*Juglans regia L.*) green husk extracts, *Ind Crops Prod*, 42(2013), 126-132,.

12. F. Shahmoradi Ghaheh, A. Shams Nateri, S.M. Mortazavi, D. Abedi, J. Mokhtari, The effect of mordant salts on antibacterial activity of wool fabric dyed with pomegranate and walnut shell extracts, *Color. Technol.*, 128(2012), 473-478.

13. H. Han, S. Wang, M. Rakita, Y. Wang, Q. Han, Q. Xu, Effect of ultrasound-assisted extraction of phenolic compounds on the characteristics of walnut shells, *Food Nutr. Sci.*, 9(2018), 1034-1045.

14. M. Sadeghi-Kiakhani, A. R. Tehrani-Bagha, K. Gharanjig, E. Hashemi, Use of pomegranate peels and walnut green husks as the green antimicrobial agents to reduce the consumption of inorganic nanoparticles

on wool yarns, *J. Clean. Prod.*, 231(2019), 1463-1473.

15. V. Raja, S. I. Ahmad, M. Irshad, WA Wani, WA Siddiqi, S. Shreaz, Anticandidal activity of ethanolic root extract of *Juglans regia (L.)*: Effect on growth, cell morphology, and key virulence factors, *J. Mycol. Méd.*, 27(2017), 476-486.

16. E. H. Papaioannou, S. T. Mitrouli, S. I. Patsios, M. Kazakli, A.J. Karabelas, Valorization of pomegranate husk-Integration of extraction with nanofiltration for concentrated polyphenols recovery, *J. Environ. Chem. Eng.*, 8(2020), 103951.

17. C. Harscoat-Schiavo, B. Khoualdia, R. Savoire, S. Hobloss, C. Buré, B.A. Samia, P. Subra-Paternault, Extraction of phenolics from pomegranate residues: Selectivity induced by the methods, *J. Supercrit. Fluids.*, 176(2021), 105300.

18. K. Kaderides, L. Papaoikonomou, Melania Serafim, Athanasia M. Goula Microwave-assisted extraction of phenolics from pomegranate peels: Optimization, kinetics, and comparison with ultrasounds extraction, *Chem. Eng. Process.: Process Intensif.*, 137(2019), 1-11.

19. S. Talekar, A.F. Patti, R. Singh, R. Vijayraghavan, A. Arora, From waste to wealth: High recovery of nutraceuticals from pomegranate seed waste using a green extraction process, *Ind Crops Prod*, 112(2018), 790-802.

20. B. Singh, J.P. Singh, A. Kaur, N. Singh, Phenolic compounds as beneficial phytochemicals in pomegranate (*Punica granatum L.*) peel: A review, *Food Chem.*, 261(2018), 75-86.

21. O. Sauperl, M. Kostic, J. Milanovic, L. Fras Zemljic, Chemical Binding of Chitosan and Chitosan Nanoparticles onto Oxidized Cellulose, *J. Eng. Fibers Fabrics*, 10(2015), 70-77.

22. F. Ahmadi, Z. Oveisi, S.M. Samani et al. Chitosan based hydrogels: characteristics and pharmaceutical applications, *Res Pharm Sci.*, 10(2015), 1-16.

23. A. Hebeish, S. Sharaf, A. Farouk, Utilization of chitosan nanoparticles as a green finish in multifunctionalization of cotton textile, *Int. J. Biol. Macromol.*, 60(2013), 10-17.

24. Y. Gökçe, B. Cengiz, N. Yildiz, A. Calimli, Z. Aktas, Ultrasonication of chitosan nanoparticle suspension: influence on particle size, *Colloid. Surf. A: Physicochem. Eng. Aspects*, 462(2014), 75-81.

25. S.W. Ali, S. Rajendran, M. Joshi, Synthesis and characterization of chitosan and silverl chitosan nanoparticles for bioactive polyester, *Carbohydr. Polym.*, 83(2011), 438-446.

26. M. Sadeghi-Kiakhani; S. Safapour; Y. Golpazir, Impact of chitosan-poly(amidoamine) dendreimer hybrid treatment on dyeing and color fastness properties of wool yarn with Madder Natural Dye, *Prog. Color. Colorant Coat*, 12(2019), 241-250.

27. L. Mehrparvar, S. Safapour, M. Sadeghi-Kiakhani, K. Gharanjig, A cleaner and eco-benign process for wool dyeing with madder, *Rubia tinctorum L.*, root natural dye, *Int. J. Environ. Sci. Technol.* 13(2016), 2569-2578.

28. V. R. Giri Dev, J. Venugopal, S. Sudha, G. Deepika, S. Ramakrishna, Dyeing and antimicrobial characteristics of chitosan treated wool fabrics with henna dye, *Carbohydr. Polym.*, 75(2009), 646-650.

29. M. Sadeghi-Kiakhani, A. R. Tehrani-Bagha, S. Safapour, Enhanced anti-microbial, anti-creasing and dye absorption properties of cotton fabric treated with chitosan-cyanuric chloride hybrid, *Cellulose*, 25(2018), 883-893.

30. S. Safapour, M. Sadeghi-Kiakhani, S. Doustmohammadi, Chitosan-cyanuric chloride hybrid as an efficient novel bio-mordant for improvement of cochineal natural dye absorption on wool yarns, *J. Text. Inst.*, 110(2019), 81-88.

31. M. Sadeghi-Kiakhani, H. Tayebi, Eco-friendly reactive dyeing of modified silk fabrics using corona discharge and chitosan pre-treatment, *J. Text. Inst.*, 108(2017), 1164-1172.

32. M. Sadeghi-Kiakhani, E. Hashemi, K. Gharanjig, Treating wool fibers with chitosan-based nano-composites for enhancing the antimicrobial properties, *Appl. Nanosci.*, 10(2020), 1219-1229.

33. L. Mehrparvar, S. Safapour, M. Sadeghi-Kiakhani, K. Gharanjig, Chitosan-polypropylene imine dendrimer hybrid: a new ecological biomordant for cochineal dyeing of wool, *Environ. Chem. Lett.*, 14(2016), 533-539.

34. S. Govindan, E. A. K. Nivethaa, R. Saravanan, V. Narayanan, A. Stephen, Synthesis and characterization of chitosan-silver nanocomposite, *Appl. Nanosci.*, 2(2012), 299-303.

35. A.S. Wazed, S. Rajendran, M. Joshi, Synthesis and characterization of chitosan and silver loaded chitosan nanoparticles for bioactive polyester, *Carbohydr. Polym.*, 83(2011), 438-446.

36. J. An, Q. Luo, X. Yuan, D. Wang, X. Li, Preparation and characterization of silver–chitosan nanocomposite particles with antimicrobial activity, *J Appl Polym Sci.*, 120(2011), 3180-3189.

37. S. H. Hsieh, Z. K. Huang, Z. Z. Huang, Z. S. Tseng, Antimicrobial and physical properties of woolen fabrics cured with citric acid and chitosan, *J Appl Polym Sci.*, 94(2004), 1999-2007.

38. A. B. Rezaie, M. Montazer, M. M. Rad, A cleaner route for nanocolouration of wool fabric via green assembling of cupric oxide nanoparticles along with antibacterial and UV protection properties, *J. Clean. Prod.*, 166(2017), 221-231.

39. A. Manhita, V. Ferreira, H. Vargas, I. Ribeiro, A. Candeiasa, D. Teixeiraac, T. Ferreira, C.B. Dias, Enlightening the influence of mordant, dyeing technique and photodegradation on the colour hue of textiles dyed with madder-A chromatographic and spectrometric approach, *Microchem. J.*, 98(2011), 82-90.

40. S. Adeel, F. Rehman, M. Pervaiz, M. Hussaan, N. Amin, A. Majeed, H. Rehman, Microwave Assisted Green Isolation of Laccaic Acid from Lac Insect (Kerria lacca) for Wool Dyeing, *Prog. Colorant Color. Coat*, 14(2021), 293-299.

The Effect of Different Nanoparticles on Dyed Wool Carpet with Walnut Shell Natural Dye

M. Khajeh Mehrizi*[1], F. Malekan[2], M. Veysian[3], Z. Shahi[1]

[1.] Department of Textile Engineering, Yazd University, P.O. Box: 89195-741, Yazd, Iran,

[2.] Iran Carpet Scientific Association, P. O. Box: 141551139, Tehran, Iran.

[3.] Deputy of Research and Training, Iran National Carpet Center, P. O. Box: 1998844641, Tehran, Iran.

ARTICLE INFO

ABSTRACT

N owadays, research on handmade carpet is developing. It is very important to protect dyed fibers by natural dyes in handwoven woolen carpets against harmful environmental bacteria. In this study, the effect of different nanoparticles on dyed woolen carpet has been investigated. Wool yarns were mordanted with alum 10 % and acetic acid 2 % and then dyed with 60 % walnut natural dyes. After dyeing, carpet was woven and finally was treatment in three steps with three types of particles (nano-silver, nano-titanium dioxide and nano-alumina oxide). SEM, FTIR, color value and color strength, self-cleaning, moisture absorption time, the size of the contact angle, anti-odor property and anti-bacterial activities of dyed wool carpet are investigated. The results showed that the hydrophilic properties of samples have been improved. SEM images indicated the presence of nanoparticles on samples. Also, antibacterial properties of samples against E. coli and S. aureus were very good evaluated. Moreover, Long-term static loading was applied on the sample to make the pile up before and after loading. Prog. Color Colorants Coat. 16 (2023), 231-241© Institute for Color Science and Technology.

1. Introduction

J. regia (common walnut) is a deciduous tree of the Junglan-daceae family native to south-eastern Europe. It reaches a height of up to 25−35 m and a diameter of up to 2 m. The water extracted from walnut leaves is reported to exhibit powerful antioxidative and antimicrobial properties owing to the presence of large amounts of phenolic compounds, such as naphtoquinones and flavonoids. From among the naphtoquinones, the juglone is of great importance due to its chemical reactivity [1].

The chief coloring compound present in walnut dye is juglone having molecular formula $C_{10}H_6O_3$. Chemically the molecule of juglone is 5-hydroxy-1, 4-naphthoquinone and is described as natural brown

(juglone, CI 75500), which acts as a substantive dye and imparts brown color to the textile substrates. Juglone is a quinone group aromatic compound has been found in all parts of the walnut tree and it has also been the amounts of juglone were in order of green peel>leaves>bark and it has phytotoxic and allelopathic properties [2-3]. Figure 1 show the main chemical structure of walnut natural dye.
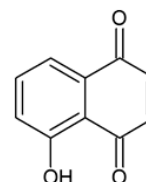

Figure 1: Chemical structure of juglan in a walnut hull [4].

Natural dyes are highly regarded for their chemical composition due to their lack of chemical hazard and toxic effects. Therefore, for many years, the use of renewable and environmentally friendly resources has been considered [5]. In recent years, studies have been conducted on the antifungal activity of phenolic compounds including flavones and related flavonoid glycosides, coumarins and derivatives, and anthraquinones. Presence for a large number of tannins in some of the common plant derived nature dyes and naphthoquinones such as lawsone in henna, juglone in walnut and lapachol in alkannet are reported to exhibit antibacterial and antifungal activity. The antifungal potency of natural dye derived from B. prionitis aerial parts may be due to the presence of phenolic chemical constituents [6].

It is known that naphthoquinones are slightly soluble in water. A small amount of juglone (a quinone form) dissolves in water. When juglone is subjected to aqueous NaOH solution, hydrogen is replaced by metal in the hydroxyl group in the aromatic ring (a phenolate form). A phenolate form of juglone becomes water-soluble [7].

Natural dyes having functional groups such as −OH, −NH$_2$, −COOH, etc. groups and the textile fibers with active sites (–OH, –SO$_3$H, −COOH, −C$_6$H$_5$OH, −NH$_2$) can make a complex with or without mordant. Because of the different interactions of dye and fabric, many functional properties can be achieved. Besides functional group of natural dye such as tannins, flavonoids, anthraquinone, etc., functional groups of respective fabrics are also responsible for functional properties in the fabric [8].

An interest in the use of natural dyes in textile coloration has been rising and this is a result of the rigid environmental standards imposed by many countries in a response to the toxic and allergic reactions associated with synthetic dyes [9]. In this regard, some researchers improved application of natural dyes along with nanoparticles to finding definite properties on wool samples [10].

In this study, we investigated the effect of different nanoparticles on dyed wool with walnut natural dye. Then, morphological properties, color characteristics, self-cleaning, antibacterial activities and some other properties were evaluated.

2. Experimental

2.1. Material and equipment

In this study, merino wool yarn with a score of ten folds, walnut natural dye, nonionic soap (Nikogen SDN), deionized water, mordant alum, acetic acid, hypophosphite and sodium carbonate from Merck (Germany) were used. Also, nano silver with an average particle size of 20 nm, nano dioxide Titanium with a purity of 90 % and a particle size of 20 nm, and nano aluminum oxide with a purity of 99 % and a particle size of 50 nm, were obtained from US Research nanomaterials. X-rite sp62 reflective spectrophotometer, Phenom Prox SEM scanning electron microscope, Spectron 700 transfer spectrophotometer, Camera Video Color- spectrometer series Made in USA Nexus-Spattering, and Colony counter were used for additional analyses.

2.2. Method

Merino wool yarns were first washed in a bath containing 2 g/L nonionic soap at 50 °C for 20 minutes with a L:R=40:1. For mordanting, samples with the alum mordant 10 % and acetic acid 2 % were treated at 100 °C for 45 minutes (Figure 2). Then, the mordanted samples, dyed with the natural dye (60 % o.w.f) at 100 °C for 1 hr (Figure 3).

Finally, after dyeing step, the samples in solution containing 2 g/L nonionic soap at 50 °C for 10 minutes were washed. After washing step, the samples were woven 50 centimeters in 50 centimeters with 50 rings. Woven samples treated at three stages with various nanoparticles.

In the first stage, the woven samples were placed inside a nano silver solution with 0.5 and 2 g/L and acetic acid 10 % (20 % o.w.f) at 80 °C for 15 minutes, then samples was rinsed with deionized water and cured at 100 °C for 10 minutes. In the second step, the samples treated in the solution containing acetic acid 5 % (10 % o.w.f), Sodium hypophosphate 2 % (6 % o.w.f) and nano dioxide titanium as 0.5 and 1.5 g/L at 90 °C for 30 minutes. Treated samples was rinsed with deionized water, and then were cured for 2 minutes at 120 °C.

Finally, Samples were placed in sodium carbonate 3 % (5 % o.w.f) and nano oxide aluminium as 0.5 and 1.5 g/L at 60 °C for 15 minutes and then washed with deionized water and cured in an oven at 100 °C for 10 minutes. Table 1 indicate the condition of treated

samples in the various stages.

Figure 4 indicate the mechanism of interaction between wool, mordant and dye molecule. The oxygen in a polar group of natural dye has a strong affinity for silver ions and silver nanoparticles. The last stage (after coating of dyed samples with all nanoparticles) can involves the formation of coordinative bonding between the oxygen of a hydroxyl group in juglone dye and nanoparticles.
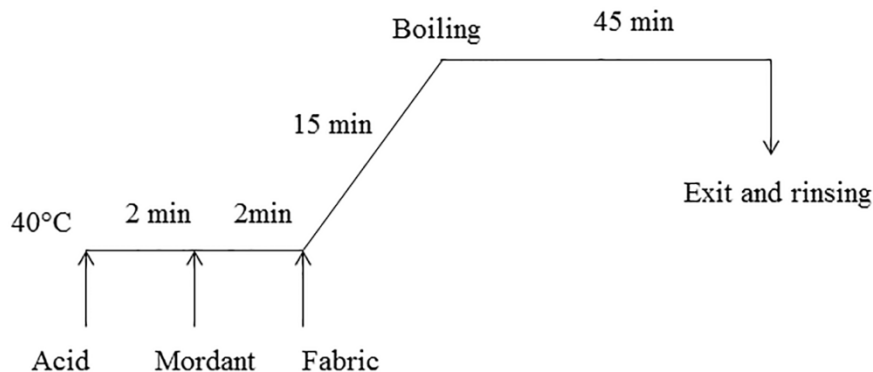
Figure 2: Mordanting diagram.
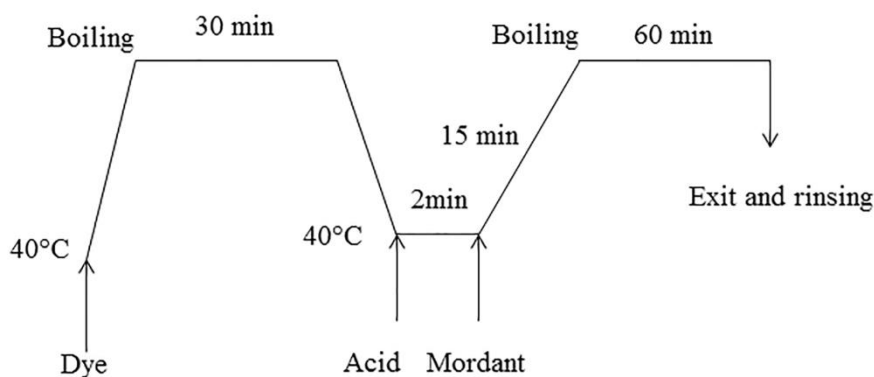
Figure 3: Dyeing diagram.

Table 1: Code of samples and quantities of used materials Walnut shell dye (60 % o.w.f).

Material	G1	G2	G3	G4	G5	G6	G7	G8	G9
Alum mordant %	–	10							
Acetic acid %	–	2							
Nano silver (g/L)	-	2	2	2	2	0.5	0.5	0.5	0.5
Acetic acid 10 %		20 %							
Nano dioxide titanium (g/L)	-	1.5	1.5	0.5	0.5	1.5	1.5	0.5	0.5
Acetic acid 5 %	–	10 %							
Hypophosphite sodium 2 %	–	6 %							
Nano oxide aluminium (g/L)	1.5	0.5	1.5	0.5	1.5	0.5	1.5	0.5	1.5
Carbonate sodium 3 %	–	5 %							
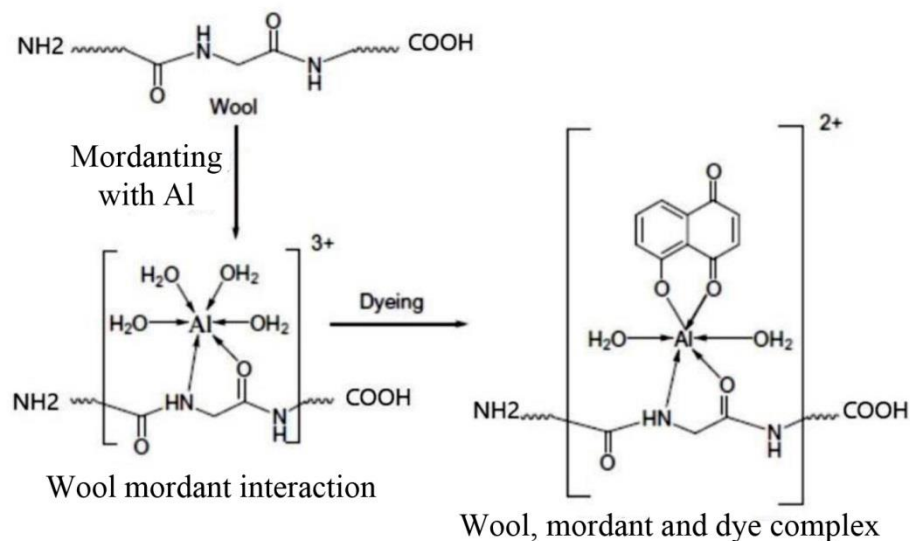
Figure 4: Complex formation between wool, mordant and dye molecule [2].

3. Results and Discussion

3.1. Investigation of color values, self-cleaning properties and color strength

Application of natural dyes on fabric significantly enhances the UPF of the fabric. UPF of fabric is affected by the absorption characteristics of natural dyes. Tannins in plant act as a chemical protector against the UV radiation. Tannin as a phenolic compound absorbs UV radiation due to resonance in structure and hence after the process of attachment on textile surface. These attached molecules absorb the UV radiation and thus protect the skin from absorbing UV rays. The presence of hydroxyl and carbonyl groups in tannins is responsible for forming a large number of hydrogen bonds with fabric and also showed van der Waals forces with fabric, thus improving the color strength of fabric [11]. Tannin-based natural dyes such as R. maritimus, M. philippinensis, K. lacca, A. catechu and A. nilotica have good UV protection properties Ferrous sulphate as a mordant establishes ternary complex with both fiber and the dye, and the remaining coordination sites of Fe metal can absorb UV radiation by converting electronic excitation energy into thermal energy [8].

The color components of the samples were measured with the ASTM D 1925 standard by x-rite sp 62 reflectance spectrophotometer in the range of 400-700 nm with a standard viewing angle of 10 degrees and a D65 light source. All samples were exposed to ultraviolet light for 48 hours after finishing with nanoparticles to evaluate self-cleaning properties. Color strength (K/S) of samples was calculated based on the Kubelka-Munk relation.

Ali Khan et al. [2] confirmed that the walnut dye extract can give satisfactory results in wool dyeing, even without mordanting; also, the use of potassium aluminum sulphate as a mordant in wool dyeing with walnut dye extract resulted in an improvement in the K/S and fastness properties of dyed wool.

Color difference and self-cleaning were investigated using the following equation (CIE L*a*b* 1976) (Eq. 1).

$$\Delta E = \sqrt{\left(\Delta L^*\right)^2 + \left(\Delta a^*\right)^2 + \left(\Delta b^*\right)^2} \qquad (1)$$

In Table 2, the values of the color components and the color strength before and after exposure is stated. In most cases with an increase the amount of silver, titanium dioxide and oxide aluminum nanoparticles increase the brightness of the samples. The amount of redness and yellowness in most samples decrease and, in some specimens, after exposure the ultraviolet light has not changed. Comparing the brightness of the control sample with other samples, the results show that in the G6 sample the maximum brightness is obtained. In other words, rising of L*, indicates an increase in fading due to the self-cleaning property is the result of the presence of nanoparticles.

Table 2: Values of color components, color difference and color strength of treated samples before and after exposure.

code	L*	a*	b*	K/S	R	code	L*	a*	b*	K/S	R
G1	32.22	9.65	16.39	20.33	2.49	UVG1	38.05	10.68	18.38	13.01	3.75
G2	36.3	7.05	11.09	8.12	5.83	UVG2	42.55	7.27	11.17	6.44	7.27
G3	38.2	8.28	13.17	9.91	4.82	UVG3	39.7	8.5	13.18	9.11	8.28
G4	35	7.9	13.03	12.65	3.82	UVG4	38.49	7.64	12.85	10.36	4.69
G5	36.26	8.08	13.07	11.4	4.26	UVG5	38.47	8.35	14.02	8.12	5.88
G6	39.84	8.8	13.62	8.42	5.61	UVG6	41.73	8.77	13.06	7.07	6.64
G7	35.84	7.15	11.72	6.62	4.31	UVG7	38.59	7.32	12.79	8.12	5.81
G8	36.32	7.46	12.11	10.61	4.58	UVG8	40.81	7.56	12.31	7.97	5.93
G9	36.55	9.75	15.18	12.65	3.87	UVG9	36.02	8.82	14.59	10.8	4.45

As can be shown that in Table 2, with increasing the amount of titanium oxide nanoparticles and decreasing the concentration of aluminum oxide nanoparticles, the color difference of the samples and the self-cleaning properties of the carpets have increased. In other words, titanium dioxide nanoparticles have higher self-cleaning properties (more severe oxidizing properties) which is due to the fact that when the nanoparticle optical catalyst coating is irradiated with light, hydroxyl and super-oxidizing radicals produced on the surface are compounded. And cause self-cleaning properties [10].

3.2. Investigation of contact angle and water droplet adsorption time

Surface wettability is one of the most important characteristics of surface quality. The most important characteristic for measuring this feature is the contact angle. Surface roughness is also the most important structural feature of the surface that causes changes in surface wettability. Surface energy is also largely dependent on the surface material. Therefore, changing the surface roughness can be the main goal in achieving surfaces with special hydrophobic and hydrophilic conditions. The hydrophilicity of titanium oxide nanoparticles causes water droplets to always be placed at very low angles on surfaces coated with titanium oxide nanoparticles, tending to spread on the surface. 10 The hydrophilic nature of titanium oxide nanoparticles allows water droplets on surfaces coated with titanium oxide to be always at very low angles and tend to spread on the surface and get wet.

The duration of water droplet adsorption was measured by the standard method AATCC Test Method 79-2000 and to reduce the amount of test error, was performed at four different points of the carpet and the angle of contact of water with the samples was measured with Video Camera Color. Figure 5 shows the contact angle of treated samples. Absorption and desorption of water from wool with the number and type of functional groups in chains protein is associated. On the other hand, the hydrophilicity of nanoparticles depends on their specific surface, the average particle size and how to place the particles in gatherings.

The lowest contact angle and water droplet adsorption time is related to the sample treated with the highest concentration of all nanoparticles (G2 sample). As can be seen from Figure 6, the treated sample with the lowest value of all nanoparticles (G9 sample) attained the highest adsorption time.
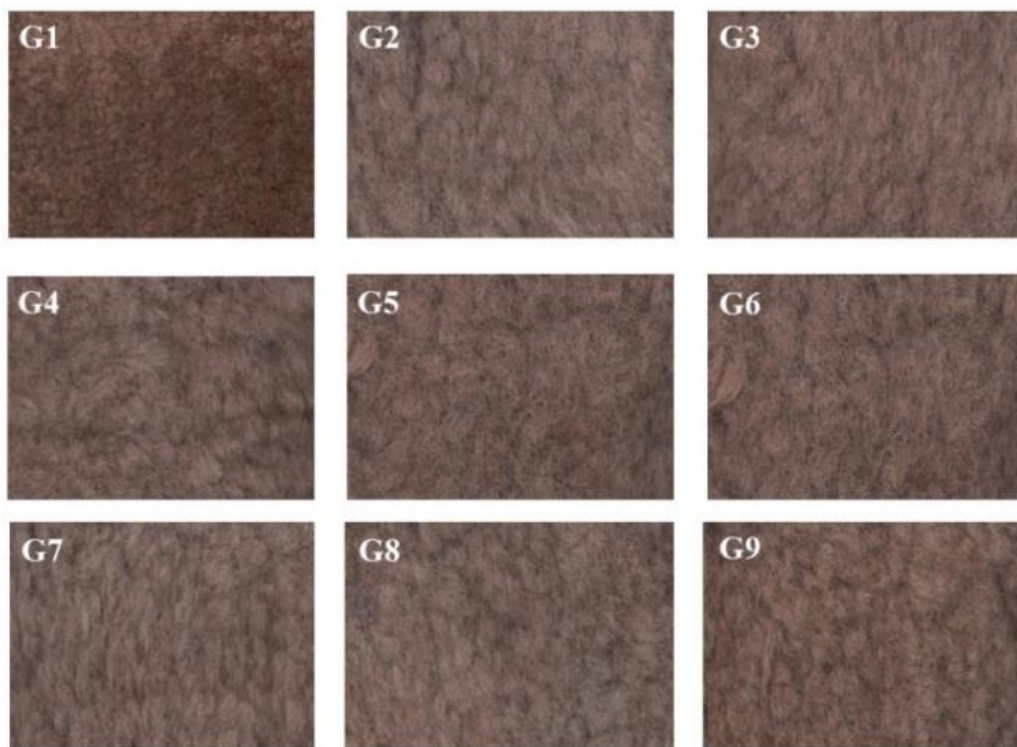
Figure 5: Scanned images of woven carpet.
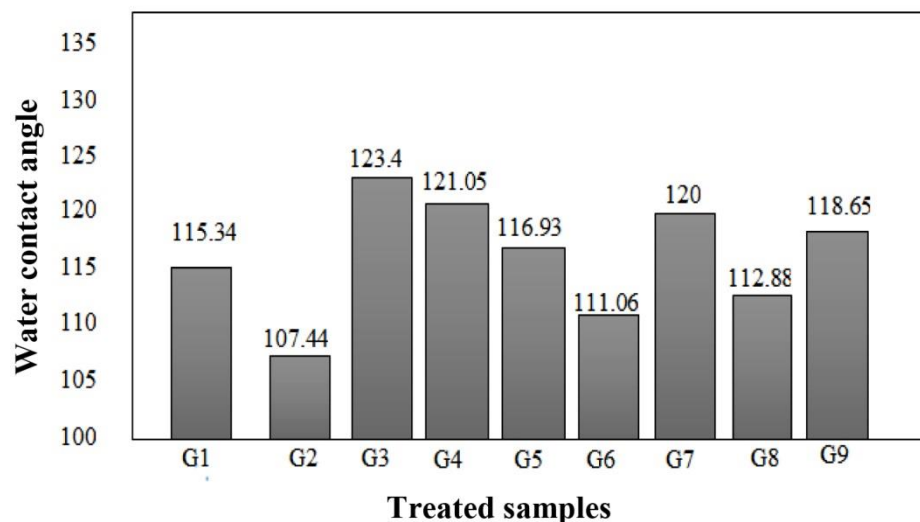
Figure 6: Water absorption time of treated samples.

3.3. Evaluation of detoxification

Natural dyeing of cotton, wool and silk fabric using gallnut also provides a better deodorizing function against ammonia, trimethylamine and acetaldehyde and showed bacterial resistance against Staphylococcus aureus and Klebsiella pneumonia. The main component in the gallnut extract was found to be Gallotannin which is the reason for these functional properties [8]. Human olfactory test was performed according to ISO standard at 22 ± 3 °C and relative humidity R.H= 7%$\pm$38 and processed samples with 200 grams of chopped onions are kept in a sealed container for 24 hours [12]. After 24 hours, the samples were removed from the container and each one was placed inside the

human with a lid. In this case, the samples were then given 1 hour to balance their upper space for human olfactory testing [13].

The samples were evaluated by 9 people and the obtained numbers are the average of this evaluation. These numbers show that due to the use of aluminum nanoxide in the final stage of completion, the samples have been significantly deodorized. (G5, G6 and G7 samples indicate the highest odor intensity and also G1 and G2 samples indicates the lowest odor intensity based on human sense of smell (Figure 7).

3.4. Investigation of surface morphology of samples using scanning electron microscopy

SEM were performed on four samples (raw wool, walnut dyed sample (G1), walnut dyed sample and supplemented with the highest (G2) and lowest (G9) nanoparticles (Figure 8).

Figure 9 displays that raw wool (untreated wool) and G1 sample have perfectly defined scales with clear edge. Moreover, existence of nanoparticles and their submicron aggregates in surfaces of finished samples (G2 and G9) with uniform distribution and small particle size about 66 nm can be seen.
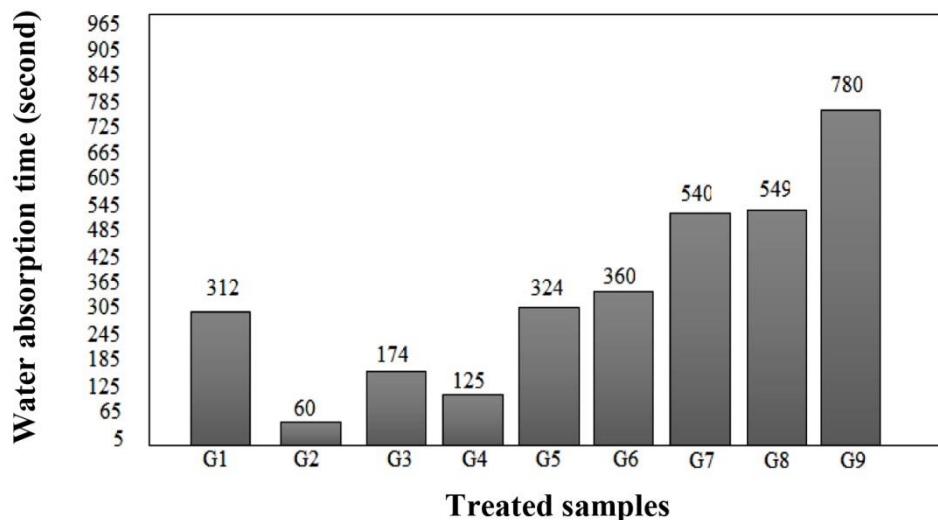

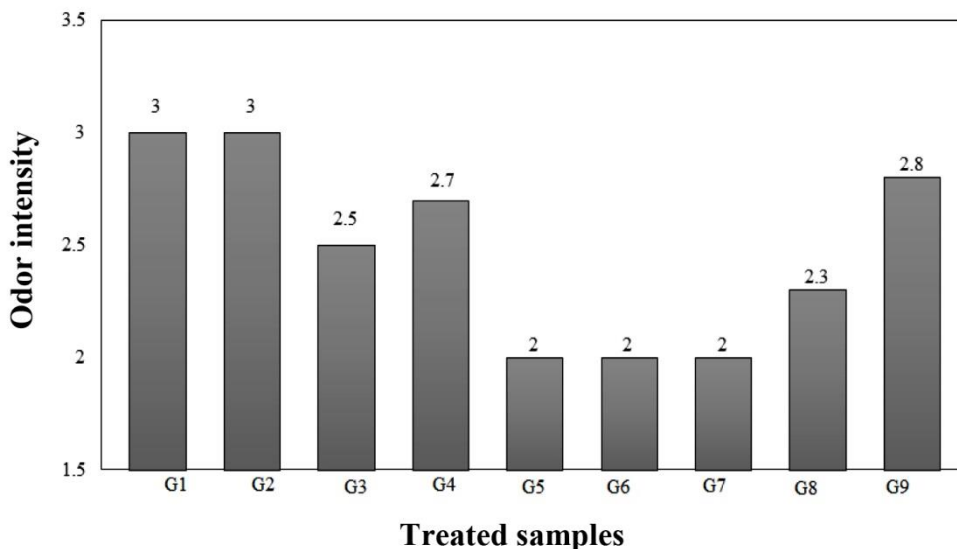**Figure 7:** Water absorption time of treated samples.

Figure 8: The odor intensity treated samples.

3.5. Static loading

Carpets are usually exposed to two types of loads during use: static (such as table and chair bases) and dynamic (such as walking on the carpet, moving furniture on the carpet). Carpet yarns are compacted in this constant or fast compressive load, their deformation is complex, and each villus are individually subjected to different deformation modes due to axial pressure, bending, flattening, stretching and shearing. Compressive behavior of carpet lint during loading and reaction. Their dynamics after load removal have an important role in their mechanical performance. Static loading machine with force arm has been used on the same basis from 1966 until today. Often in this machine, a horizontal arm with an end weight is designed to apply a load with a length ratio of 1: 5 to the arm in contact with the product. five times the amount of weight added to the end of the horizontal arm will apply a constant compressive load to the sample.

Standing and walking are different forces and deformations that applied to carpet piles during such human daily activities. Axial compression, bending, flattening, and extension and also static and dynamic pressure are some examples of these deformations. Furthermore, the compression behavior and mechanical reaction influence on the piles thickness loss in the carpet. The recovery behavior of the pile carpet after static loading is important for the quality, performance and lifetime of the piled carpet after static loading [10].

Carpet is predominantly used in home floor covering as an indispensable decorative product and also preferred by its heat and sound insulation feature. Compression performance in general terms of mechanical properties influences carpet performance under dynamic or static loads. Carpet thickness will be deformed when it is exposed to dynamic and static loads which are created by walking and furniture, respectively. During daily usage of the carpet, thickness loss is directly affected by raw material, pile height, carpet construction, pile density etc. There are a lot of studies focused on effects of these parameters on carpet performance based on static loading, dynamic loading and compressibility [14].

This experiment was performed by long-term loading method with a compressive load period of 24 hours. This test is in accordance with BS ISO 10834 standard. The sample (G2) was subjected to a compressive load of 700 kPa for 24 hours by a static loading device. After loading, the villi height of the sample was measured and recorded. Result in Table 3 indicate that after unloading, the villi height of the sample decrease.

3.6. Investigation of antibacterial properties

The surrounding of human includes a variety of microorganisms like bacteria and other microbes, which are invisible for the naked eyes. Bacterium is a unicellular organism. It is divided in Gram-positive like Staphylococcus aureus (S. aureus) and Gram-negative like Escherichia coli (E. coli) on the basis of chemical and physical properties of their cell walls. It is reported that antibacterial and antifungal properties of natural dye are due to its phenolic content. Phenolic compounds attach on the surface of textiles by forming a complex. When the fabric comes in contact with microbes, these attached phenolic compounds hamper the enzyme production in microbes; thus, further cell reaction would not take place and at the end cell dies.

Rumex maritimus (golden dock) and Quercus infectoria (indigo) dyes are found to be the most effective against common microbes like E. coli, Bacillus subtilis, Klebsiella pneumoniae, Proteus vulgaris and Pseudomonas aeruginosa. Berberine compound as a cationic dye having quaternary ammonium structure can act as an antibacterial agent. The dyed wool represented a high level of antibacterial activity. Application of natural dyes like pomegranate, clove, coptis chinensis (Chinese goldthread) and gallnut extracts on cotton, silk and wool fabric provides excellent antibacterial activity against S. aureus.

Table 3: Height of carpet sample lint.

The height of the villi, 1 minute after unloading (cm)	Initial height of the villi (cm)	Sample code
0.35	0.47	G1

Generally, water soluble nanoparticles might be able to be absorbed internally by wool [15]. The antibacterial properties of AgNPs mostly depends upon the size, pH and ionic strength of the medium [16]. The silver ions bind disulphide (S- S) and sulfhydryl (-SH) groups of wool fiber in the microbial cell wall's protein resulting in the disruption of metabolic processes, and ultimately cell death happen [17]. When silver molecules apply with binder or any cross-linking agent, an increased durability to clean wash was obtained in antimicrobial performance. Dyes obtained from plants have antimicrobial properties. Like beet root, pomegranate seeds, curcumin etc. due to the presence of tannins quantity. Other sources like naphthoquinones such as lawsone from henna, juglone from walnut and lapachol from alkanet exhibit antimicrobial activity [18].

In this study, the quantitative AATCC Test Method 1993-100 was used to evaluate the antibacterial activity against S. aureus and E. coli. The test method is described in our previous study [19].

Antibacterial test results in dyed sample and treated with 2 g/L nano silver and 0.5 g/L aluminum nano oxide and titanium nano dioxide (G2) and also, dyed sample and treated with 0.5 g/L Nano-silver, nano-aluminum oxide and nano-titanium dioxide (G9) were evaluated (Table 4).

In general, S. aureus is more resistant than E. coli because the cell wall membrane of S. aureus is thicker than E. coli. Result of sample in Table 4 shows that the small value of nanoparticles can be granted great antibacterial properties to samples especially against to gram-negative microbes. The antibacterial efficacy toward E. coli were higher than S. aureus at the low silver concentration, indicating that gram-negative bacteria are generally more sensitive to Ag NPs than gram-positive bacteria [20].

3.7. FTIR spectra analysis of samples

The FTIR spectra of raw wool, G1 and G2 samples are presented in Figure 9. The strong peaks at 2949 and 2867 cm^{-1} are attributed to CH_3 asymmetric/symmetric stretching vibrations, and those at 2916 and 2837 cm^{-1} are assigned to CH_2 asymmetric/symmetric stretching vibrations. The peaks around 842 and 810 cm^{-1} are due to CH_2 rocking vibrations in the crystalline regions [21].

Table 4: Investigation of antibacterial properties of treated samples.

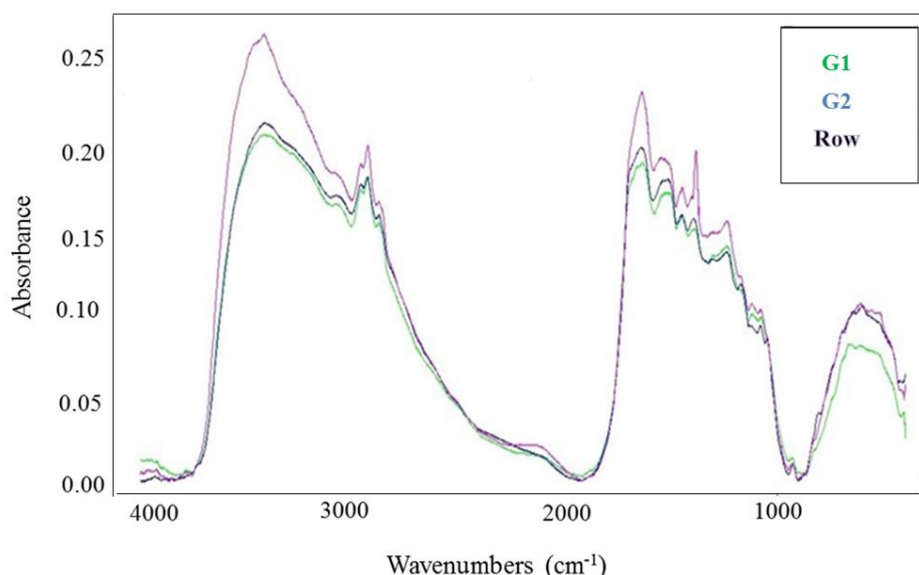| Percentage reduction of S. aureus bacteria	Percentage reduction of E. coli bacteria	Number of S. aureus colonies	Number of E. coli colonies	Sample code
0	0	>1000	>1000	G2
30	100	700	0	G9

Figure 9: FTIR spectra of raw wool, G1 and G2 samples.

The main characteristic peaks of raw wool fibers due to protein macromolecule evidenced at 1639, 1546, and 1238 cm^{-1} correlated to amide I (C=O stretching), amide II (N–H stretching), and amide III (N–H in-plane bending and C–N stretching), respectively. Moreover, a broad band is considered at 3432 cm^{-1} due to the N-H stretching vibrations of terminal amino group. As can be seen, compared with raw wool sample, these bands' position and intensity undergo red-shift to lower frequencies and intensity in the dyed and treated wool fibers (G1 and G2), which is due to interaction of Ag nanoparticles with the amide groups [22].

4. Conclusions

In this study, firstly, woolen yarns were mordanted with alum, and then dyed with Walmut natural dye. After dyeing, carpet was woven and it was treated in three stages with three types of Nano-silver, Nano-titanium dioxide and Nano-alumina oxide. Using nano particles, the color strength of the samples has been reduced after receiving UV light, and self-cleaning properties of samples have been improved. The results showed that the hydrophilic properties and brightness values of samples is improved. SEM images indicated the effect of nano particles on treated carpets. The rate of water drop absorption of the treated samples has increased and their contact angle has decreased. In long-term static loading, the height is reduced by measuring the length of the villi. In the antibacterial test, the percentage of reduction against E. coli was higher than S. aureus bacteria. In the view of anti-odor test, an average of odor reduction was attained in the most samples. FTIR spectra of samples indicated the interaction of nanoparticles with amide groups. Present study displayed using of mentioned nanoparticles can reach multifunctional handmade carpet.

5. References

1. A. Ojstršek, D. Fakin, Natural dyeing of wool using Junglans regia (Common Walnut) leaf extract, *Tekstilec.*, 62(2019), 288-298.
2. M. Ali Khan, S. Ul-Islam, F. Mohammad, Extraction of natural dye from Walnut bark and its dyeing properties on wool yarn, *J. Natural Fibers.*, 13(2016), 458-469.
3. İ. Kocaçalışkan, E. Turan, Ü. Ertürk, Y. Demir, İ. Terzi, Varietal and time dependent differences in juglone and total phenolic contents of the walnut (Juglans regia L.) leaves, *Prog. Nutrition.*, 22(2020), 193-198.
4. F. Mirshahi, A.r. Khosravi, K. Gharanjig, J. Fakhari, Antimicrobial properties of treated cotton fabrics with non-toxic biopolymers and their dyeing with safflower and walnut hulls, *Iran Polym. J.*, 22, (2013), 843-851.
5. M R. Shahparvari, M. Safi, S. Safapour, K. Gharanjig, Compatibility of natural dyes on aluminum pre-mordanted woolen yarns by determination of diffusion coefficient, *Fibers Polym.*, 19 (2018), 1663-1669.
6. P. Anita, K. Rakesh, U. Lokesh, Y.C. Tripathi, Antifungal Activity of Natural Dye from Aerial Biomass of Barleria prionitis L. and Dyed Fabrics, Iran. *J. Chem. Chem. Eng.*, 37(2018), 213-221.
7. E. V. Emelyanova, I. P. Solyanikova, Understanding the mechanism of formation of a response to Juglone for Intact and immobilized bacterial cells as recognition elements of microbial sensors: processes causing the biosensor response, *Biosensors.*, 11(2021), 77-83.
8. D. Pargai, S. Jahan, M. Gahlot, Functional Properties of natural dyed textiles. [Online], Book technology of natural and synthetic dyes and pigments, chapter 9, London, United Kingdom, 2020, 6. Available from: https://www.intechopen.com.
DOI: 10.5772/ intechopen.88933.
9. N. Ashrafi, K. Gharanjig, M. Hosseinnezhad, M. Khajeh Mehrizi, H. Imani, N. Razani, Dyeing properties and color fabrics using natural dye and mordant, *Prog. Color Colorants Coat.*, 11(2018), 79-83.
10. F. Malekan, M. Khajeh Mehrizi. S. M. Veysian, The Effect of Nanomaterials on Dyed Handmade Carpet with Weld Natural Dye, *J. Color. Sci. Tech.*, 14(2020) 203-214.
11. F. Nazir, A. Siddique, A. Nazir, S. Javed, T. Hussain, S. Abid, Eco-friendly dyeing of cotton using waste-derived natural dyes and mordants, *Color. Technol.*, 138(2022), 684-692.
12. I. Ebrahimia, M. Parvinzadeh Gashti, Extraction of juglone from Pterocarya fraxinifolia leaves for dyeing, anti-fungal finishing, and solar UV protection of wool, *Color. Technol.*, 131(2015), 451-457.
13. A. Nazari. Introduction to Textile Machinery, Islamic Azad University, Yazd Branch, First Edition, 2014.
14. D. Vuruşkan, E. Sarıoğlu, H.İ. Çelik, H.K. Kaynak. Compression properties of woven carpet performance under dynamic loading, *Periodicals Eng. Natural Sci.*, 5 (2017), 181-186.

15. D. G. King, A. P. Pierlot, Absorption of nanoparticles by wool, *Color Technol.*, 125(2009), 111-116.

16. S. A. Ahmad, S. S. Das, A. Khatoon, M. Tahir Ansari, M. Afzal, Bactericidal activity of silver nanoparticles: A mechanistic review, *Mater. Sci Energy Technol.,* 3(2020), 756-769.

17. R. Kaur, Dr. A. Tomar, A review of wool from microbe's growth, *Inter. J. Sci. Res. Develop.*, 5(2017), 744-745.

18. R. Assefi Pour, R. Bagheri, T. Naveed, N. Ali, F. Rehman, J. He, Surface functionalization of wool via microbial-transglutaminase and bentonite as bio-nano-mordant to achieve multi objective wool and improve dyeability with madder, *Heliyon*. 6(2020), e04911, 2020.

19. M. Khajeh Mehrizi, S. M. Mortazavi, D. Abedi, The antimicrobial characteristic study of acrylic fiber treated with metal salts and direct dyes, *Fiber Polym.,* 10(2009), 601-605.

20. S. Mowafi, H. Kafafy, A. Arafa, K. Haggag, M. Rehan, Facile and environmental benign in situ synthesis of silver nanoparticles for multifunctionalization of wool fibers, *Environ. Sci. Poll. Res.,* 25(2018), 29054-29069, 2018.

21. M. Glogar, J. Tancik, I. Brlek, A. Sutlovic, Tkalec M. Optimisation of process parameters of Alpaca wool printing with Juglans regia natural dye, *Color. Technol.*, 136(2020), 188-201.

22. H. Barani, M. Nasiri Boroumand, S. Rafiei, Application of Silver nanoparticles as an antibacterial mordant in wool natural dyeing: synthesis, antibacterial activity, and color characteristics, *Fiber Polym.*, 18(2017), 658-665.

Fluorescence Quenching Study of Nano Graphene Oxide Interaction with Naphthalimide Dye: Thermodynamic and Binding Characteristics

M. Mahdiani[1], Sh. Rouhani[*2,3], P. Zahedi[1, 4]**

[1.] Department of Polymer Engineering, Kish International Campus, University of Tehran, P.O. Box: 141763-3644, Kish Island, Iran

[2.] Department of Organic Colorant, Institute for Color Science and Technology, P.O. Box: 16765-654, Tehran, Iran

[3.] Center of Excellence for Color Science and Technology, Institute for Color Science and Technology, P.O. Box: 16765-654, Tehran, Iran

[4.] School of Chemical Engineering, College of Engineering, University of Tehran, P.O. Box: 11155-4563, Tehran. Iran

ABSTRACT

A quenching study was reported for interacting a fluorescence naphthalimide derivative with graphene oxide (GO) as a quencher. 1,8-naphthalimide fluorophore with two amine functional side arms (NN2) was synthesized and characterized. Many different 1,8-naphthalimide fluorescence dye derivatives have been designed for fluorescence probe application. Fluorescence quenching-based platforms in nanoscale have extensively been used in sensing systems. Raman, FTIR, UV-Vis, and fluorescence spectroscopic techniques were used to study GO and NN2 characteristics and their photophysical and quenching mechanisms at different temperatures. The results indicated that graphene plays an effective quencher against the naphthalimide molecule, with quenching efficiently at 91 %. The Stern-Volmer analysis results show a mix of static and dynamic quenching mechanisms. The binding constant of the quencher and fluorophore and the number of binding sites have been reported. Thermodynamic parameters of their interaction were evaluated. The negative values of the ΔG confirm that the complexation process is spontaneous. Meanwhile, the positive entropy value confirms the favourable pathway process. Prog. Color Colorants Coat. 16 (2023), 243-253© Institute for Color Science and Technology.

1. Introduction

Nano graphene oxide with unique optical and physicochemical properties attracted much attention for sensor application. Its excellent electrical conductivity, fast electron mobility, tunable optical properties, high mechanical strength, and functionalization capability make it an efficient platform for developing sensor applications [1-8]. One of the most sensitive optical sensors is based on the quenching process between a fluorophore and a quencher. Reported quenching mechanisms of graphene oxide (GO) as a quencher are

based on one of these models, the photoinduced electron transfer (PET) process or Förster resonance energy transfer (FRET). The fluorophore directly affected by the graphene quencher makes it suitable for optical sensing platforms [9-14]. When GO and the fluorophore are close, the energy or excited electron is transferred from the fluorophore to GO. In this case, the fluorescence signal decreases.

Among fluorescence dyes, 1,8-naphthalimide has been applied in different areas. They are used in the paint and textile industry, sensors, laser diodes, and

biological probes [15, 16]. Their excellent stabilities, such as photo, thermal, and chemical stability, attracted much attention. Their derivatives showed high fluorescence efficiency [17, 18]. These properties make it to be a good candidate for sensitive fluorescent sensors. Easy modification of the fluorescence core achieved through imide or core position resulted in a desirable design for specific interaction and an efficient fluorescent probe [18]. The design and development of novel platforms based on graphene as the energy acceptor have been a remarkable success in recent years. Our team is developing the design and application of fluorochrome dyes for probe applications. Gharagozlou et al. reported a new reusable mercury-sensitive turn-on nano-chemosensor based on CoFe$_2$O$_4$@SiO$_2$ magnetic nanocomposite. It was functionalized by napthalimide-rhodamine sites [19]. Seraj et al. investigated the fluorescence quenching mechanism of a naphthalimide dye derivative by graphene oxide [20]. Seraj et al. in 2019, developed a naphthalimide-based optical turn-on sensor for monosaccharide recognition using a boronic acid receptor [21]. Also, Seraj et al. in 2021 reported the synthesis and fluorescence quenching mechanism of a novel naphthalimide derivative by nanographene oxide [22].

Recently we worked on the effect of graphene oxide as a quencher on the different naphthalimide derivatives. Studies on the quenching mechanism between graphene oxide and a symmetric di-amino functionalized 1,8-naphthalimide dyes have yet to be reported. This work investigated the synthesis of a water-soluble 1,8-naphthalimide dye. The mechanism of quenching was studied by UV-Vis and fluorescence spectroscopic techniques. Also, the thermodynamic pathway of interactions was investigated. The quenching parameters were obtained, and involved mechanisms were reported.

2. Experimental

2.1. Materials

4-Bromo-1,8-naphtalic anhydride and ethylenediamine were purchased from Merck Chemical Co. and used as received. All solvents were of analytical grade. The used graphene oxide was purchased from Nano SANY Co. (product number; US 7906, CAS 7732-18-5). A stock solution of dye (10^{-3} M) was used for spectroscopic investigations.
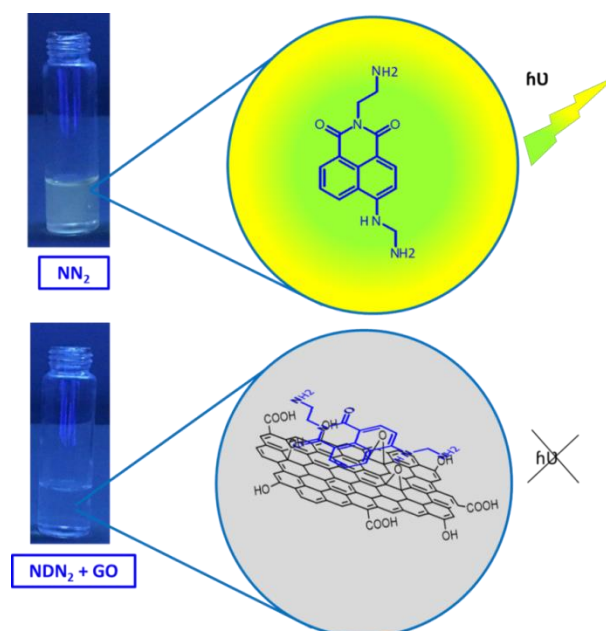
Scheme 1: Schematic of NDN2 quenching by graphene oxide.

2.2. Synthesis of fluorescence dye (NN2)

NN2 was synthesized from 4-bromo-1,8-naphtalic anhydride, according to our previous work [21, 22]. 0.3 g 4-Bromo-1,8-Naphtalic anhydride was dissolved in 12 mL Ethanol. 40 mL ethylenediamine was added in 2 steps intervals. The resulting solution was heated under reflux for 24 h. After cooling, the ethylenediamine was distilled under a vacuum to afford a crude product. After recrystallization from ethanol, yellow needles were obtained (90 %). m.p. 235 °C, FTIR (KBR) cm^{-1}: 3439, 3080, 2934, and 1729 cm^{-1}. ^{1}H NMR (400 MHz, DMSO-d6): d (ppm) = 8.55 (d, 1H, Ar-H), 8.32 (d, 1H, Ar-H), 8. (d, 1H, Ar-H), 7.62 (t, 1H, Ar-), 6.73 (d, 1H, Ar-), 4.83 (s, 4H, –NH$_2$), 4.41 (s, 1H, –NH–), 4.04 (t, 2H, –CH$_2$–), 3.92 (t, 2H, –CH$_2$–), 3.22 (t, 2H, –CH$_2$–) ,3.00 (t, 2H, –CH$_2$–). Anal. Calcd. for C$_{16}$H$_{18}$N$_4$O$_2$ (%): C, 64.41; H, 6.08; N, 18.78. Found: C, 64.51; H, 6.01; N, 18.68.

2.3. Apparatus

^{1}HNMR spectra were recorded with Brucker spectrophotometer at 500 MHz (solvent: DMSO). FTIR spectra were recorded on a SPECTRUM ONE spectrometer. A Perkin-Elmer LS55 fluorescence spectrophotometer was used for all fluorescence measurements. UV-VIS absorption spectra were measured on a CECIL-CE9200 spectrophotometer.

2.4. Preparation of NN2/GO

A stock dispersed GO solution was prepared by 20 min sonication of appropriate GO powder in distilled water. To a 0.1 mL of the stock solution of NN2 (10^{-3} M), an appropriate amount (0, 8, 10, 15, 20, 25, 30, 35, 40, 45, 50, 55 μg/mL) of 30 μg/mL GO was added, sonicated for 10 min, and, diluted to 5 mL was transferred into a 5 mL tube.

3. Results and Discussion

### 3.1. Synthesis of fluorescence dye (NN2)

The synthetic route for the preparation of NN2 is shown in Scheme 2. A simultaneous nucleophilic substitution on two positions of naphthalic anhydride molecule by ethylenediamine has been performed. Position, 4 of naphthalic anhydride ring is prone to nucleophilic attack. Also, the anhydride ring and the carbonyl groups have a suitable position for the nucleophilic attack, subsequently forming a stable amide ring. NN2 was obtained with a good yield of 90 %. Results of FTIR and HNMR, and CHN analysis firmly identified the structure of compound NN2.

3.2. Photophysical properties

NN2 is related to the 1,8- naphthalimide category of dyes, which have photophysical properties, and strongly depend on the dicarboximide and amino-substituted groups. The amino-substituted groups with the ethylene space show a photoinduced charge transfer process (PET) to carbonyl groups. The electron charge transfer between the donor-acceptor (the imide moiety or C-4 position of the chromophoric core and the carbonyl groups) and resulting polarization is responsible for the spectral characteristics of these derivatives [15, 16].

The absorption and emission spectra of dispersed NN2 in H_2O are shown in Figure 1. The dye shows a yellow-green color (λ_{abs}= 420 nm). The wavelength band around 420 nm (ε= 13900 L mol^{-1}.cm^{-1}) confirms a charge transfer (CT) band due to ($\pi \rightarrow \pi^*$) transition of the S0$\rightarrow$S1 transition [23]. There is a band in ABS spectra at about 550 nm attributed to intermolecular charge transfer (ICT) [24]. The dye emission was shifted to the visible region with a maximum (λ_{em}= 540 nm) with an intense yellow-green emission and a significant 120 nm stock shift.
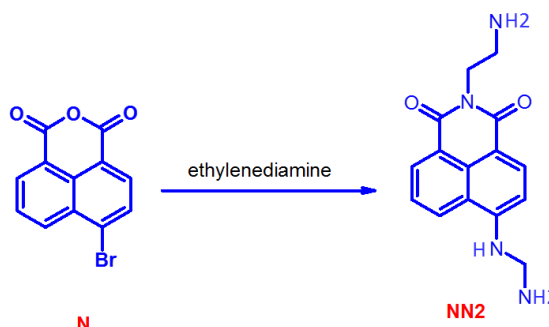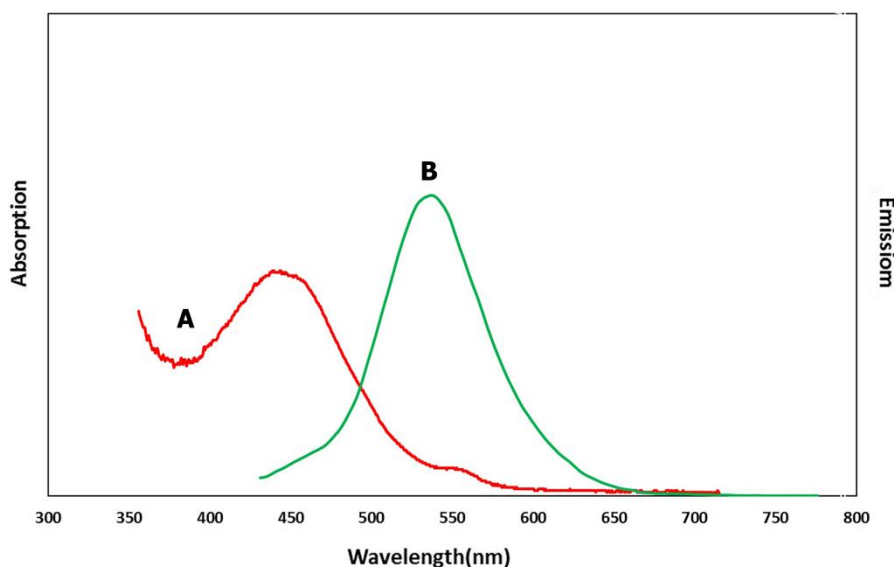

Scheme 2: Synthesis of NN2.

Figure 1: A) Absorption and B) emission spectra of NN2 (10^{-5} M) in H_2O.

3.3. Characterization of GO

SEM and UV-Vis techniques were applied to characterize the commercial GO used, as shown in Figure 2a and b. SEM image shows the planar morphology of GO. These results showed that the used GO was indeed a single-layer sheet. As shown in Figure 2b, maximum absorption at 229 nm confirms the π-π* transition of aromatic C=C bonds. Also, a shoulder around 300 nm is related to the n-π* transition of C=O bonds [25].

Raman analysis was also conducted for the absorption of NN2 and GO, shown in Figure 3. The Raman spectra of GO show GO's characterized D and G bands at (1348 cm^{-1}) and (1599 cm^{-1}), respectively, approving the presence of GO. The GO spectrum, after interaction with NN2 remarkable intensity reduction at the D and G bands without any significant shift. These results can be further evidence of the interaction between GO and NN2.
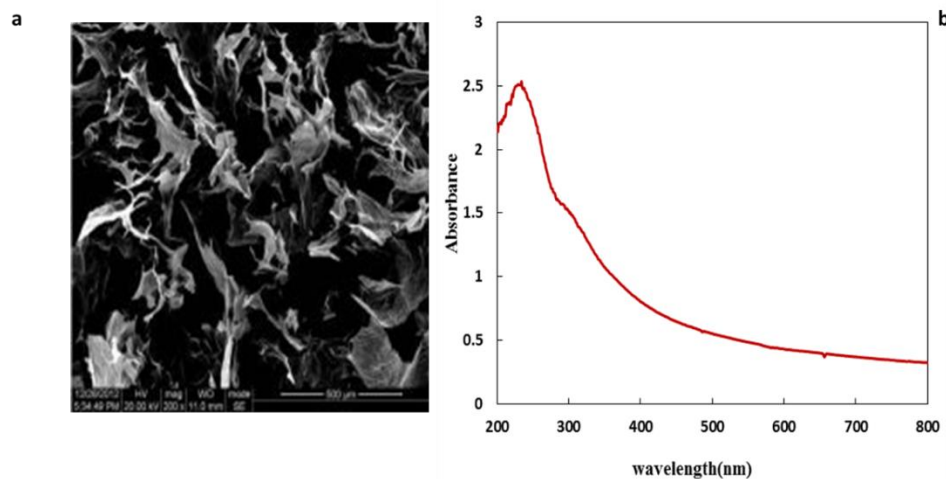

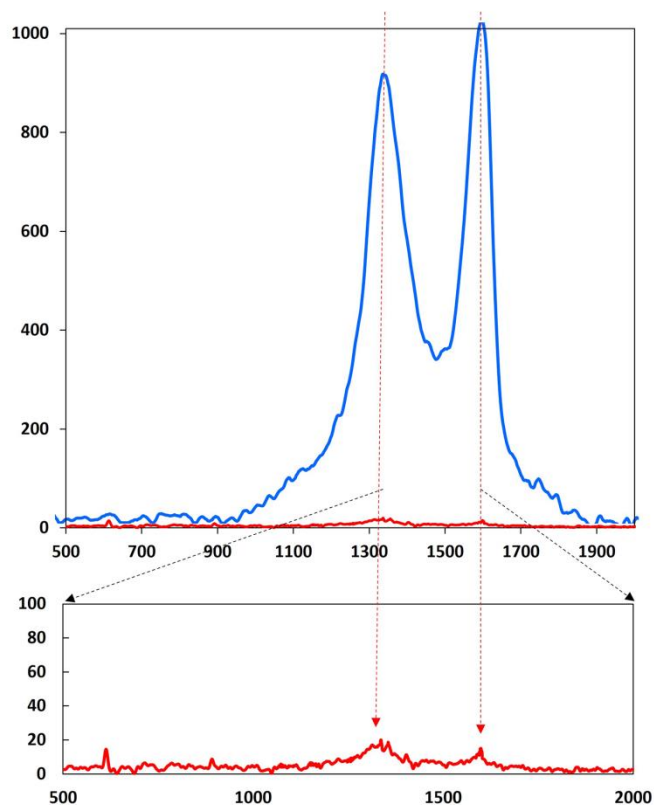**Figure 2**: a) SEM, b) UV-Vis spectra of used GO.

Figure 3: Raman spectra of GO before (blue) and after adsorption of NN2 (red).

Figure 4 shows FTIR spectra of individual GO, NN2, and a mixture of GO+NN2. As obvious in the figures, characteristic peaks of C=O vibration for GO are at 1723, 1572, and 3000-3200 cm^{-1}. Also NN2 shows C=O vibration at 1732, N-C stretching at 1600, 1532, and NH$_2$ vibration at 3331 cm^{-1}. Remarkable changes occur on these characteristic peaks for the mixture of GO and NN2. The peak at 3445 is going to be wider, with different shapes for GO in this region. The C=O vibration peak is shifted to the lower vibration energy at 1627 cm^{-1}, respecting the individual GO and NN2 C=O peaks. Our previous work obtained the same results [21, 22].

3.4. Quenching mechanism

A wide variety of processes can decrease the intensity of fluorescence. Such decreases in intensity are called quenching. Quenching can occur via different pathways. Energy transition takes place by non-radiative process, where two species come close together to transfer the energy. Collisional quenching occurs when the excited-state fluorophore is deactivated upon contact with some other molecule in the solution, which is called the quencher. Then the fluorophore is returned to the ground state. A wide variety of molecules can act as collisional quenchers. Examples include oxygen, halogens, amines, and electron-deficient molecules [26].

The fluorescence emission spectra of NN2 are illustrated in Figure 5. It shows a maximum intensity at 540 nm, gradually decreasing with increasing GO concentration. Changes indicate that GO is a quencher of the naphthalimide fluorophore (NN2). Also, GO has no fluorescence at the NN2 excitation wavelength. The quenching was due to the interaction between NN2 and GO, not an inner filter effect or reabsorption. As previously reported in the literature, GO was the oxidized form of graphene with the carboxylic acid, hydroxyl, and epoxy groups [27-29]. Therefore, GO could have π-π stacking interaction with aromatic rings of aromatic molecules, herein, NN2 dye. The quenching efficiency is defined as $\eta = (F0-F)/F0 \times 100$, for which a high value of (91.33 %) was obtained for the NN2.
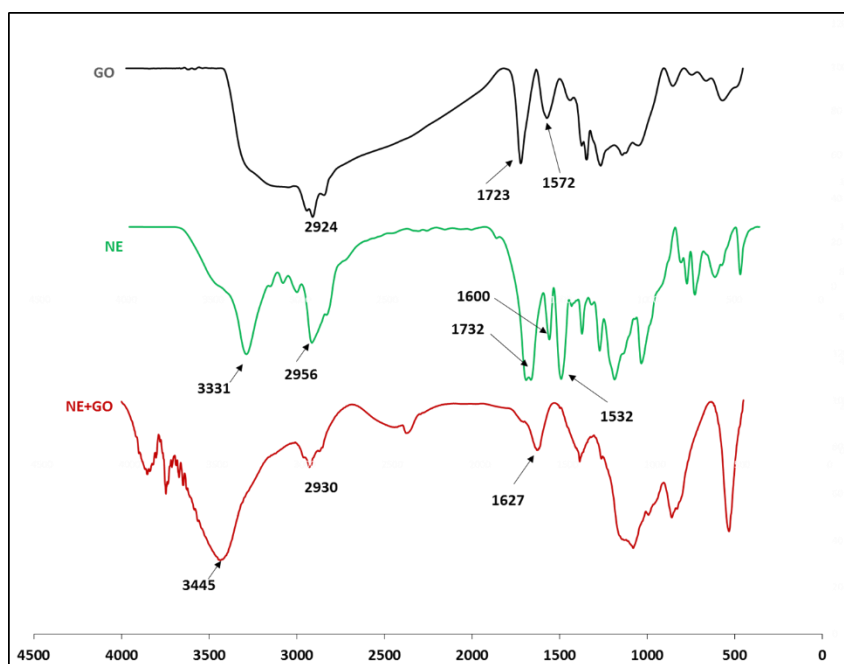

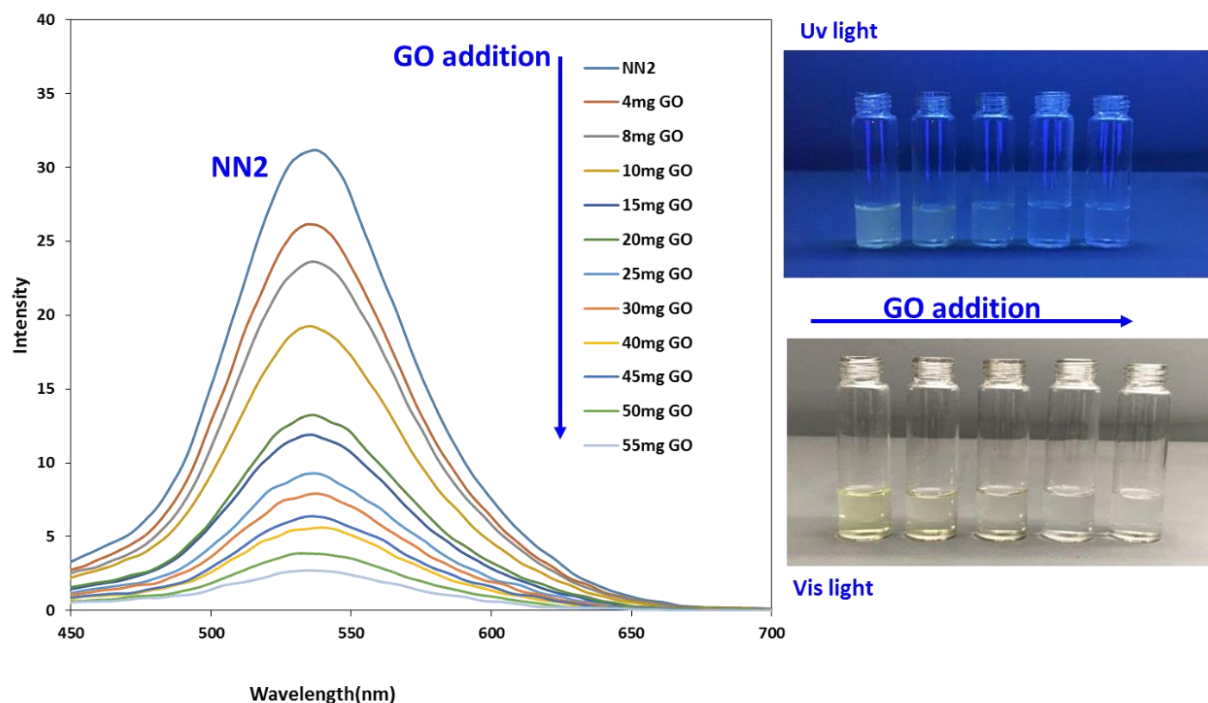**Figure 4:** FTIR spectra of GO, NN2, and GO+NN2.

Figure 5: left) Fluorescence spectra of (10^{-5} M) NN2 in the presence of various concentrations of GO, right) Photographs of NN2 during GO addition under UV light(up) and Vis light (down).

It was found that quenching goes through either static or dynamic interaction mechanisms [30, 31]. When a complex formation between an emissive molecule and a quencher occurs, it is called static quenching. The resulting complex has no emission. Therefore, its intensity gradually decreases by adding a quencher. Dynamic quenching is called collisional quenching because a collision with a quencher causes a loss of emission. Herein there is not any complex formation [32]. The Stern-Volmer equation (Eq. 1) was used to study the dynamic quenching mechanism [26].

$$F_0/F = 1 + K_{sv}[Q] \tag{1}$$

F_0 and F are the molecule's fluorescence intensity in the quencher's absence and presence, respectively. K_{sv} is the binding constant of the quencher-fluorophore, and [Q] is the concentration of the quencher. Temperature directly affects dynamic quenching because this process goes through a diffusion-controlled pathway. The diffusion of the quencher to the fluorophore during the lifetime of the excited state is essential. Increasing the temperature resulted in a faster diffusion rate, and the bimolecular quenching constants are expected to increase. In static quenching, a non-fluorescent complex forms at the ground state; therefore, K_{sv} decreases with increasing temperature. In

some processes, there is not involved only one quenching mechanism.

Generally, dynamic quenching involves the collision followed by the formation of a transient complex between an excited-state fluorophore and quencher. Recording the effect of temperature on the quenching efficiency helps identify which mechanisms are involved. It is found that the higher temperature increases the possibility of collision. It resulted in a higher quenching efficiency, known as dynamic quenching. At the same time, less quenching was observed at a lower temperature [29, 33]. The fluorescence emission results of NN2 in the presence of GO were obtained at different temperatures (288, 298, and 308 °k). Figure 6 illustrates the Stern-Volmer plot, in which a higher quenching efficiency was observed at lower temperatures. Results showed that dynamic quenching was not the primary quenching mechanism of NN2. As can be seen, the dependence of F_0/F on [Q] strayed from linearity.

The expansion is due to the strong and π-π stacking between NN2 and graphene oxide. These results showed that the responsible quenching mechanism for NN2/GO follows both dynamic and static quenching.
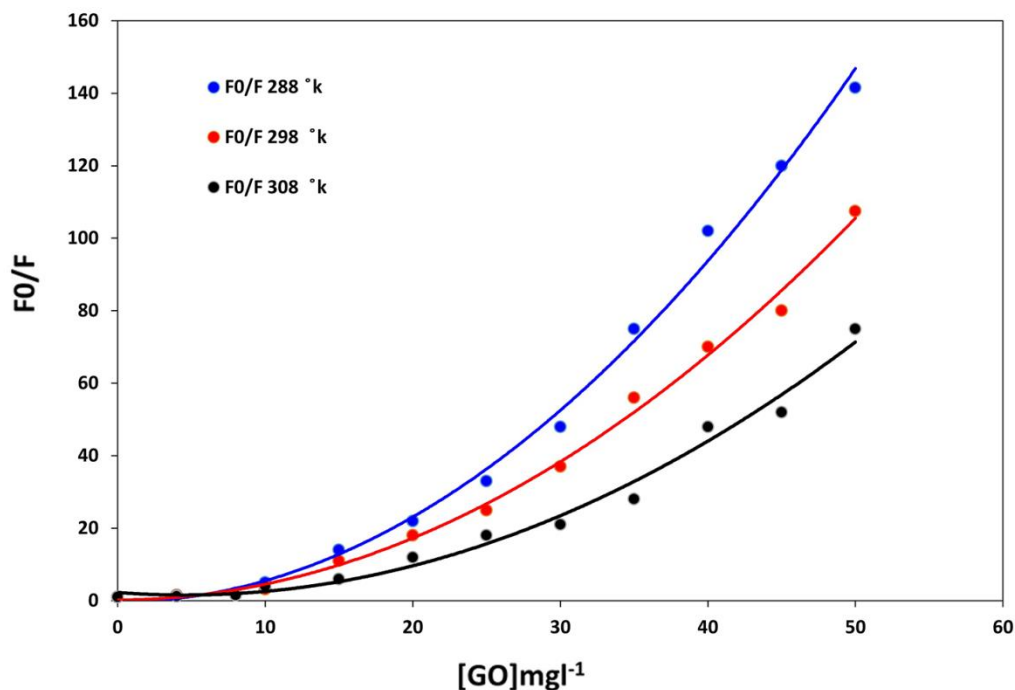
Figure 6: Fluorescence quenching of NDN2/ GO at different temperatures.

The resulting curves in Figure 6 show a nonlinear behavior with an upward curvature. It cannot be accurately fitted in the linear Stern-Volmer equation (Eq. 1). The modified equation (Eq. 2) has been introduced for a single species undergoing both dynamic quenching and ground-state complex static quenching [32]. K_S and K_D need to be determined in an analysis of the nonlinear steady-state fluorescence quenching model [34]. The measured K_S, K_D, and R^2 are evaluated from Figure 6 and given in Table 1.

$$F_0/F = (1+ K_S[Q])(1+ K_D[Q]) \qquad (2)$$

The number of binding sites between the fluorophore and GO can be evaluated by the site binding model (Eq. 3).

$$\log\left[\left(\frac{F_0}{F}\right)-1\right]=\log Kb+n\log[Q] \qquad (3)$$

Where K_b is the binding constant and n is the number of the binding site. Figure 7 shows the plots of $\log[(F_0-F)/F]$ versus $\log[Q]$ at different temperatures, and the corresponding values of k_b and n are given in Table 1. The correlation coefficient of the curves is larger than 0.95, indicating that the interaction between NN2 and GO agrees well with the site binding model underlying (Eq.3)

The result manifested that the binding constant kb decreased as the temperature increased, resulting in the destabilization of the GO-NOP complex. The unstable complex would be partly decomposed when the temperature is increased, and hence K_b value decreased. At the experimental temperature, the values of n at the experimental temperature were approximately equal to 1, which hinted that there was a single binding site in GO and NOP.

Table 1: Quenching parameters of graphene oxide and NN2 at different temperatures, Temperature (ºK).

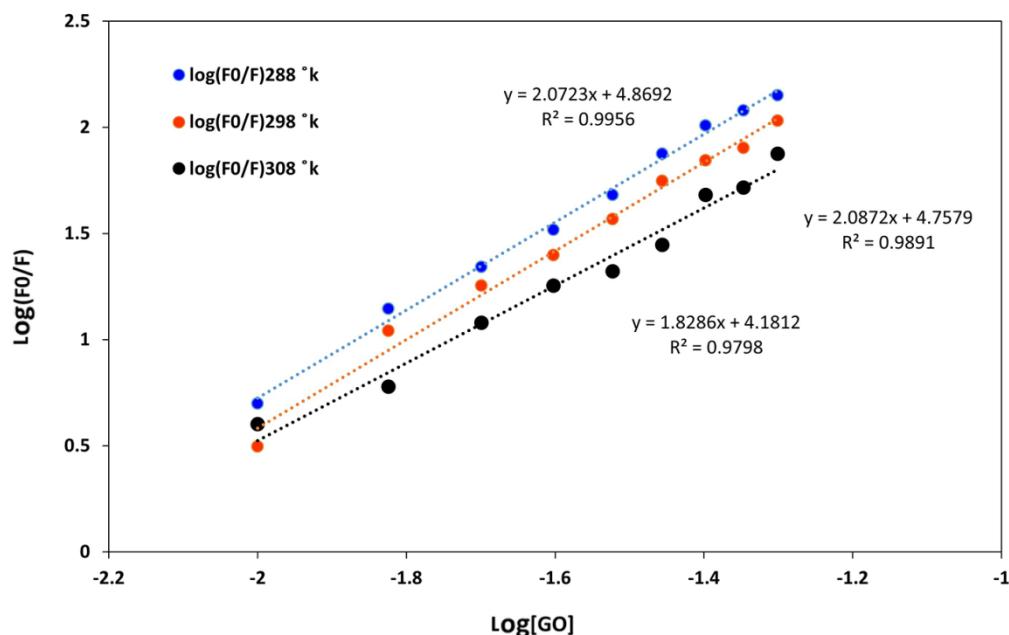| Temperature (ºK)	K_S	K_D	R^2	Log K_b	n	R^2
288	209.06	0.00030	0.98	1.59	2.11	0.96
298	128.83	0.00035	0.98	1.52	1.98	0.95
308	88.83	0.00033	0.96	1.37	1.76	0.95

Figure 7: Plots of log [(F$_0$ –F)/F] versus log [Q] at different temperatures.

The quenching of NN2 could occur through the following possible processes, an energy transfer or electron transfer. For an energy transfer via the FRET mechanism, an overlap between the absorption spectra of a quencher (acceptor) and the emission spectra of emissive species (donor) is needed. However, there is no overlap between the absorption spectra of GO (acceptor) and the emission spectra of NN2 (donor). Therefore, the FRET mechanism made energy transfer between NN2 and GO impossible. The fluorescence quenching of NN2 and GO seems to follow an electron transfer process. Further studies were performed to investigate the ground state and excited state energy levels of NN2. Cyclic voltammetry and UV-Vis spectra were used to calculate the band gap energy of GO and NN2. The energies obtained are -3.28 eV and -5.22eV for LUMO and HOMO energy levels of NN2, respectively. The calculated band gap, ΔE, is 1.94 eV for NN2. The reported valence bound of GO is to be -4.7 eV. Therefore, as shown in Figure 8, electron transfer is possible from the excited state of the NN2 to the GO plates. NN2 acts as a donor in the exited state to the graphene surface as an acceptor. The same behavior for GO and coumarin dye was reported previously [33].

3.5. Thermodynamic parameters

Generally, the binding constants are affected by temperature. Therefore, we follow the quenching process in different temperatures (288, 298, and 308 °k). From the value of the stability constant at different temperatures, the enthalpy can be calculated from the Van't Hoff equation (Eq. 4) based on the relationship between the binding constant (k) and temperature (T).
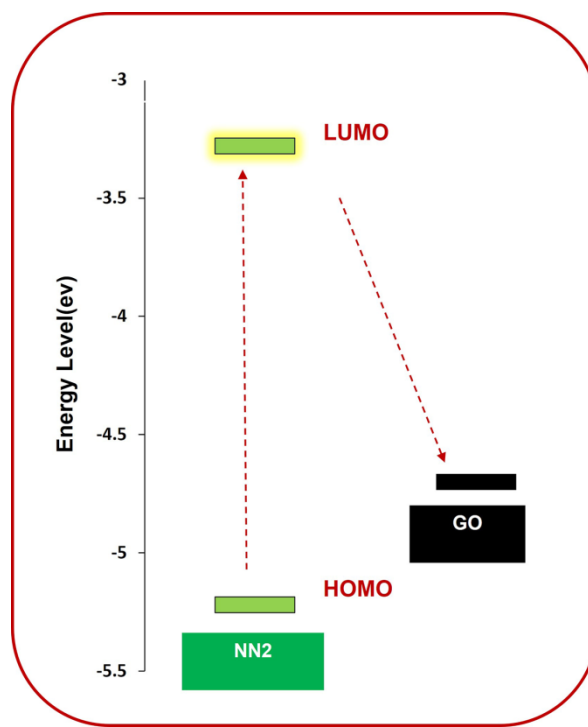
$$\Delta G = -2.303\ RT \log K \qquad (4)$$

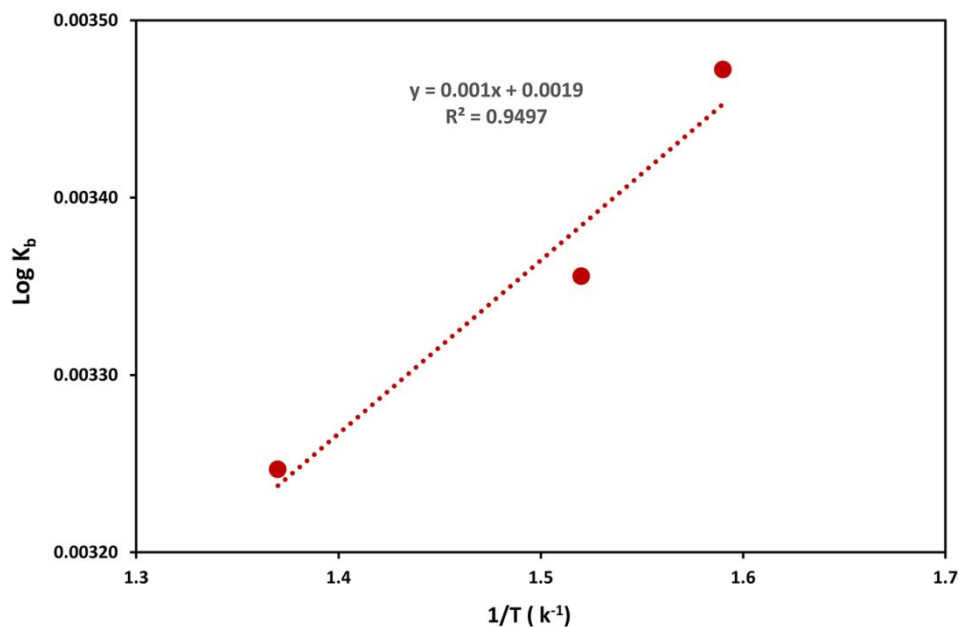**Figure 8:** Energy levels of NN2 and GO.

Figure 9: Plot of log K_{vs} vs. $1/T$.

Table 2: Thermodynamic parameters of NN2/GO quenching at (288,298 and 308 ºk)

Temperature (°K)	ΔG (KJ.mol⁻¹)	ΔH (J.mol⁻¹)	ΔS (J.mol⁻¹.K⁻¹)
288	-8.768	0.019	30.44
298	-8.673	0.019	29.10
308	-8.01	0.019	26.23

R is the gas constant, T is the temperature, and K is the binding constant [33]. The enthalpy (ΔH) of the complexation process was obtained from the slope of the plot of log K_b vs. $1/T$ using the graphical representation of Van't Hoff's equation (Figure 9), and the entropy (ΔS) could then be calculated as follows using Eq. 5.

$$\Delta G = \Delta H - T\Delta S \qquad (5)$$

The thermodynamic parameters of complex formation between NN2 and GO are included in Table 2. It seems that the enthalpy (ΔH) did not vary significantly over the studied temperature range, and cab assume it is constant. As can be seen, all the thermodynamic parameters are negative. The negative ΔG values confirm a spontaneous complexation process. The positive ΔS is evidence of a favorable entropy change during the complexation process.

4. Conclusions

GO efficiently interacts with NN2 via fluorescence quenching. Raman and FTIR investigations approved the adsorption of NN2 on the nano GO sheets. Fluorescence spectroscopy results also confirmed the efficient interaction between a donor and acceptor species combined with energy transfer followed by quenching of the fluorescence molecule. The results of the Stern-Volmer plot show that the primary quenching mechanism is a combination of static and dynamic quenching. The obtained binding constant of the quencher and fluorophore and the number of binding sites confirmed the presence of two sites for interaction. The binding study is of great importance in pharmacy and biochemistry. These experimental and theoretical results are potentially important in understanding the interaction mechanism between graphene and naphthalimide dye. They would be helpful guides for designing and developing efficient

graphene-based sensors. Also, the negative values of the ΔG confirm that the complexation process is spontaneous, and the positive entropy value confirms the favorable pathway process.

5. References

1. X. J. Lee, B. Y. Z. Hiew, K. C. Lai, L. Y. Lee, S. Gan, S. Thangalazhy-Gopakumar, S. Rigby, Review on graphene and its derivatives: Synthesis methods and potential industrial implementation, *J. Taiwan Inst. Chem. Eng.*, 98(2019), 163-180.

2. Y. Zhu, S. Murali, W. Cai, X. Li, J.W. Suk, J.R. Potts, R.S. Ruoff, Graphene and graphene oxide: synthesis, properties, and applications, *Adv. Mater.*, 22(2010), 3906-3924.

3. A. K. Geim, K. S. Novoselov, The rise of graphene, *Nat. Mater.*, 6(2007), 183-191.

4. D. Shahdeo, A. Roberts, N. Abbineni, S. Gandhi, Graphene based sensors, *Compreh. Anal. Chem.*, 91(2020), 175-199.

5. C. H. Lu, H. Yang, A graphene platform for sensing biomolecules, *Angew.Chem.*, 48(2009), 4785-4797.

6. E. Narvaez, A. Merkoci, Graphene oxide as an optical biosensing platform, *Adv. Funct. Mater.*, 24(2012), 3298-3308.

7. K. P. Loh, Q. Bao, G. Eda, M. Chhowalla, Graphene oxide as a chemically tunable platform for optical applications, *Nature Chem.*, 2(2010), 1015-1024.

8. Y. Zhau, X. Gang, Review on the graphene based optical fiber chemical and biological sensor, *Sensors Actuators B Chem.*, 231(2016), 324-340.

9. X. G. Gao, L. X. Cheng, W. S. Jiang, X. K. Li, F. Xing, Graphene and its derivatives-based optical sensors, *Front. Chem.*, 9(2021), 615164.

10. Z. Ifrah, A. Shah Rukh, S. Muhammad Nauman, S. Maryam, U. Rahat, Fluorescence quenching of graphene quantum dots by chloride ions: A potential optical biosensor for cystic fibrosis, *Front. Mater.*, 9(2022), 857432.

11. H. Chen, Q. Gao, J. Li, Jm. Lin, Graphene materials-based chemiluminescence for sensing, *J. Photochem. Photobiol. C: Photochem. Rev.*, 27(2016), 54-71.

12. N. A. A. Anas, Y. W. Fen, N. A. S. Omar, W. M. E. M. M. Daniyal, N. S. M. Ramdzan, S. Saleviter, Development of graphene quantum dots-based optical sensor for toxic metal ion detection, *Sensors,* 19(2019), 3850.

13. A. Kasry, A. A. Ardakani, G. S. Tulevski, B. Menges, M. Copel, L. Vyklicky, Highly efficient fluorescence quenching with graphene, *J. Phy. Chem. C,* 116(2012), 2858-2862.

14. X. Xiao, Y. Zhang, L. Zhou, B. Li, L. Gu, Photoluminescence and fluorescence quenching of graphene oxide: A review, *Nanomaterials,* 12(2022), 2444.

15. S. Kagatikar, D. Sunil, A systematic review on 1,8-naphthalimide derivatives as emissive materials in organic light-emitting diodes, *J. Mater. Sci.*, 57(2022), 105-139.

16. N. Jain, N. Kaur, A comprehensive compendium of literature of 1,8-naphthalimide based chemosensors from 2017 to 2021, *Coordin. Chem. Rev.*, 459(2022), 214454.

17. R. Tandon, V. Luxami, N. Tandon, K. Paul, Recent developments on 1,8-naphthalimide moiety as potential target for anticancer agents, *Bioorg. Chem.*, 121(2022), 105677.

18. D. Gudeika, A review of investigation on 4-substituted 1,8-naphthalimide derivatives, *Synthetic Metals.*, 262(2020), 116328.

19. M. Gharagozlou, S. Rouhani, A New reusable mercury-sensitive turn-on nano-chemosensor based on functionalized $CoFe_2O_4@SiO_2$ magnetic nano-composite, *Prog. Color Colorants Coat.,* 15(2022), 75-85.

20. S. Seraj, S. Rouhani, A fluorescence quenching study of naphthalimide dye by graphene mechanism and thermodynamic properties, *J. Fluores.*, 27(2017), 1877-1883

21. S. Seraj, S. Rouhani, F. Faridbod, Naphthalimide-based optical turn-on sensor for monosaccharide recognition using boronic acid receptor, *RSC Adv.*, 9(2019), 17933-17940.

22. S. Seraj, S. Rouhani, Synthesis and fluorescence quenching mechanism of novel naphthalimide derivative by nanographene oxide, *Chem. Phys. Lett.*, 780(2021), 138895.

23. C. Manivannan, R. Renganathan, A study on the fluorescence quenching of 9-Aminoacridine by certain antioxidants, *J. Luminescence.,* 131(2011), 2365-2371.

24. Y. Kitamoto, T. Namikawa, T. Suzuki, Y. Miyata, H. Kita, T. Sato, S. Oi, Dimesitylarylborane-based luminescent emitters exhibiting highly-efficient the\rmally activated delayed fluorescence for organic light-emitting diodes, *Org. Electron.*, 34(2016), 208-217.

25. F. T. Johra, J. Lee, W. Jung, Uv-vis characterization of GO: Facile and safe graphene preparation on solution based platform, *J. Indus. Eng. Chem.*, 20(2014), 2883-2887.

26. J. R. Lakowicz, Principles of fluorescence spectroscopy, Springer; 3rd edition, 2006.

27. W. R. Laws, P. B. Contino, Fluorescence quenching studies: Analysis of nonlinear Stern-Volmer data, *Methods Enzymology*, 210(1992), 448-463.

28. R. S. Swathi, K. L. Sebastian, Resonance energy transfer from a dye molecule to graphene, *J. Chem. Phys*., 129(2008), 054703.

29. R. S. Swathi, K. L. Sebastian, Long range resonance energy transfer from a dye molecule to graphene has (distance)− 4 dependence, *J. Chem. Phys*., 130(2009), 086101.

30. J. I. Paredes, S. Villar-Rodil, A. Martínez-Alonso, J.M. Tascon, Graphene oxide dispersions in organic solvents, *Langmuir*, 24(2008), 10560-10564.

31. J. R. Lakowicz, Topics in fluorescence spectroscopy, Plenum Press, New York, 2002 .

32. A. Airinei, R. I. Tigoianu, E. Rusu, D. O. Dorohoi, Fluorescence quenching of anthracene by nitroaromatic compounds, *Dig. J. Nanomater. Biostruct*., 6(2011), 1265-1272.

33. F. Galindo, M. Isabel Burguete, R. Gavara, S. V. Luis, Fluorescence quenching in organogel as a reaction medium, *J. Photochem. Photobiol. A: Chem.*, 178(2006), 57-61.

Gravimetric and Density Functional Theory Investigations on 4-Amioantipyrin Schiff Base as an Inhibitor for Mild Steel in HCl Solution

K. Mohsen Raheef[1], H. S. Qasim[2], A. A. Radhi[2], W. Kh. Al-Azzawi[3], M. M. Hanoon[2], A. A. Al-Amiery[4,5*]

[1.] Ashur University College, P.O. Box: 10001, Baghdad, Iraq.

[2.] Production and Metallurgy Engineering Department, University of Technology, P.O. Box: 10001, Baghdad, Iraq.

[3.] Department of Medical Instruments Engineering Techniques, Al-Farahidi University, P.O. Box: 10001, Baghdad, Iraq.

[4.] Department of Chemical and Process Engineering, Faculty of Engineering and Built Environment, Univerversiti Kebangsaan Malaysia, P.O. Box: 43600 UKM Bangi, Selangor, Malaysia.

[5.] Energy and Renewable Energies Technology Center, University of Technology-Iraq, P.O. Box: 10001, Baghdad, Iraq.

ABSTRACT

Metal corrosion, in general, is a serious economic problem. One of the most effective ways to prevent corrosion on metal surfaces is to use corrosion inhibitors, especially green organics. Here, the effects of concentration, exposure time, and temperature on the antiproliferative ability of 4-aminoantipyrine derivative were investigated. The 4-aminoantipyrine derivative showed significant corrosion resistance to mild steel melting in a 1M hydrochloric acid environment, as observed from the weight loss method. At 303 K and a dose of 500 ppm, the maximum inhibitory efficacy of the 4-aminoantipyrine derivative was 96.1 %. Corrosion test results showed that the 4-aminoantipyrine derivative has an inhibitory effect of more than 88 % at the concentration of 400 ppm and inhibits corrosion through an adsorption mechanism. The inhibitory potency of the 4-aminoantipyrine derivative changed inversely with a long exposure time, while temperature affected it directly. The Langmuir model was used to control the physical and chemical adsorption of its 4-aminoantipyrine derivative as a corrosion inhibitor on metallic surfaces. Data from density functional theory simulations help bridge the gap between theoretical studies and experimental approaches. Prog. Color Colorants Coat. 16 (2023), 255-269© Institute for Color Science and Technology.

1. Introduction

Mild steel is a material that is widely used in various manufacturing and construction processes, including design and construction. Unfortunately, one of the major problems with using mild steel is the material's susceptibility to corrosion [1]. Corrosion in structural steel is a natural but manageable phenomenon. Inhibitors are important additives to protect structural steel from corrosion. Pickling is a typical industrial cleaning process that removes scale and metal oxide deposits in oil drilling operations and petrochemical production. This process must be controlled as the mineral acids used are highly corrosive [2]. Organic molecules containing heteroatoms such as sulfur, oxygen, and nitrogen are effective corrosion inhibitors due to their ability to adsorb and inhibit active sites on metal substrates [3]. These organic inhibitors consist of two components, hydrophobic and hydrophilic, mostly

surfactants. Hydrophilic head groups (polar solvents) are usually ionizable and have a considerable affinity for water. Hydrophobic tails, on the other hand, are usually hydrocarbon (branched or linear). The head assembly can be attached to metal surfaces, forming a protective layer on the metal surface and protecting it from corrosion in acidic or corrosive liquids [4]. Environmentally friendly organic inhibitor technology has evolved in response to needs.

Despite their good efficiency, inorganic inhibitors (such as nitrate, chromate, phosphate, molybdate, etc.) are frequently used to prevent corrosion in structural alloys [5]. Theoretical chemical techniques are just as crucial as experimental techniques to identify corrosion inhibitors. Several quantum chemical factors can be used to interpret the activity of an inhibitor without the need for experimentation [6]. Quantitative chemical calculations can be used to produce materials that act as corrosion inhibitors between organic molecules. Atomic charges, molecular orbital energies, and energy are categories for the quantum chemical quantities often utilized in theoretical corrosion investigations [7]. In other words, it's important to determine corrosion inhibitor factors, including molecular activity, structure, and load. The molecule's potential structure may provide insight into the steric obstruction or how the inhibitor interacts with the metal solution interface. No studies have been reported on the 4-aminoantipyrine Schiff inhibitor used in this current study. This investigation aims to study the ability of the Schiff base "N-(4-amino-1,5-dimethyl-2-phenyl-1H-pyrazole-3 (2H) -ylidene)thiazol-2-amine" which is described in Figure 1 to the corrosion resistance of mild steel in 1 M hydrochloric acid solution using gravimetric techniques and DFT calculations.
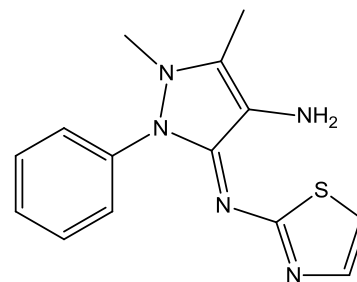.

Figure 1: Molecular structure of (E)-N-(4-amino-1,5-dimethyl-2-phenyl-1H-pyrazole-3 (2H)-ylidene)thiazol-2-amine.

2. Experimental

2.1. Synthesis of testes inhibitor

The synthesis of the corrosion inhibitor was based on the reference [8]. Equal volumes of 2-aminothiazole and 4-aminoantipyrene were refluxed into a sufficient volume of ethyl alcohol for 5 h, and the product was filtered and recrystallized from ethyl alcohol. Scheme 1 represents the outline synthesis of the target compound. The yield was 71 %, and the melting point was 180 °C. Chemical Formula: $C_{14}H_{15}N_5S$. Micro elemental analysis: C, 58.92 %; H, 5.30 %; N, 24.54 % (Calculated), C, 50.01%; H, 5.27 %; N, 24.47 % (Found). Proton NMR: δ 2.11 (3H, s), 3.49 (3H, s), 6.61 (1H, d, J=7.1 Hz), 7.19-7.24 (3H, dd, J=7.1 Hz), 7.48-7.61 (3H, dd, J=8.2, 7.9 Hz), 7.59 (d, J=3.2, 1.7 Hz)).

2.2. Mild steel preparation

A section of mild steel with composition (wt. %) of 0.01 Al, 0.05 Mn, 0.05 S, 0.09 F, 0.21 C, 0.38 Si, balance iron. Tested metal coupons cut to size 25×20× 0.3 mm were cleaned with silicon carbide paper of different grit from 320 to 1200. The cleaning process is based on ASTM G1-03 [8] technology.
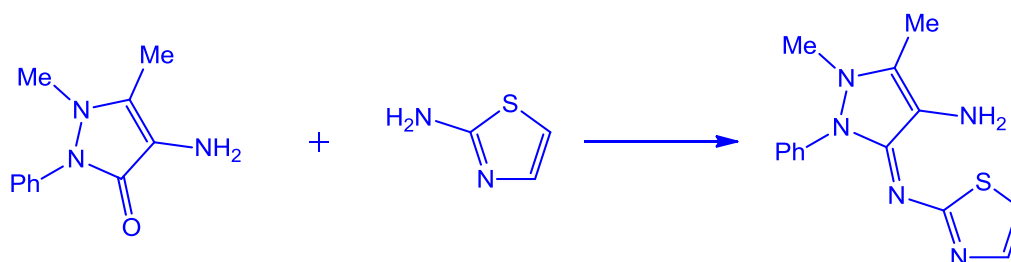
Scheme 1: The synthesis of the tested corrosion inhibitor.

2.3. Hydrochloric acid solution

The hydrochloric acid solution was 1 M HCl with different exposure times (1, 5, 10, 24, and 48 hours). Different inhibitor concentrations were 0.0, 100, 200, 300, 400, 500, and 1000 ppm. The temperatures used were 303, 313, 323, and 333 K.

2.4. Weight loss techniques

The weight loss indicates the difference in mass of the sample before and after it is exposed to an acidic environment. It has been evaluated at different temperatures, periods, and concentrations. Based on the data obtained and the formula equation, the wear rate was determined depending on the weight loss [9]. The corrosion rate was calculated as follows in equation 1:

$$C_R(mmpy) = 87600W/a\rho t \tag{1}$$

Where, W is the weight loss of the mild steel coupon (mg), a is the mild steel coupon area (cm^2), ρ is the mild steel coupon density (gcm^{-3}), and t is the immersion period (hours).

The inhibition efficiency was determined according to equation 2:

$$IE\% = 1 - \frac{C_{R(inh)}}{C_{R(blank)}} \times 100 \tag{2}$$

where, $C_{R(blank)}$ is the rate of corrosion of mild steel in the absence of the inhibitor, $C_{R(inh)}$ is the rate of corrosion of mild steel in the presence of the inhibitor.

Based on equation 3, the surface coverage area (θ) was determined for various inhibitor concentrations in corrosive solution from the weight loss measurements.

$$\theta = 1 - \frac{C_{R(inh)}}{C_{R(blank)}} \tag{3}$$

2.5. Quantum chemical calculations

The theoretical chemistry calculations have been conducted through Gaussian 09 [10]. The inhibitor structure in the gas phase was optimized using the B3LYP method, and the basis was set to "6-31G++" (d,p). As per Koopman's theorem [11], the ionization potential (I) and electron affinity (A) relate to E_{HOMO} and E_{LUMO}, respectively and were calculated using Equations 4 and 5, respectively:

$$I = -E_{HOMO} \tag{4}$$

$$A = -E_{LUMO} \tag{5}$$

Equations 6 to 11 were used to determine the electronegativity (χ), softness (σ), and hardness (η):

$$\chi = \frac{I+A}{2} \tag{6}$$

$$\eta = \frac{I-A}{2} \tag{7}$$

$$\sigma \sim \eta^{-1} \tag{8}$$

Equation 9 was applied to calculate the fractional number of transported electrons (ΔN), [10]:

$$\Delta N = \frac{\chi_{Fe} - \chi_{inh}}{2(\eta_{Fe} + \eta_{inh})} \tag{9}$$

The electronegativity value for iron (χ_{Fe}) was equal to 7 eV, whereas the hardness of iron η_{Fe} was equal to 0 eV as in equation 10:

$$N = \frac{7 - \chi_{inh}}{2(\eta_{inh})} \tag{10}$$

3. Results and Discussion

3.1. Inhibitor concentration and exposure time effects

At 303 K, I ran exposures of 1, 5, 10, 24, and 48 hours. 4-aminoantipyrine derivatives were exposed to hydrochloric acid environments at different concentrations to assess their effectiveness as green corrosion inhibitors. Figure 2 presents the results of the exposure procedure. Figure 2 shows that the inhibition efficiency improves with immersion time (up to 24 h) at the same concentration. The corrosion rate slows with increasing immersion time above 24 hours. The shape of the protective layer begins to decrease due to prolonged contact with the hydrochloric acid solution, the longer the exposure time is greater than 24 hours. The increase in metallic substrate mass, which lowers as more corrosive ions attack the metallic substrate, shows that the rate of corrosion increases as more hydrogen protons are generated. The amino group in the heterocyclic ring allows the 4-aminoantipyrine derivative to react with iron and other metal cations. The iron derivative 4-aminoantipyrine is created when the amino group combines with the Fe^{3+} ion. By sticking to the metal surface, the 4-aminoantipyrine derivative will stop further corrosion.
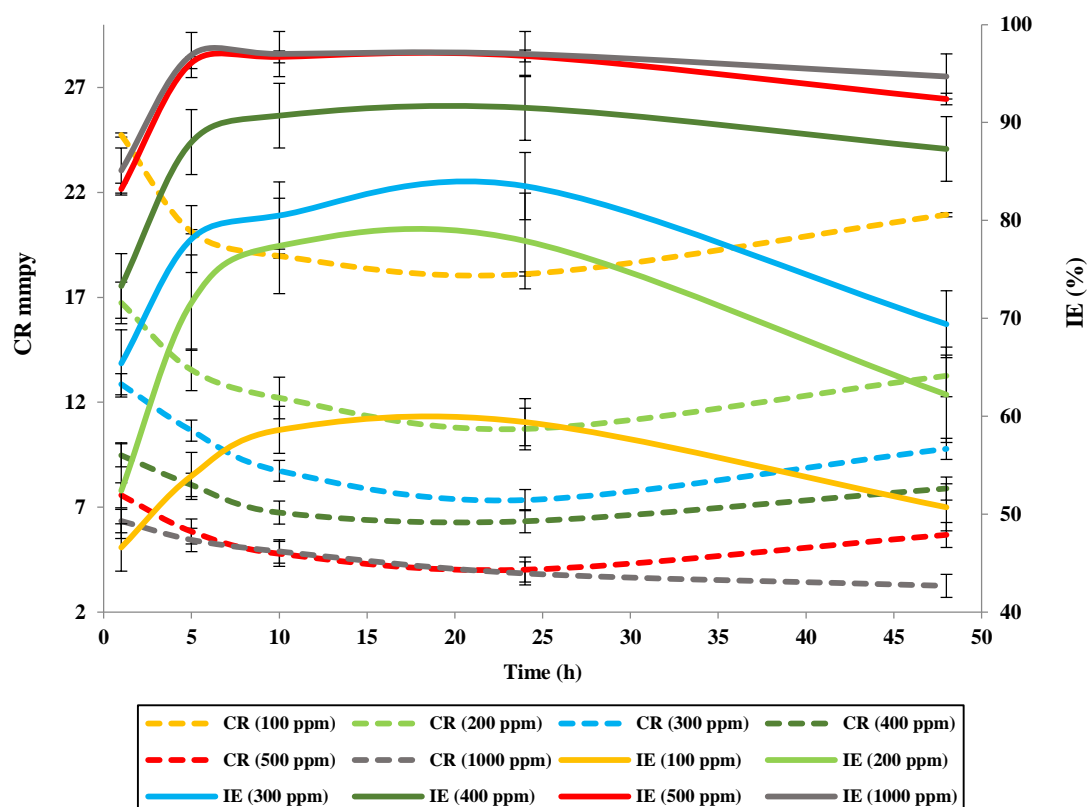
Figure 2: Exposure durations and inhibitor concentration against corrosion rate and inhibition efficiency at Temperature 303 K.

3.2. Temperature effects

Figure 3 displays the outcomes of the mass loss techniques computations together with inhibition efficiency values. Figure 3's study reveals how temperature affects inhibition effectiveness. As the HCl solution temperature rises, the inhibition's effectiveness decreases. The number of dissolving increases with temperature. Removing the inhibitor particles from the metal surface causes corrosion when the temperature rises. This event increases the surface area of mild steel in interface with the acidic environment and, in turn, increases the corrosion rate. In the presence of HCl, mild steel surface corrosion is followed by hydrogen gas generation. Because the complex molecule in the inhibitor solution adhering to the surface of mild steel to produce a protective barrier that can block corrosion attacks, the addition of inhibitor concentration can increase efficiency. The mild steel surface will adsorb the 4-aminoantipyrine derivative to a greater extent at higher concentrations, boosting the inhibitor's ability to prevent corrosion.

3.3. Adsorption isotherms

The degree of interaction between molecules of different inhibitors and the metal surface is explained by adsorption isotherms since the formation of protective films on metal surfaces resulted from molecules that have been adsorbed during organic corrosion inhibitors. It was determined that the inhibitory mechanism is adsorption using isotherm equations. Additionally, applying empirical equations like exponential, hyperbolic, logarithmic, and power to the known processes of the adsorption process is challenging to get the closest equation that connects the concentration of inhibitors to the adsorbed concentration at saturation. In addition to being straightforward, the Frumkin, Langmuir, and Temkin isotherms make it simple to use their parameters to characterize the corrosion inhibition system. [22].

Isotherm models are typically represented using equation 11 [23].

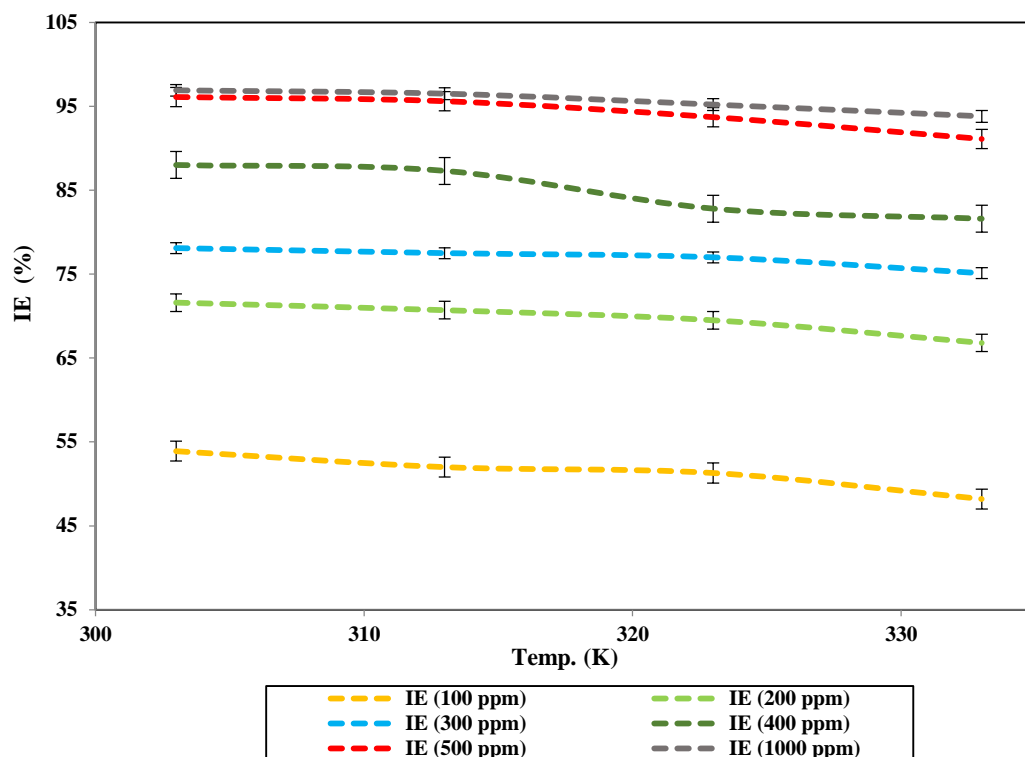$$f(\theta, \chi)\, exp(-a\theta) = KC \qquad (11)$$

Figure 3: Temperature and inhibitor concentrations against inhibition efficiency for exposure duration 5h.

Adsorption of particles onto the metallic surface always occurs in conjunction with the inhibitory mechanism [23]. Equation 3 was used to determine the percentage of the surface covered at any given time. The following isotherms were looked into for a proper understanding of the mechanism involved.

3.3.1. Langmuir model

The Langmuir isotherm is described by equation 12. K_{ads} is the adsorption-desorption constant, and θ is the surface coverage

$$\frac{C}{\theta} = \frac{1}{K_{ads}} + C \tag{12}$$

3.3.2. Frumkin model

The linear version of the Frumkin isotherm is represented by equation 13.

$$\log \frac{\theta}{1-\theta} = 2.303 \log k + 2\alpha\theta \tag{13}$$

3.3.3. Tempkin model

Equation 14 relates the concentration (C) of inhibition to the amount of surface coverage (θ). Constant K and

parameter (α) for the Tempkin isotherm at various temperatures and times were determined from Eq. 14 after linearization using the logarithmic transformation 14.

$$\log \frac{\theta}{C} = \log k + \alpha\theta \tag{14}$$

The conclusion drawn from the different isotherms was sufficient to describe the 4-aminoantipyrin derivative molecules' adsorption process and inhibitory ability at the interface between the corrosive environment and mild steel. The following isotherm plots' calculations provide significant findings: Due to significant R2 values and a slope that was near 1, Freundlich, Langmuir, and Temkin measurements at various temperatures showed that the process of 4-aminoantipyrin derivative adsorption on mild steel surfaces followed the Langmuir isotherm at all temperatures examined. According to the Langmuir equation, this suggests that the 4-aminoantipyrin derivative molecules are evenly distributed in monolayers on the surface of mild steel [25].

Figure 4's Langmuir isotherm plot, which depicts the K_{ads} value as a straight line between $log\ (C/\theta)$

and C_{inh}, was used to make this determination. The greater the adsorption and the more effective the inhibition, the higher the K_{ads} value, which measures how well an inhibitor molecule sticks to a metallic substrate [26]. The inhibitor that was tested had the highest K_{ads} value, suggesting that mild steel surfaces would be the best for adsorption. Equation 15 shows a relationship between the K_{ads} values and the common free energy of adsorption (ΔG^0_{ads}) determined by the relationship [27]:

$$\Delta G^0_{ads} = -RTln(55.5K_{ads}) \qquad (15)$$

When ΔG^0_{ads} becomes less than 20 kJ mol^{-1}, physical adsorption occurs between charges on inhibitor molecules and the mild steel surface. When ΔG^0_{ads} is greater than 40 kJ mol^{-1}, chemisorption occurs when unpaired electrons from the inhibitor molecules' heteroatoms transfer to the Fe-orbital on the metal surface to form a stable complex [28]. The ΔG^0_{ads}

was 37.85 kJ mol^{-1} This investigation demonstrates a broad range of adsorption (involving both physisorption and chemisorption). Chemisorbed molecules are anticipated to provide more effective shielding because they reduce the metal's inherent reactivity at the spots where they are linked. Thus, it is difficult to discriminate between chemisorption and physisorption using just the ΔG^0_{ads} value. In addition, inhibitors' physical adsorption on the metal surface takes place before their chemical adsorption [29].

3.4. DFT calculations

Quantum chemical simulations were carried out to examine the structural factors that affect the inhibition efficacy of inhibitors. The inhibitor's geometric and electrical structure was computed by maximizing its bond length. Figure 5 shows the optimal molecular structure with the lowest energy discovered using DFT computations.
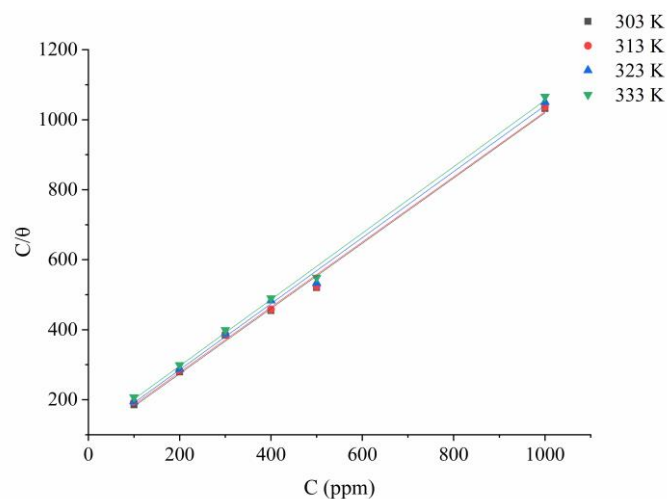

Figure 4: Langmuir isotherm models in treated solution at various temperature.
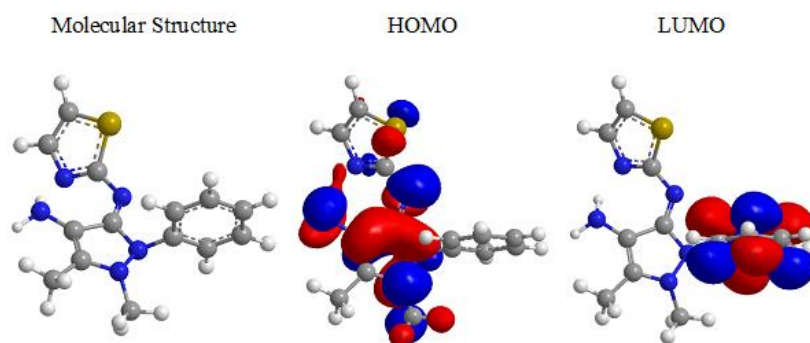

Figure 5: The neutral inhibitor at the optimal molecular structure, HOMO and LUMO, as determined by DFT/B3LYP/6-31G(d).

The following computations are used to determine quantum chemical variables: the highest occupied molecular orbital energy (EHOMO), the lowest-occupied molecular orbital energy (ELUMO), energy gap (ΔE), dipole moment (μ), electronegativity (χ), electron affinity (A), global hardness (η), softness (σ), ionization potential (I), the total energy (TE) and the fraction of electrons transferred from the inhibitor to mild steel surface (ΔN). These parameters are determined and presented in Table 1.

High values of EHOMO are likely to suggest a propensity of the molecule to donate electrons to suitable acceptor molecules with low energy and vacant molecular orbitals. The energy of HOMO is frequently related to the ability of a molecule to give electrons. As a result, the energy of the LUMO signal denotes the molecule's capacity to receive electrons [12, 13]. Therefore, the likelihood that the molecule will receive electrons increases with decreasing ELUMO values. With rising HOMO and falling LUMO energy values, the inhibitor's ability to attach to the metal surface increases. According to the calculations, the tested inhibitor had the lowest LUMO level or -1.113 eV, and the highest HOMO level, or -5.599 eV, which explained why increased HOMO and decreased LUMO energies are responsible for the highest inhibitory efficacy evaluated. The obtained results perfectly agree with the DFT simulation, which indicates that the evaluated inhibitor has significant inhibition potency. According to the study 4, the density for the tested inhibitor, HOMO, is primarily dispersed throughout the heterocyclic ring of 4-aminoantipyrine. The 4-aminoantipyrine's benzene ring is where the LUMO density is primarily concentrated.

The schematic diagram of frontier molecular orbitals for the tested inhibitor to its estimated energy gap, E, is shown in Figure 6. Corrosion inhibition is typically understood as the result of inhibitor molecules adhering to the metal surface. Two adsorption modes are conceivable. The interaction of electrically charged metal surfaces and charged species in most solutions is necessary for physical adsorption. The chemisorption mode implies charge sharing from the inhibitor molecule to the open orbitals of the metal with low energy. The effectiveness of the tested inhibitors and adsorption

parameters as a function of temperature revealed that the physisorption phenomena is more preferred [15, 16]. Therefore, in the study, the tested inhibitor effectively prevented mild steel from corroding in 1 M HCl. The evaluated inhibitor is regarded as a noteworthy effective inhibitor. According to the data, the tested inhibitor had a greater ΔE_{gap}. This parameter measures the stability of the generated complex on the metal surface. The stability of the produced complex is higher the lower the value of ΔE_{gap}. The tested inhibitor's ΔE_{gap} value is -4.486eV. The relationship between ΔE_{gap} and inhibition effectiveness is frequently highlighted in the literature as well. According to our theoretical findings, there is no connection between inhibitory effectiveness and ΔE_{gap}.

Also estimated was the number of electrons transported (ΔN). The values of (ΔN) revealed that Lukovits' study [17] agreed with the inhibitory efficiency of electron donation. The capacity of this inhibitor to give electrons to the metal surface is great, and if N 3.6, the inhibition efficiency rises by increasing the ability to donate electrons to the metal surface. The absolute value of ΔN may not reflect reality, but it does represent tendencies within a collection of molecules. The number of electrons that leave the donor and enter the acceptor molecule is not perfectly represented by the ΔN value.

Table 1: The 4-aminoantipyrine Schiff base theoretical parameters.

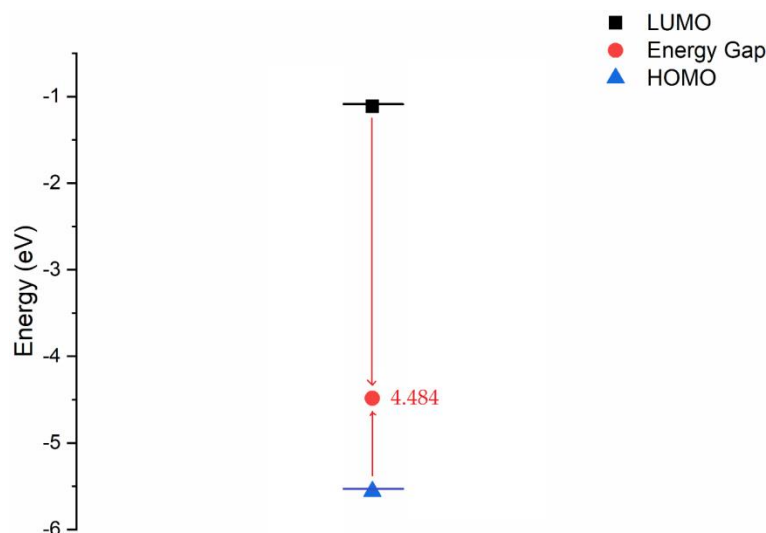| Quantum Chemical Parameters	Values
E_{HOMO} (eV)	-5.5999
E_{LUMO} (eV)	-1.113
ΔE_{gap}	-4.486
μ (Depye)	4.9834
χ	3.356
I	5.599
A	1.113
η	2.243
Σ	0.4458
ΔN	0.8123

Figure 6: Frontier molecular orbital correlation diagram for the evaluated inhibitor.
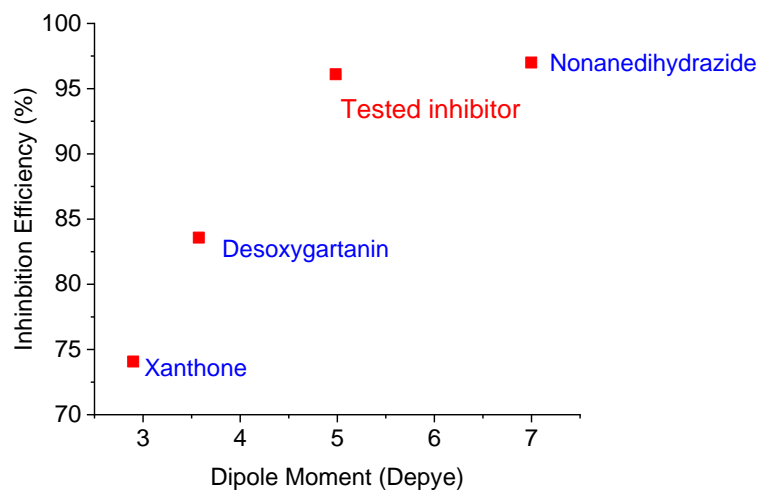

Figure 7: The relationship between the inhibitory performances and the dipole moments.

On the other hand, the molecule's dipole moment is the most frequently used parameter to explain polarity [18]. A covalently bonded bond's dipole moment serves as a measurement for its polarity. Its formula is the sum of the charges on the atoms and the separation of the two bound atoms. However, the total dipole moment only captures the overall polarity of a molecule. The vector sum of the individual bond dipole moments can be used to approximate the overall molecular dipole moment for a whole molecule. Theoretical research has demonstrated a strong correlation between the dipole moment and the effectiveness of the inhibition (Figure 7). Indeed, as the

dipole moment increases, the inhibition efficiency increase [19-21].

3.5. Inhibition mechanism

Organic molecules adsorb on the surface of steel to prevent corrosion. Nitrogen, oxygen, and the fused benzene ring are present in the 4-aminoantipyrine Schiff base molecules. It has been found that chemisorption and physisorption processes account for the majority of inhibitor adsorption on metallic substrate surfaces. Through donor–acceptor interactions with the empty Fe-orbitals, 4-aminoantipyrine Schiff base molecules are adsorbed onto the mild steel surface. The inhibitor's

nitrogen and oxygen atoms can transfer one pair of electrons to the unoccupied d-orbitals of the metal, forming a coordinating contact. In addition, the metal atom can make the same type of bond with the electrons of the aromatic rings. As shown in Figure 8, the metallic substrate/corrosive solution interface may have a potential blockage of the adsorption inhibitor molecules' process. Additionally, the d-orbitals of the iron atoms receive the free electrons from the nitrogen and oxygen atoms.

3.6. Comparison study

Table 2 demonstrates that the tested inhibitor N-(4-amino-1,5-dimethyl-2-phenyl-1H-pyrazole-3 (2H)-ylidene) thiazol-2-amine was a one-shot synthesis, has a substantial inhibiting efficiency when matched to several other produced inhibitors. The corrosion inhibitors in Table 2 were much more expensive to synthesize than the studied inhibitor because their protective effectiveness was proportionately lower or comparable, requiring numerous stages and expensive solvents.
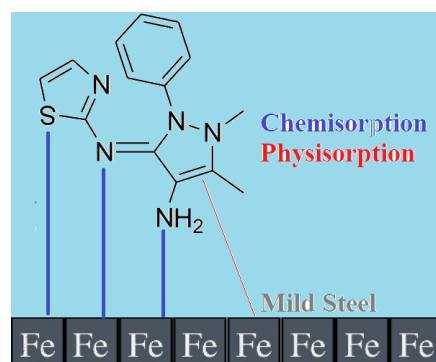
Figure 8: The proposed protected inhibited mechanism for the metallic substrate by Physisorption and Chemisorption methods.

Table 2: Compares the investigational inhibitor to verified steel inhibitors in hydrochloric acid solution.

Corrosion inhibition	Nature of adsorption	Alloy	Verified steel inhibitors	Ref.
96.1 %	Physisorption & chemisorption	Mild steel		-
91 %	Physisorption and chemisorption	Mild steel		[30]
98 %	Physisorption and chemisorption	Mild steel		[31]
94 %	Physisorption and chemisorption	Mild steel		[31]
96 %	Physisorption and chemisorption	Mild steel		[32]

Table 2: Continue.
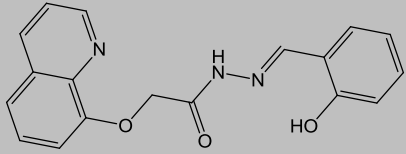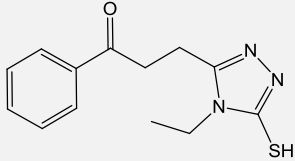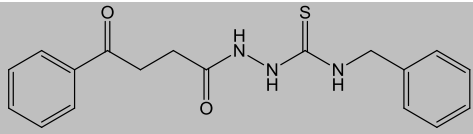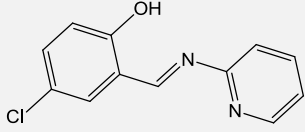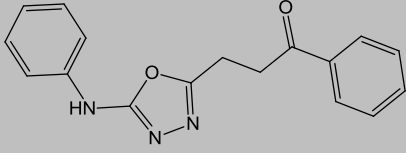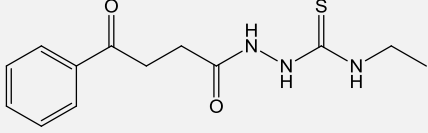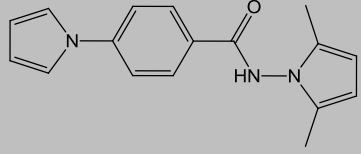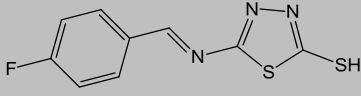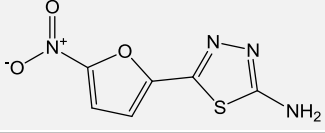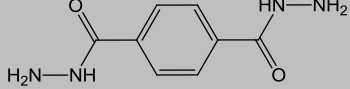
Corrosion inhibition	Nature of adsorption	Alloy	Verified steel inhibitors	Ref.
93%	Physisorption and chemisorption	Mild steel		[33]
97%	Physisorption and chemisorption	Mild steel		[34]
92%	Physisorption and chemisorption	Mild steel		[35]
91%	Physisorption and chemisorption	C. steel		[36]
95%	Physisorption and chemisorption	Mild steel		[37]
96%	Physisorption and chemisorption	Mild steel		[38]
95%	Physisorption and chemisorption	Mild steel		[39]
94%	Physisorption and chemisorption	Mild steel		[40]
91%	Physisorption and chemisorption	Mild steel		[41]
83%	Physisorption and chemisorption	Mild steel		[42]
96%	Physisorption and chemisorption	Mild steel		[43]

Table 2: Continue.

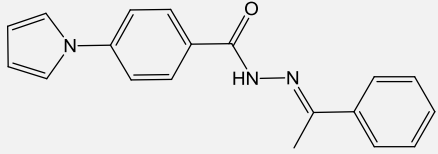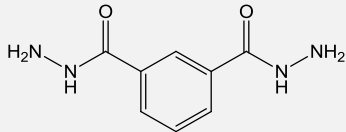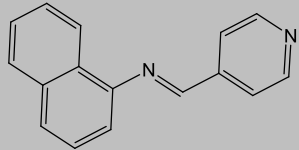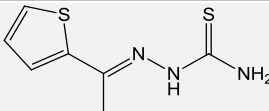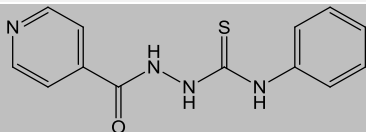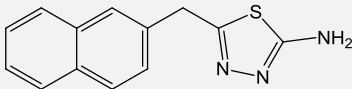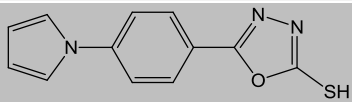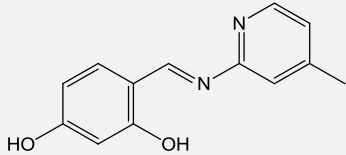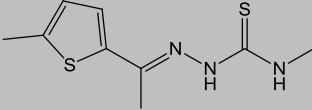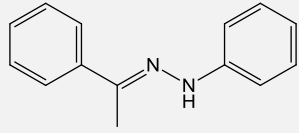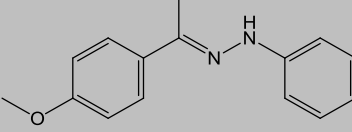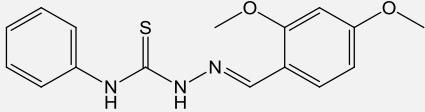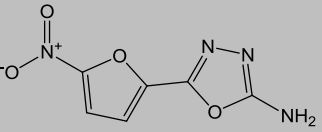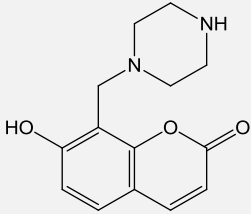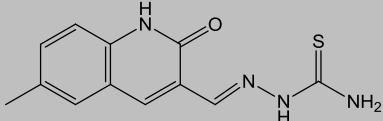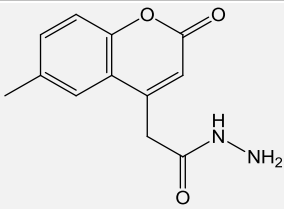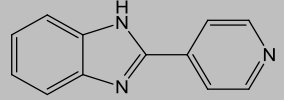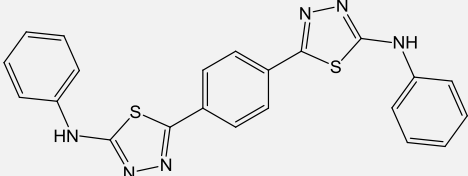| Corrosion inhibition	Nature of adsorption	Alloy	Verified steel inhibitors	Ref.
97 %	Physisorption and chemisorption	Mild steel		[44]
91 %	Physisorption and chemisorption	Mild steel		[45]
96 %	Physisorption and chemisorption	Mild steel		[46]
96 %	Physisorption and chemisorption	Mild steel		[47]
95 %	Physisorption and chemisorption	C. steel		[48]
95 %	Physisorption and chemisorption	Mild steel		[49]
93 %	Physisorption and chemisorption	C. steel		[50]
95 %	Physisorption and chemisorption	Mild steel		[51]
83 %	Physisorption and chemisorption	Mild steel		[52]
95 %	Physisorption and chemisorption	Mild steel		[53]
94 %	Physisorption and chemisorption	Mild steel		[54]
79 %	Physisorption and chemisorption	Mild steel		[55]

Table 2: Continue.

Corrosion inhibition	Nature of adsorption	Alloy	Verified steel inhibitors	Ref.
93 %	Physisorption and chemisorption	Mild steel		[56]
95 %	Physisorption and chemisorption	Mild steel		[57]
94 %	Physisorption and chemisorption	Mild steel		[58]
93 %	Physisorption and chemisorption	Mild steel		[59]
94 %	Physisorption and chemisorption	Mild steel		[59]

4. Conclusions

The current study aimed to assess the 4-aminoantipyrine Schiff base's effectiveness in inhibiting the corrosion of mild steel in hydrochloric acid solutions. Furthermore, to determine the effectiveness of the inhibition, the adsorption characteristics of the mild steel were investigated using weight loss methods. This event led to the classification of 4-aminoantipyrine Schiff base as a potent inhibitor with a promising inhibition efficiency of 96.1 %. The 4-aminoantipyrine Schiff base's chemical composition provided mild steel protection through physisorption and chemisorption. These findings were in agreement with the DFT used in this investigation.

5. References

1. G. E. Badr, The role of some thiosemicarbazide derivatives as corrosion inhibitors for C-steel in acidic media, *Corros. Sci.*, 51(2009), 2529-2536.
2. M. Goyal, S. Kumar, I. Bahadur, C. Verma, E. Ebenso, Organic corrosion inhibitors for industrial cleaning of ferrous and non-ferrous metals in acidic solutions: A review, *J. Mol. Liq.*, 256(2018), 565-573.
3. S. Ghareba, S. Omanovic, Interaction of 12-aminododecanoic acid with a carbon steel surface: towards the development of 'green' corrosion inhibitors, *Corros. Sci.*, 52(2010), 2104-2113.
4. A. Yıldırım, M. Cetin, Synthesis and evaluation of new long alkyl side chain acetamide, isoxazolidine and isoxazoline derivatives as corrosion inhibitors, *Corros. Sci.*, 50(2008), 155-165.
5. S. K. Saha, A. Dutta, P. Ghosh, D. Sukul, P. Banerjee, P. Novel Schiff-base molecules as efficient corrosion inhibitors for mild steel surface in 1 M HCl medium: experimental and theoretical approach, *Phys. Chem. Chem. Phys.*, 18(2016), 17898-17911.
6. X. Li, S. Deng, H. Fu, Three pyrazine derivatives as corrosion inhibitors for steel in 1.0 M H_2SO_4 solution,

Corros. Sci., 53(2011), 3241-3247.

7. M. Karelson, V. Lobanov, A. Katritzky Quantum-chemical descriptors in QSAR/QSPR studies, *Chem. Rev.*, 96(1996), 1027-1044.

8. J. Kumaran, S. Priya, J. Gowsika, N. Jayachandramani, S. Mahalakshmi, Synthesis, spectroscopic characterization, in silico DNA studies and antibacterial activites of Copper(II) and Zinc(II) complexes derived from thiazole based pyrazolone derivatives, *Res. J. Pharm. Biol. Chem. Sci.*, 4(2013), 279-288.

9. A.S.T.M. Standard, Standard practice for preparing, cleaning, and evaluating corrosion test specimens, American Society for Testing and Materials G1-03, (2011).

10. Gaussian 09, Revision D.01, M. J. Frisch, G. W. Trucks, H. B. Schlegel, G. E. Scuseria, M. A. Robb, J. R. Cheeseman, G. Scalmani, V. Barone, B. Mennucci, G. A. Petersson, H. Nakatsuji, M. Caricato, X. Li, H. P. Hratchian, A. F. Izmaylov, J. Bloino, G. Zheng, J. L. Sonnenberg, M. Hada, M. Ehara, K. Toyota, R. Fukuda, J. Hasegawa, M. Ishida, T. Nakajima, Y. Honda, O. Kitao, H. Nakai, T. Vreven, J. A. Montgomery, Jr., J. E. Peralta, F. Ogliaro, M. Bearpark, J. J. Heyd, E. Brothers, K. N. Kudin, V. N. Staroverov, R. Kobayashi, J. Normand, K. Raghavachari, A. Rendell, J. C. Burant, S. S. Iyengar, J. Tomasi, M. Cossi, N. Rega, J. M. Millam, M. Klene, J. E. Knox, J. B. Cross, V. Bakken, C. Adamo, J. Jaramillo, R. Gomperts, R. E. Stratmann, O. Yazyev, A. J. Austin, R. Cammi, C. Pomelli, J. W. Ochterski, R. L. Martin, K. Morokuma, V. G. Zakrzewski, G. A. Voth, P. Salvador, J. J. Dannenberg, S. Dapprich, A. D. Daniels, Ö. Farkas, J. B. Foresman, J. V. Ortiz, J. Cioslowski, and D. J. Fox, Gaussian, Inc., Wallingford CT, (2009).

11. T. Koopmans, Ordering of wave functions and eigenenergies to the individual electrons of an atom, *Physica*, 1(1933), 104-113.

12. L. Larabi, Y. Harek, O. Benali, S. Ghalem, Hydrazide derivatives as corrosion inhibitors for mild steel in 1 M HCl, *Prog. Org. Coat.*, 54(2005), 256-263.

13. Lukovits, E. Kálmán, F. Zucchi, Corrosion inhibitors-correlation between electronic structure and efficiency, *Corrosion*, 57(2001), 3-12.

14. A. Zarrouk, A. Dafali, B. Hammouti, H. Zarrok, S. Boukhris, M. Zertoubi, Synthesis, characterization and comparative study of functionalized quinoxaline derivatives towards corrosion of copper in nitric acid medium, *Int. J. Electrochem. Sci.*, 5(2010), 46-53.

15. A. Fiala, A. Chibani, A. Darchen, A. Boulkamh, K. Djebbar, Investigations of the inhibition of copper corrosion in nitric acid solutions by ketene dithioacetal derivatives, *Appl. Surf. Sci.*, 253(2007), 9347.

16. M. M. El-Naggar, Bis-aminoazoles corrosion inhibitors for copper in 40 M HNO$_3$ solutions, *Corros. Sci.*, 42(2000), 773.

17. Lukovits, E. Kálmán, F. Zucchi, Corrosion inhibitors-correlation between electronic structure and

18. efficiency, *Corrosion*, 57(2001), 11-23.

19. O. Kikuchi, Systematic QSAR procedures with quantum chemical descriptors, *Quant. Struct.-Act. Relat.*, 6(1987), 179.

20. K. Al-Azawi, S. Al-Baghdadi, A. Mohamed, A. Al-Amiery, T. Abed, S. Mohammed, A. Kadhum, A. Mohamad, Synthesis, inhibition effects and quantum chemical studies of a novel coumarin derivative on the corrosion of mild steel in a hydrochloric acid solution, *Chem. Central J.*, 10(2016), 1-9.

21. A. Al-Amiery, A. Mohamad, A. Kadhum, l. Shaker, W. Isahak, M. Takriff, Experimental and theoretical study on the corrosion inhibition of mild steel by nonanedioic acid derivative in hydrochloric acid solution, *Sci. Rep.*, 12(2022), 1-21.

22. F. Ramadhani, E. Emriadi, S. Syukri, Theoretical study of xanthone derivative corrosion inhibitors using density functional theory (DFT), *J. Kimia Valensi*, 6(2020), 96-105.

23. A. Singh, M. Quraishi, Effect of cefazolin on the corrosion of mild steel in HCl solution, *Corros. Sci.*, 52(2010), 152-160.

24. M. Ameer E. Khamis G. Al-Senani, Adsorption studies of the effect of thiosemicarbazides on the corrosion of steel in phosphoric acid, *Adsorpt. Sci. Technol.*, 8(2000), 177-194.

25. A. Yaro A. Khadom, R. Wael, Apricot juice as green corrosion inhibitor of mild steel in phosphoric acid, *Alexandria Eng. J.*, 52(2013), 129-135.

26. B. Meroufel O. Benali M. Benyahia Y. Benmoussa M. Zenasni, Adsorptive removal of anionic dye from aqueous solutions by algerian kaolin: characteristics, isotherm, kinetic and thermodynamic studies, *J. Mater. Environ. Sci.*, 3(2013), 482-491.

27. I. Ahamad, R. Prasad, M. Quraishi, Inhibition of mild steel corrosion in acid solution by Pheniramine drug: Experimental and theoretical study, *Corr. Sci.*, 52(2010), 3033-3041.

28. N. Kıcır, G. Tansuğ, M. Erbil, T. Tüken. Investigation of ammonium (2, 4-dimethylphenyl)-dithiocarbamate as a new, effective corrosion inhibitor for mild steel, *Corr. Sci.*, 105(2016), 88-99.

29. W. Li, Q. He, S. Zhang, C. Pei, B. Hou, Some new triazole derivatives as inhibitors for mild steel corrosion in acidic medium, *J. Appl. Electrochem.*, 38(2008), 289-295.

30. S. Zhang, Z. Tao, S. Liao, F. Wu, Substitutional adsorption isotherms and corrosion inhibitive properties of some oxadiazol-triazole derivative in acidic solution, *Corr. Sci.*, 52(2010), 3126-3132.

31. A. Alamiery, Study of corrosion behavior of N'-(2-(2-oxomethylpyrrol-1-yl) ethyl) piperidine for mild steel in the acid environment, *Biointerface Res. Appl. Chem.*, 12(2022), 3638-3646.

32. A. Alamiery, A. Mohamad, A. Kadhum, S. Takriff, Comparative data on corrosion protection of mild steel in HCl using two new thiazoles, *Data in Brief*, 40(2022), 107838.

33. A. M. Mustafa, F.F. Sayyid, N. Betti, L.M. shaker,

M. M. Hanoon, A.A. Alamiery, A.A.H. Kadhum, M.S. Takriff, Inhibition of mild steel corrosion in hydrochloric acid environment by 1-amino-2-mercapto-5-(4-(pyrrol-1-yl)phenyl)-1,3,4-triazole, *South African J. Chem. Eng.*, 39(2022), 42-51.

33. A. Alamiery, Investigations on corrosion inhibitory effect of newly quinoline derivative on mild steel in HCl solution complemented with antibacterial studies, *Biointerface Res. Appl. Chem.*, 12(2022), 1561-1568.

34. A. Aziz, I.A. Annon, M. Abdulkareem, M. Hanoon, M. Alkaabi, L. Shaker, A. Alamiery, W. Wan Isahak, M. Takriff, Insights into corrosion inhibition behavior of a 5-Mercapto-1, 2, 4-triazole derivative for mild steel in hydrochloric acid solution: experimental and DFT studies, *Lubricants*, 9(2021), 122.

35. A. Alamiery, W. Isahak, M. Takriff, Inhibition of mild steel corrosion by 4-benzyl-1-(4-oxo-4-phenylbutanoyl)thiosemicarbazide: gravimetrical, adsorption and theoretical studies, *Lubricants*, 9(2021), 93.

36. M.A. Dawood, Z.M.K. Alasady, M.S. Abdulazeez, D.S. Ahmed, G.M. Sulaiman, A.A.H. Kadhum, L.M. Shaker and A.A. Alamiery, The corrosion inhibition effect of a pyridine derivative for low carbon steel in 1 M HCl medium: Complemented with antibacterial studies, *Int. J. Corros. Scale Inhib.*, 10(2021), 1766-1782.

37. A. Alamiery, Corrosion inhibition effect of 2-N-phenylamino-5-(3-phenyl-3-oxo-1-propyl)-1,3,4-oxadiazole on mild steel in 1 M hydrochloric acid medium: Insight from gravimetric and DFT investigations, *Mater. Sci. Energy Technol.*, 4(2021), 398-406.

38. A. Alamiery, Short report of mild steel corrosion in 0.5 M H_2SO_4 by 4-ethyl-1-(4-oxo-4-phenylbutanoyl) thiosemicarbazide, *J. Tribologi*, 30(2021), 90-99.

39. A. Alamiery, Anticorrosion effect of thiosemicarbazide derivative on mild steel in 1 M hydrochloric acid and 0.5 M sulfuric Acid: Gravimetrical and theoretical studies, Mater. Sci. Energy Technol., 4(2021), 263-273.

40. A. Alamiery, W., Isahak, H. Aljibori, H. Al-Asadi, A. Kadhum, Effect of the structure, immersion time and temperature on the corrosion inhibition of 4-pyrrol-1-yl-n-(2,5-dimethyl-pyrrol-1-yl)benzoylamine in 1.0 m HCl solution, *Int. J. Corros. Scale Inhib.*,10(2021), 700-713.

41. A. Alamiery, E. Mahmoudi and T. Allami, Corrosion inhibition of low-carbon steel in hydrochloric acid environment using a Schiff base derived from pyrrole: gravimetric and computational studies, *Int. J. Corros. Scale Inhib.*, 10(2021), 749-765.

42. A.J.M. Eltmimi, A. Alamiery, A.J. Allami, R.M. Yusop, A.H. Kadhum, T. Allami, Inhibitive effects of a novel efficient Schiff base on mild steel in hydrochloric acid environment, *Int. J. Corros. Scale Inhib.*,10(2021),634-648.

43. A. Alamiery, L. Shaker, A. Allami, A. Kadhum, M. Takriff, A study of acidic corrosion behavior of Furan-Derived schiff base for mild steel in hydrochloric acid environment: Experimental, and surface investigation, Mate. Today: Proceedings, 44(2021), 2337-2341.

44. S. Al-Baghdadi, A. Al-Amiery, T. Gaaz, A. Kadhum, Terephthalohydrazide and isophthalo-hydrazide as new corrosion inhibitors for mild steel in hydrochloric acid: Experimental and theoretical approaches, *Koroze Ochrana Materialu*, 65(2021), 12-22.

45. M. Hanoon, A. Resen, L. Shaker, A. Kadhum, A. Al-Amiery, Corrosion investigation of mild steel in aqueous hydrochloric acid environment using n-(Naphthalen-1yl)-1-(4-pyridinyl)methanimine complemented with antibacterial studies, *Biointerface Res. Appl. Chem.*, 11(2021), 9735-9743.

46. S. Al-Baghdadi, T. Gaaz, A. Al-Adili, A. Al-Amiery, M. Takriff, Experimental studies on corrosion inhibition performance of acetylthiophene thiosemicarbazone for mild steel in HCl complemented with DFT investigation, *Intern. J. Low-Carbon Technol.*, 16(2021), 181-188.

47. A. Al-Amiery, Anti-corrosion performance of 2-isonicotinoyl-n-phenylhydrazinecarbothioamide for mild steel hydrochloric acid solution: Insights from experimental measurements and quantum chemical calculations, *Surface Rev. Letters*, 28(2021), 2050058.

48. M.S. Abdulazeez, Z.S. Abdullahe, M.A. Dawood, Z.K. Handel, R.I. Mahmood, S. Osamah, A.H. Kadhum, L.M. Shaker, A.A. Al-Amiery, Corrosion inhibition of low carbon steel in HCl medium using a thiadiazole derivative: weight loss, DFT studies and antibacterial studies, *Int. J. Corros. Scale Inhib.*, 10(2021), 1812-1828.

49. A. Mustafa, F. Sayyid, N. Betti, M. Hanoon, A. Al-Amiery, A. Kadhum, M. Takriff, Inhibition evaluation of 5-(4-(1H-pyrrol-1-yl)phenyl)-2-mercapto-1,3,4-oxadiazole for the corrosion of mild steel in an acidic environment: thermodynamic and DFT aspects, *Tribologia-Finnish J. Tribol.*, 38(2021), 39-47.

50. Y.M. Abdulsahib, A.J.M. Eltmimi, S.A. Alhabeeb, M.M. Hanoon, A.A. Al-Amiery, T. Allami, A.A.H. Kadhum, Experimental and theoretical investigations on the inhibition efficiency of N-(2,4-dihydroxytolueneylidene)-4-methylpyridin-2-amine for the corrosion of mild steel in hydrochloric acid, *Int. J. Corros. Scale Inhib.*, 10(2021), 885-899.

51. A. Khudhair, A. Mustafa, M. Hanoon, A. Al-Amiery, L. Shaker, T. Gazz, A. Mohamad, A. Kadhum, M. Takriff, Experimental and theoretical investigation on the corrosion inhibitor potential of N-MEH for mild steel in HCl, *Prog. Color Colorants Coat.*, 15(2021), 111-122.

52. D. Zinad, R. Salim, N. Betti, L. Shaker, A. AL-Amiery, Comparative investigations of the corrosion inhibition efficiency of a 1-phenyl-2-(1-phenylethylidene)hydrazine and its analog against mild steel corrosion in hydrochloric acid solution, *Prog. Color Colorants Coat.*, 15(2021), 53-63

53. R. Salim, N. Betti, M. Hanoon, A., Al-Amiery, 2-(2,4-Dimethoxybenzylidene)-N-

phenylhydrazinecarbothioamide as an efficient corrosion inhibitor for mild steel in acidic environment, *Prog. Color Colorants Coat*., 15(2021), 45-52.

54. A. Al-Amiery, L. Shaker, A.M. Takriff, Exploration of furan derivative for application as corrosion inhibitor for mild steel in hydrochloric acid solution: Effect of immersion time and temperature on efficiency, *Mater. Today: Proc.*,42(2021), 2968-2973.

55. A.M. Resen, M.M. Hanoon, W.K. Alani, A. Kadhim, A.A. Mohammed, T.S. Gaaz4, A.A.H. Kadhum, A.A. Al-Amiery, M.S. Takriff, Exploration of 8-piperazine-1-ylmethylumbelliferone for application as a corrosion inhibitor for mild steel in hydrochloric acid solution, *Int. J. Corros. Scale Inhib.*, 10(2021), 368-387.

56. M. Hanoon, A., Resen, A. Al-Amiery, A. Kadhum, T. Takriff, Theoretical and experimental studies on the corrosion inhibition potentials of 2-((6-Methyl-2-ketoquinolin-3-yl)Methylene) hydrazinecarbothioamide for mild steel in 1 M HCl, *Prog. Color Colorants Coat*., 15(2021), 21-33.

57. F. Hashim, T. Salman, S. Al-Baghdadi, T. Gaaz, A. Al-Amiery, Inhibition effect of hydrazine-derived coumarin on a mild steel surface in hydrochloric acid, Tribologia, , 37(2020), 45–53

58. A.M. Resen, M. Hanoon, R.D. Salim, A.A. Al-Amiery, L.M. Shaker, A.A.H. Kadhum, Gravimetrical, theoretical, and surface morphological investigations of corrosion inhibition effect of 4-(benzoimidazole-2-yl) pyridine on mild steel in hydrochloric acid, *Koroze Ochrana Materialu*, 64(2020), 122-130.

59. A. Salman, Q. Jawad, K. Ridah, L. Shaker, A. Al-Amiery, Selected BIS-Thiadiazole: synthesis and corrosion inhibition studies on mild steel in HCl environment, *Surf. Rev. Lett.*, 27(2020), 2050014

Facile One-pot Synthesis of Binder-free MnCo$_2$O$_4$ Nanosheets as Efficient Supercapacitor Electrode Material

Z. Norouzi, S. H. Mahmoudi Najafi, S. A. Mozaffari*

Department of Chemical Technologies, Iranian Research Organization for Science and Technology (IROST), P.O. Box: 33535-111, Tehran, Iran

ABSTRACT

*T*he engineered nanostructured electrode material is an important factor in enhancing the performance of supercapacitors. Herein, a facile procedure was reported for the electrosynthesis of MnCo$_2$O$_4$ nanosheets through one-pot electrodeposition method. The obtained MnCo$_2$O$_4$ nanosheets have been characterized using field-emission scanning electron microscopy (FE-SEM), X-ray diffraction (XRD), and energy-dispersive X-ray spectroscopy (EDX) techniques. The results showed that MnCo$_2$O$_4$ nanosheets with multiple walls had been successfully prepared. The electrochemical evaluation revealed that the as-prepared MnCo$_2$O$_4$ electrode delivered a high specific capacitance of 1198 mF cm^{-2} at the current density of 1 mA cm^{-2} and demonstrated outstanding cycling performance. The binary nature of the MnCo$_2$O$_4$ nanosheets, along with the unique nanosheet architecture with accessible void spaces for the transfer of electrolyte ions and electrons, is responsible for these remarkable properties. These results demonstrate that the present MnCo$_2$O$_4$ nanosheets with outstanding electrochemical properties can be considered as promising candidates for energy storage systems. *Prog. Color Colorants Coat. 16 (2023), 271-281© Institute for Color Science and Technology.*

1. Introduction

Rapid reduction of fossil fuel supplies and the increase of greenhouse gases have caused a severe threat to the ecology of the earth. Also, with the increase of power demand for portable electronics, developing renewable and clean energy resources is necessary [1, 2]. In this regard, supercapacitors have attracted significant research interests from both industry and science due to their high power density, long cycle life, safe operation, and environmental friendliness [3] as backup/auxiliary power supplies of portable electronics, smart grids [4, 5], hybrid electric vehicles, and several micro-devices [6, 7].

Supercapacitors (i.e., electrochemical capacitors) can store charges on highly porous electrode materials. According to the charge storage mechanisms, they can be categorized into electrical double-layer capacitors (EDLCs) and pseudocapacitors [8]. The EDLC version is the most common type of supercapacitors and stores charges at the interface of electrode/electrolyte based on Helmholtz law. The pseudocapacitor version stores charges based on electrochemical reactions [9].

Many efforts have been made to develop high-performance electrode materials with low cost and high capacitance. The specific surface area of the electrode materials should be increased to increase the specific capacitance of supercapacitors. In this case, the EDLC capacitances promoted and imparted many electroactive

sites for participation in the electrochemical reaction. Furthermore, the suitable pore size distribution of the porous electrode materials facilitates the mass transfer of electrolyte ions through the pores for fast faradaic reactions and EDLC charging/discharging [10]. Hence, control over the dimensions and morphology of electrode material is vital for achieving high-performance supercapacitors [11].

Despite architecture, the material selection also plays an essential role in the performance of supercapacitors. Transition metal oxides (TMOs) and hydroxides, and conducting polymers as pseudocapacitor electrode materials offer higher electrochemical performances than carbonaceous materials (EDLC type) due to the contribution of redox reactions [12, 13]. Using binary transition metal oxides compared to single-component metal oxides is significant in enhancing electrochemical performance since they have different oxidation states and provide richer faradaic reactions, resulting in higher capacitances compared than single-metal oxides [14]. Among the most binary metal oxides, $MnCo_2O_4$ has been recognized as an attractive electrode material due to its higher electrochemical performance than unitary manganese oxide (MnO_2) and cobalt oxide (Co_3O_4) [15].

Till now, different Mn-Co oxide morphologies, such as $MnCo_2O_4$ nanorods [16], $MnCo_2O_4$ core-shell structures [17], and $MnCo_2O_4$ hollow nanotubes [18], have been reported for supercapacitor applications. Between different morphologies, 3D nanosheets directly grown on conductive substrates are considered an ideal architecture for supercapacitor application. They possess high electroactive sites and thin wall thickness, allowing easier electron transfer [19, 20]. A significant challenge in using $MnCo_2O_4$ as the electrode material in a supercapacitor is improving its electroactive sites by developing a facile one-pot route. Therefore, specific capacitance and cycling stability are enhanced [21]. Binders and additives used in the fabrication of electrodes usually block the electroactive sites of the electrode material and decrease the total efficacies [22]. Direct growth of nanosheets on conductive current collectors enhances the conductivity of the electrode materials by close contact of nanosheets to the current collector. Such a design does not require further additives or binders [19]. So, it is critically important to develop a facile approach for the synthesis of nanosheet electrode materials. Nickel foam substrates could be used as both current collector and structure support, and

the electrode materials could be directly grown on them. In electrosynthesis, no binder and additive are used to prepare electrodes to prevent "dead" volume resulting from the tedious process of mixing active ingredients with polymer binder/conductive additives, and the total mass of the final device could be reduced.

A possible approach for decreasing the mass loading issues is precisely designing the $MnCo_2O_4$-based nano-architectures with a facile and cost-effective electrodeposition method to fulfill the requirement of high-rate supercapacitors [23]. Electrodeposition is a versatile method for fabricating porous electrode materials, which could produce many nano-architectures by tuning the processing factors [24].

To the best of our knowledge, the direct growth of $MnCo_2O_4$ nanosheets on Ni foam current collector has rarely been reported. Herein, we designed a facile, one-pot route for electro-synthesizing of 3D $MnCo_2O_4$ nanosheet arrays on the conductive substrate as an efficient binder-free electrode with enhanced surface area and easy ion and electron diffusion path. This method provides a higher utilization rate of the electrode material for high-rate supercapacitors. The resultant electrode revealed ultrahigh specific capacitance (1198 mF cm^{-2} at 1 mA cm^{-2}) and excellent cycle life (97 % capacitance retention after 2000 cycles at the scan rate of 250 mV s^{-1}), which is desired for energy storage applications.

2. Experimental

2.1. Synthesis of 3D $MnCo_2O_4$ nanosheets

All the reagents and chemicals were of analytical grade and were used without further purification. $MnCo_2O_4$ was synthesized through electrochemical deposition from the solution containing 5 mM $MnCl_2.6H_2O$, 5 mM $CoCl_2.6H_2O$, and 0.1 M KCl. Before electrodeposition, Ni foam was washed ultrasonically with alcohol, acetone, and deionized water for 10 min, respectively. All experiments were performed in a three-electrode configuration using cleaned Ni foam as the working electrode, Pt wire and Ag/AgCl as the auxiliary and reference electrodes, respectively. A potential of -1.0 V was applied against the Ag/AgCl for the duration of 120 and 1200 s. Then the samples were washed with distilled water several times and annealed at 200 °C for 30 min with temperature programming of 5 °C min^{-1}.

2.2. Characterization

The morphology and textural parameters of the nanosheets were monitored using field-emission scanning electron microscopy (FE-SEM, MiraII from TESCAN Company) equipped with energy-dispersive X-ray spectroscopy (EDX). The crystalline structure and purity of the prepared electrode were monitored by X-ray diffraction (XRD) using Philips PW 1730 diffractometer equipped with a Cu-K$_\alpha$ (λ=0.15418 nm) radiation source. Data were collected by scanning in the range of 10 ° to 80 ° with a step size of 0.05 ° (2θ) under grazing incidence mood.

2.3. Electrochemical measurement

The electrochemical tests were carried out at room temperature. The conventional three-electrode cell was used, which is connected to an Autolab PGSTAT.302N potentiostat/galvanostat (Eco-Chemie, The Netherlands). The deposited MnCo₂O₄ nanosheets on Ni foam substrate, Ag/AgCl electrode, and Pt plate were used as the working, reference, and auxiliary electrodes, respectively, in a solution of 3 M KOH as the electrolyte.

3. Results and Discussion

3.1. Synthesis and surface morphology analysis

A facile one-pot approach was used to deposit 3D MnCo₂O₄ nanosheets on Ni foam substrate (Figure 1) as an effective binder-free electrode. The electrodeposition bath contained a solution of MnCl₂.6H₂O, CoCl₂.6H₂O, and KCl. It took only 1200 s to deposit nanostructures with high specific capacitance completely. In practice, the weight of the cell is important, which could be affected by the electrolyte, binder, separator, collectors, and packaging material. The binder sticks the electrode materials on the substrate in both batteries and supercapacitors. However, the conductive additive is used to improve the electrical conductivity of the laminate. Using insulating polymeric binders increases the contact resistance between electroactive materials, which results in increased equivalent series resistance (ESR) value in the final device [25]. The binders and additives together constitute 20–40 % of the total mass of the electrode, namely 'dead mass', since it does not participate in charge storage, but instead lowers the specific energy of the final device. Besides, the diffusion path of ions and electrons is ambiguous due to the heterogeneous nature of the mixture, which results in low specific power and slow rate performance. The binder-less electrodes provide some advantages, comprising low weight, diverse macroscopic structures, well-defined pore size and distribution, and mechanical stability. It also offers higher output voltage and fast energy storage [26, 27]. Besides, such a design eliminates the need for expensive binders and additives, which reduces the cost and avoids the difficulty in electrode preparation processes.
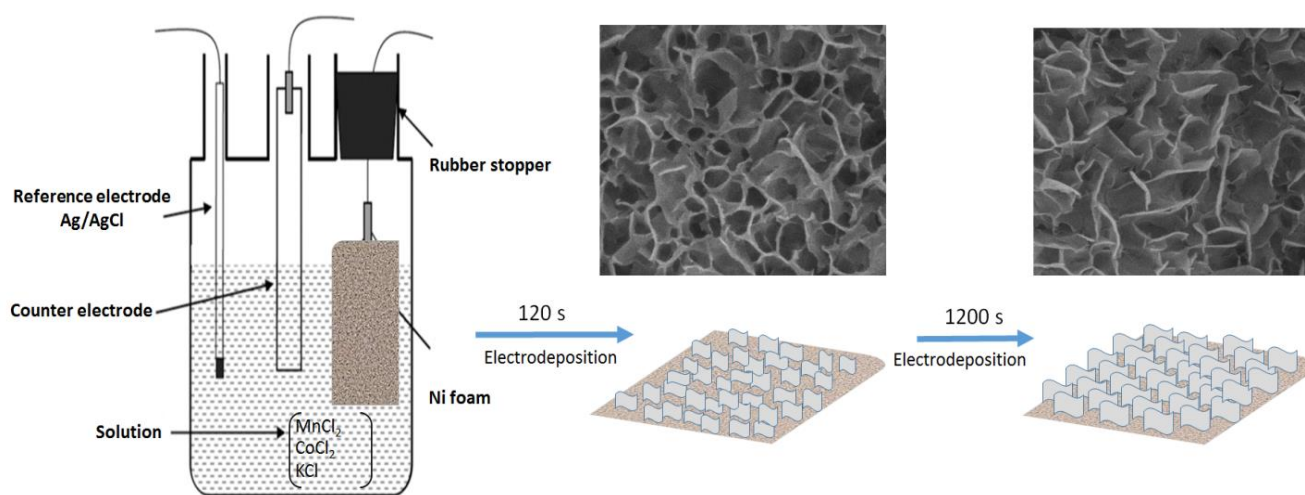
Figure 1: Schematic illustration of MnCo₂O₄ nanosheets synthesis.

FE-SEM is used to study the morphological features of the prepared electrodes. Figures 2a and b displays the FE-SEM images of the $MnCo_2O_4$ nanosheets on Ni foam substrate after 120 s. As shown, the nanosheet morphology was growing. The well-defined nanosheet morphology could be fully imaged by increasing the reaction time to 1200 s (Figures 2c and d. The $MnCo_2O_4$ nanosheets were vertically aligned and intertwined and formed 3D nanosheet arrays, which grew densely on the Ni foam substrate. After annealing at 200 °C, the $MnCo_2O_4$ keeps the wall-like architecture of the original morphology and becomes narrower. Figures 2e and f displays the SEM images of the $MnCo_2O_4$ nanosheets after annealing.

The water has evaporated, and many open pores can be detected on the $MnCo_2O_4$ nanosheet surface. The 3D nanosheet structures obtained by electrodeposition clarify a high superficial area with an open mesoporous structure.

The nanosheets have an average diameter and length of about 15-30 nm and 1 μm, respectively (Figure 2F). With such a fascinating structure, the voids between the 3D $MnCo_2O_4$ nanosheet arrays can be efficiently utilized. Such a design shortens ion diffusion pathways [28]. It provides a fast ion and charges transportation path during the faradaic reactions and many electroactive sites for trapping and accumulating electrolyte ions [29].
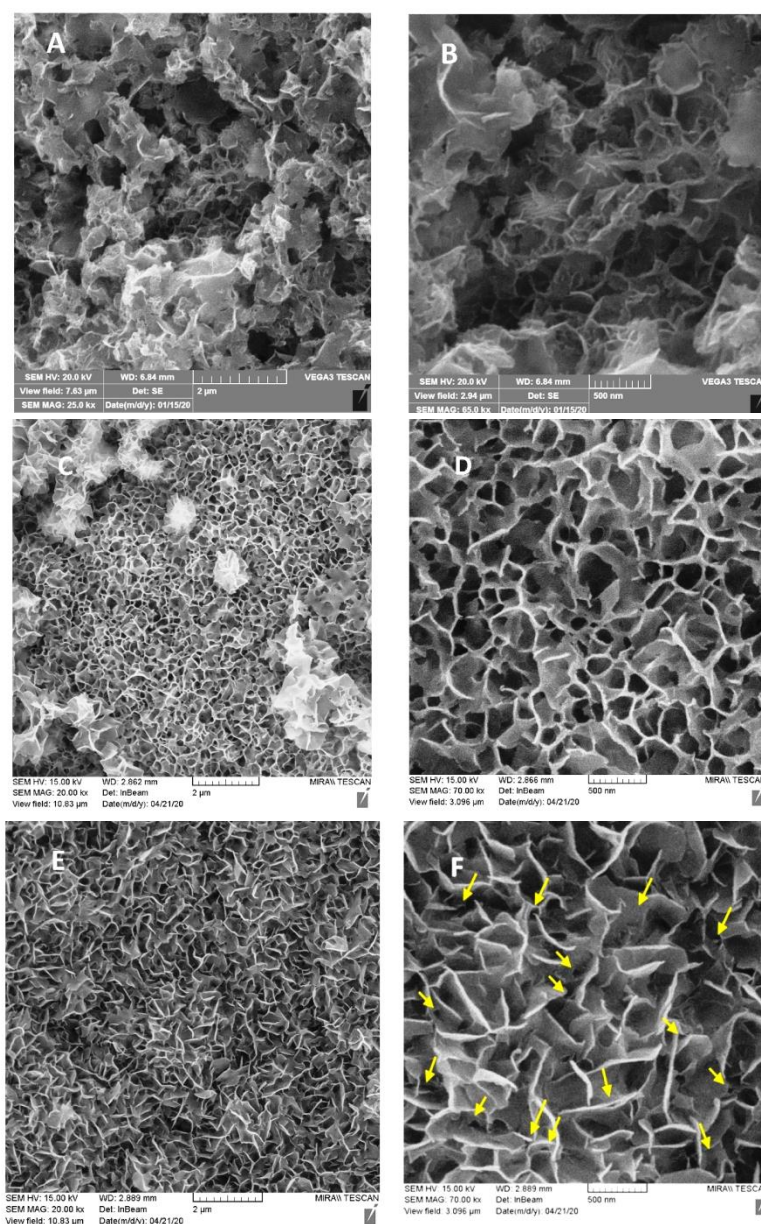
Figure 2: SEM images of $MnCo_2O_4$ nanosheets (A, B) after 120 s, (C, D) after 1200 s without annealing, (E, F) after 1200 s with annealing. Yellow arrows indicate some mesopores.

3.2. Crystalline structure

The elemental composition and crystalline structure of the prepared electrode were monitored by EDX and XRD analyses. The EDX spectrum in Figure 3a displays the presence of Mn, Co, and O elements. It can be seen in the XRD pattern (Figure 3b) that the intensity of three peaks at 44.5, 51.8, and 76.4 is much higher than the other peaks, which correspond to (1 1 1), (2 0 0), and (2 2 0) crystal facet of nickel in Nickel foam (JCPDS card no. 04-0850). The weak diffraction peaks appeared at 63.3° and 66.8°, which is consistent with (4 4 0), (5 3 1) crystal faces of spinel $MnCo_2O_4$

(JCPDS card no. 23–1237) as has been reported in the other references [30-33]. In most of the research reports, the XRD patterns of $MnCo_2O_4$ nanoscale compounds on nickel foam were very noisy, and the reflection peaks had low intensities. Also, maybe some reflection peaks of Co were hidden under Ni reflection peaks.

The sample with the less intense diffraction peak shows that the scale of the nanostructure is small, which can increase the number of effective electrochemical reaction points to improve the electro-chemical performance [34].
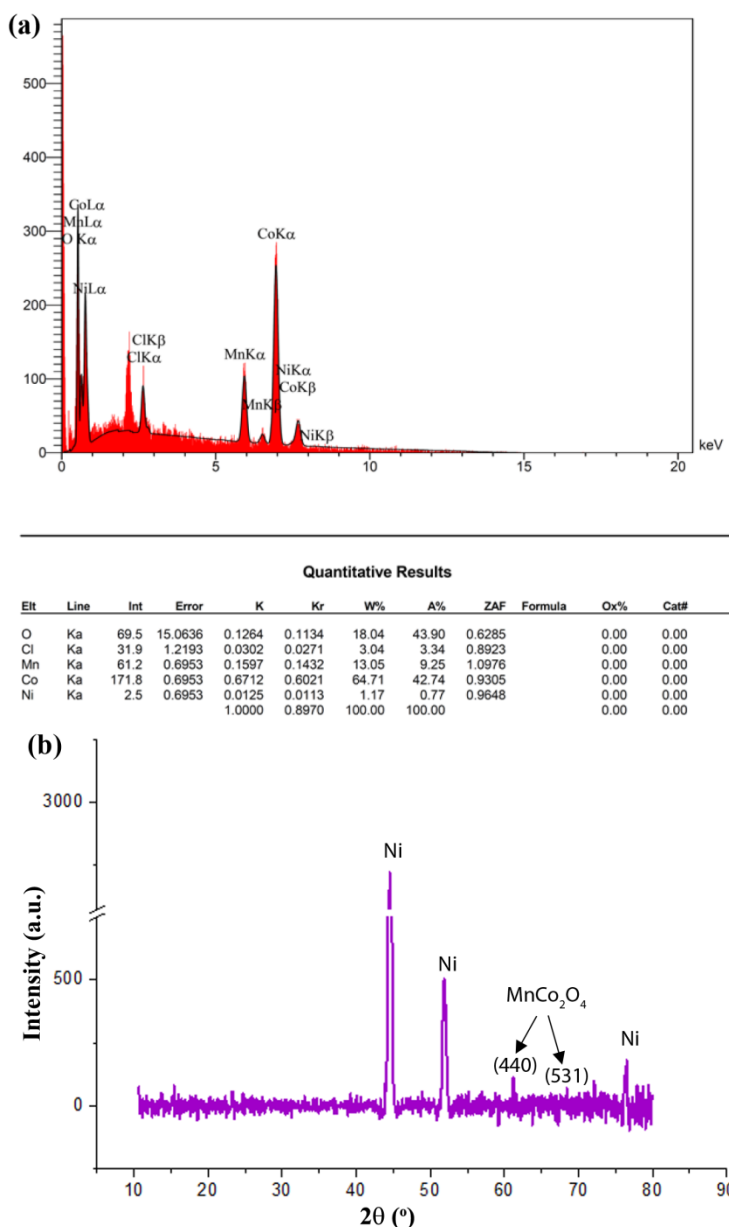
Figure 3: (a) EDX spectrum and (b) XRD pattern of MnCo₂O₄ nanosheets on the Ni foam.

3.3. Electrochemical evaluation

The super capacitive performance of the electro-synthesized electrode was investigated in this paper. Cyclic voltammetry (CV), galvanostatic charge/discharge (GCD), and electrochemical impedance spectroscopy (EIS) were used. They were measured in a three-electrode setup in 3 M KOH solution as the electrolyte.

3.3.1. Cyclic voltammetry

The CV curve was first recorded at 10 mV s^{-1} within the potential range of 0.0 to 0.5 V, as shown in Figure 4(a). The shape of the CV curve is different from that of EDLCs, which is similar to an ideal rectangular shape. The CV curves of the $MnCo_2O_4$ electrode show a pair of redox peaks corresponding to the interaction between spinel materials and electrolyte ions, reflecting the pseudocapacitive nature of the electrodes [35]. For the $MnCo_2O_4$ nanosheets, the electrochemical reactions could be described according to the following equation (Eq.1) [36]:

$$MnCo_2O_4 + OH^- + H_2O \longleftrightarrow MnOOH + 2CoOOH + e^- \quad (1)$$
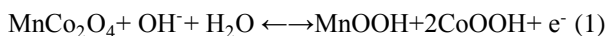
Based on the CV curve (Figure 4) of the $MnCo_2O_4$ electrode, a reversible electron-transfer process was detected, suggesting that the capacitance of $MnCo_2O_4$ arises from the redox mechanism. Furthermore, the low surface area obtained from the Ni foam substrate proves that the capacitance due to the current collector is negligible, and does not contribute to electrochemical reactions.

Figure 4b shows the CV curves of the $MnCo_2O_4$ electrode at different scan rates (5-100 mV s^{-1}). By increasing the scan rate, CV curves retain a nearly constant shape, representing the outstanding rate capability and fast kinetic of the faradaic reactions [37]. A slight shift in the anodic peaks was ascribed to the internal resistance of the electrode. At lower scan rates, the electrolyte ions can intercalate/de-intercalate into the accessible sites in the $MnCo_2O_4$ nanosheets, which results in high electrochemical reactions and high capacitance. But at higher scan rates, the effective interaction between electrode/electrolyte is considerably decreased. The faradaic reactions can take place only on the electrode material's outer surface, which leads to a decrease in the total capacitance [38].
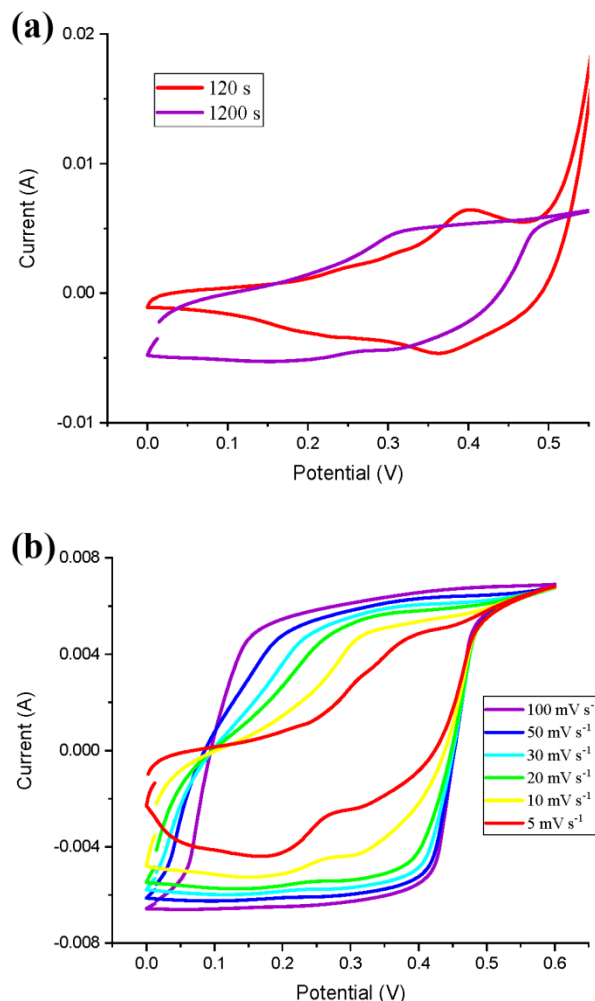
Figure 4: Voltammograms of $MnCo_2O_4$ nanosheets (a) at different deposition times at 10 mV s^{-1}, (b) at deposition time of 1200 s at different scan rates.

3.3.2. Galvanostatic charge/discharge

Figure 5a provides the GCD curve of the $MnCo_2O_4$ electrode with different deposition times in a potential window of 0.0-0.45 V (*vs.* Ag/AgCl) at the current density of 1.0 mA cm^{-2}. The symmetric shape of the GCD curves with the two well-defined voltage plateaus suggests the pseudocapacitive behavior of the electrode during the charge/discharge processes. It confirms the reversibility of the redox reactions [39], which agrees with CV results. The specific capacitance (mF cm^{-2}) was determined from the discharge cycles using equation 2 [40]:

$$C_s = \frac{I\Delta t}{S\Delta V} \quad (2)$$

where I is the charge/discharge current (A), Δt is the discharge time (s), S is the surface area of electrode material (cm²), and ΔV is the potential range during discharge (V). According to the discharge time, increasing deposition time remarkably affected the specific capacitance. The $MnCo_2O_4$ electrode with a deposition time of 1200 s delivered a high specific capacitance of 1198 mF cm⁻² at the current density of 1.0 mA cm⁻², while the $MnCo_2O_4$ electrode with the deposition time of 120 s delivered a specific capacitance of 577 mF cm⁻² at the same current density.

Figure 5b shows the GCD curves of the $MnCo_2O_4$ nanosheet electrode at different current densities, ranging from 1 to 20 mA cm⁻². The curves are symmetric, and the duration of charge and discharge curves are nearly equal, indicating a high columbic efficiency, fast redox reactions at the interface of electrode/electrolyte, and ideal capacitor behavior.

3.3.3. Electrochemical impedance spectroscopy (EIS)

The EIS analysis is a significant test that provides valuable information about the resistance behavior at the interface of electrode/electrolyte in many applications [41-51]. The Nyquist impedance plot (imaginary part (Z″) versus real part (Z′)) for the $MnCo_2O_4$ nanosheet electrode shows a small semicircle in a high-frequency region and a nearly straight line in the low-frequency region.

The intercept of the Nyquist plot at the x-axis reflects the equivalent series resistance (ESR) value. At the same time, the diameter of the semicircle represents the charge-transfer resistance (R_{ct}) value, and the straight line at the low-frequency region reflects the Warburg impedance. The ESR value of the $MnCo_2O_4$ nanosheet electrode achieved from extrapolating the Nyquist plot at the x-axis was 1.65 Ω (Figure 6a), which arose from the resistance of both electrolyte and electrode textile. The low ESR value of the electrode reveals fast electron transfer, reflecting the rich electrochemical reactions of the $MnCo_2O_4$ nanosheet.

According to the diameter of the semicircle (indicative of interfacial charge-transfer resistance), the R_{ct} of the $MnCo_2O_4$ nanosheet electrode was 2.5 Ω. The high electrical conductivity of $MnCo_2O_4$ resulted in the reduced R_{ct} and can be related to the fast charge transfer rate of the ions at $MnCo_2O_4$ nanosheets. Besides, the sharp line at the high-frequency region reflects the Warburg resistance (the more vertical line

for an electrode closer to an ideal capacitor), which arises from the frequency dependence of ion diffusion in the electrolyte [52, 53]. The $MnCo_2O_4$ nanosheets revealed a short ion diffusion pathway, as shown from the Warburg part on the Nyquist plot.

Furthermore, the $MnCo_2O_4$ electrode displays an almost vertical line in the low-frequency region, indicating reduced mass transfer resistance (Warburg), and further approving the fast redox reactions. Moreover, the $MnCo_2O_4$ nanosheet shows a lower internal resistance indicating its higher electrical conductivity [16].

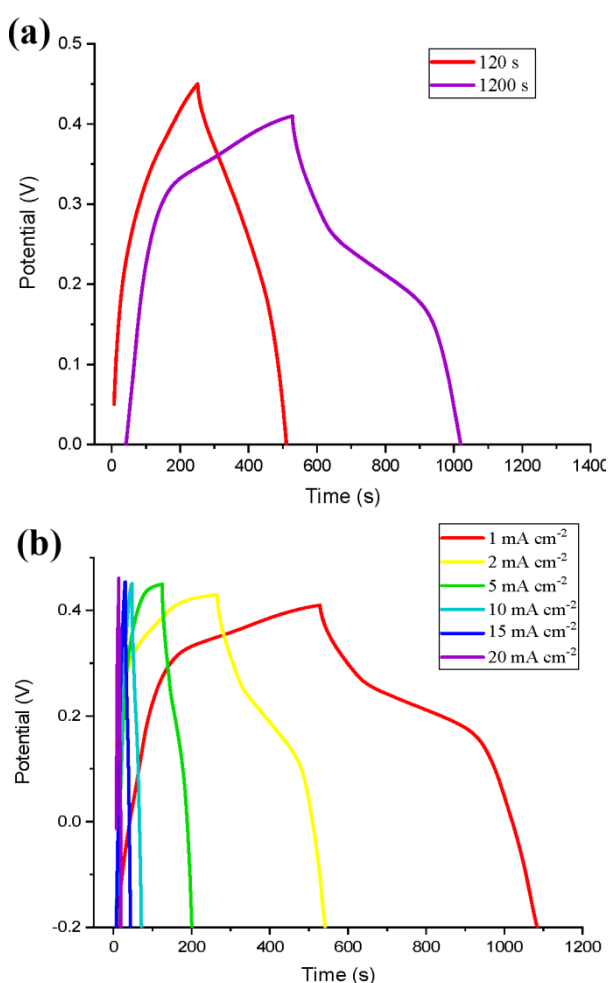**Figure 5:** GCD curves of MnCo₂O₄ nanosheets (a) at different deposition times at 1 mA cm⁻², (b) at deposition time of 1200 s at different current densities.
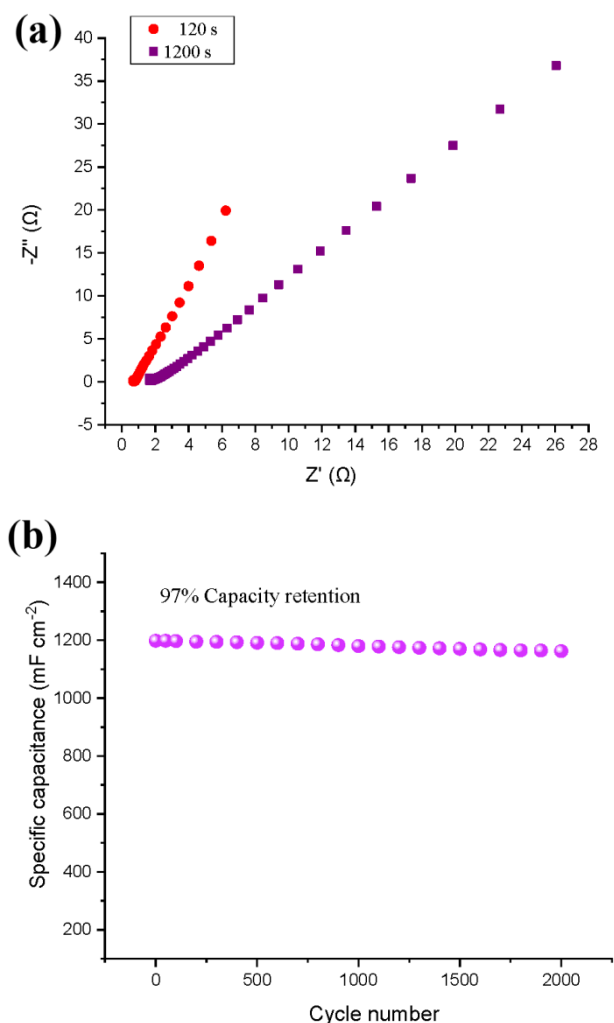
Figure 6: (A) EIS of $MnCo_2O_4$ nanosheets at different deposition times, and (B) capacity retention of $MnCo_2O_4$ nanosheets after 2000 CCV curve at 250 mV s^{-1}.

3.3.4. Continues cyclic voltammetry (CCV)

Long-term cycling stability is necessary for practical application of supercapacitors. It was examined for the $MnCo_2O_4$ nanosheet electrode. CCV test can be regarded as the best technique for monitoring and exploring the CVs and charge storage performance of supercapacitors during the time [54-56]. Successive CCV tests estimated the long-term cycling stability of the $MnCo_2O_4$ nanosheet electrode at the scan rate of 250 mV s^{-1} for 2000 cycles.

The specific capacitance as a function of time is demonstrated in Figure 6b. As shown, the specific capacitance of the $MnCo_2O_4$ nanosheet electrode remains nearly unchanged until 2000 cycles and

gradually decreases from 1198 mF cm^{-2} to 1162 mF cm^{-2} (3% decrease). This phenomenon suggests the excellent cycling stability of the $MnCo_2O_4$ electrode. These results reveal that the $MnCo_2O_4$ nanosheet electrode is highly stable during the time. The enhanced electrochemical performance of the $MnCo_2O_4$ nanosheet arrays was ascribed to its unique structure, which provides more electroactive sites for reactive species.

The superior performance of the $MnCo_2O_4$ electrode can be ascribed to the following features: (1) The $MnCo_2O_4$ was directly grown on a nickel foam substrate, which can gain direct mechanical and electrical contact with the underlying nickel foam. (2) The nanosheet feature of the $MnCo_2O_4$ electrode and superior contact area provide many electroactive sites for ions adsorption and electrochemical redox reactions. (3) The voids between the interconnected nanosheets act as ion-buffering reservoirs and ease the channeling of electrolyte ions and charge transfer [57, 58]. (4) The spinel nature of the $MnCo_2O_4$ nanosheets has high electrical conductivity and rich redox reaction, providing many superficial electroactive species for participation in Faradaic redox reactions. Therefore, lower contact resistance and superior super capacitive performance can be obtained [59]. (5) Binder-free design provides efficient electron paths for charge transport because of void spaces between neighboring sheets and ensures efficient electron transfer between active material and substrate. All of these aspects are beneficial for enhancing the super capacitive performances of the electrode materials.

4. Conclusions

In summary, a facile one-pot approach has been developed to deposit 3D interconnected $MnCo_2O_4$ nanosheet arrays through electrochemical deposition on Ni foam substrate as an efficient electrode material for supercapacitors. The $MnCo_2O_4$-loaded nickel foam can be directly used as a supercapacitor electrode without any binders and/or additives. The $MnCo_2O_4$ nanosheet electrode revealed superior performances, including a high specific capacitance of 1198 mF cm^{-2} at 1 mA cm^{-2} and long cycle life. The improved super capacitive performances are mainly ascribed to its unique nanosheet architecture, which provides many electroactive sites for electrolyte ions, allowing them easy access to the electrode surface. The results are

promising and indicate the possible application of MnCo$_2$O$_4$ nanosheets as electrode material for supercapacitors.

5. References

1. S. Zhang, N. Pan, Supercapacitors performance evaluation, *Adv. Energy Mater.,* 5(2015), 1401401.

2. L. Huang, D. Chen, Y. Ding, S. Feng, Wang Z.L., M. Liu, Nickel–cobalt hydroxide nanosheets coated on NiCo$_2$O$_4$ nanowires grown on carbon fiber paper for high-performance pseudocapacitors, *Nano Lett.*, 13(2013), 3135-3139.

3. P. Simon, Y. Gogotsi, B. Dunn, Where do batteries end and supercapacitors begin?, *Science,* 343(2014), 1210-1211.

4. X. Cao, B. Zheng, W. Shi, J. Yang, Z. Fan, Z. Luo, X. Rui, B. Chen, Q. Yan, H. Zhang, Reduced graphene oxide-wrapped MoO$_3$ composites prepared by using metal–organic frameworks as precursor for all-solid-state flexible supercapacitors, *Adv. Mater.*, 27(2015), 4695-4701.

5. L. F. Chen, Z. H. Huang, H. W. Liang, Q. F. Guan, S. H. Yu, Bacterial-cellulose-derived carbon nanofiber@ MnO$_2$ and nitrogen-doped carbon nanofiber electrode materials: An asymmetric supercapacitor with high energy and power density, *Adv. Mater.*, 25(2013), 4746-4752.

6. P. Simon, Y. Gogotsi, Materials for electrochemical capacitors. In Nanoscience and technology: a collection of reviews from Nature journals 2010 (pp. 320-329).

7. G. Wang, L. Zhang, J. Zhang, A review of electrode materials for electrochemical supercapacitors, *Chem. Soc. Rev.*, 41(2012), 797-828.

8. L. Abbasi, M. Arvand, Engineering hierarchical ultrathin CuCo$_2$O$_4$ nanosheets array on Ni foam by rapid electrodeposition method toward high-performance binder-free supercapacitors, *Appl. Surf. Sci.*, 445(2018), 272-280.

9. Z. Yu, L. Tetard, L. Zhai, J. Thomas, Supercapacitor electrode materials: nanostructures from 0 to 3 dimensions, *Energy Environ. Sci.*, 8(2015), 702-730.

10. H. Zhou, D. Li, M. Hibino, I. Honma, A self-ordered, crystalline-glass, mesoporous nanocomposite for use as a lithium-based storage device with both high power and high energy densities, *Angew. Chem. Int. Ed.*, 44(2005), 797-802.

11. D.N. Futaba, K. Hata, T. Yamada, T. Hiraoka, Y. Hayamizu, Kakudate Y. Kakudate, O. Tanaike, H. Hatori, M. Yumura, S. Iijima, Shape-engineerable and highly densely packed single-walled carbon nanotubes and their application as super-capacitor electrodes, *Nat. Mater.*, 5(2006), 987-994.

12. H. Heydari, S.E. Moosavifard, S. Elyasi, M. Shahraki, Nanoporous CuS nano-hollow spheres as advanced material for high-performance supercapacitors, *Appl. Surf. Sci.*, 394(2017), 425-430.

13. Z. Norouzi, S. A. Mozaffari, S. H. Mahmoudi Najafi, Three-dimensional unified electrode design using CuO embedded MnO$_2$ Nano-dandelions@Ni(OH)$_2$ nano-flakes as electrode material for high-performance supercapacitors, *J. Alloy. Compd.*, 938(2023), 168603.

14. L. Shen, L. Yu, H.B. Wu, X.Y. Yu, X. Zhang, X.W. Lou, Formation of nickel cobalt sulfide ball-in-ball hollow spheres with enhanced electrochemical pseudocapacitive properties, *Nat. Commun.,* 6(2015), 1-8.

15. L. Li, Y.Q. Zhang, X.Y. Liu, S.J. Shi, X.Y. Zhao, H. Zhang, X. Ge, G.F. Cai, C.D. Gu, X.L. Wang, J.P. Tu, One-dimension MnCo$_2$O$_4$ nanowire arrays for electrochemical energy storage, *Electrochim. Acta*, 116(2014) 467-474.

16. S. Jayasubramaniyan, S. Balasundari, P.A. Rayjada, R.A. Kumar, N. Satyanarayana, P. Muralidharan, Enhanced electrochemical performance of MnCo$_2$O$_4$ nanorods synthesized via microwave hydrothermal method for supercapacitor applications, *J. Mater. Sci. Mater. Electron.*, 29(2018) 21194-21204.

17. J.A. Mehrez, K.A. Owusu, Q. Chen, L. Li, K. Hamwi, W. Luo, L. Mai, Hierarchical MnCo$_2$O$_4$@NiMoO$_4$ as free-standing core-shell nanowire arrays with synergistic effect for enhanced supercapacitor performance, *Inorg. Chem. Front.*, 6(2019) 857-865.

18. L. Wu, J. Lang, P. Zhang, X. Zhang, R. Guo, X. Yan, Mesoporous Ni-doped MnCo$_2$O$_4$ hollow nanotubes as an anode material for sodium ion batteries with ultralong life and pseudocapacitive mechanism, *J. Mater. Chem. A*, 4(2016), 18392-18400.

19. G. Zhang, X.W. Lou, General solution growth of mesoporous NiCo$_2$O$_4$ nanosheets on various conductive substrates as high-performance electrodes for supercapacitors, *Adv. Mater.*, 25(2013), 976-979.

20. D. Cai, S. Xiao, D. Wang, B. Liu, L. Wang, Y. Liu, H. Li, Y. Wang, Q. Li, T. Wang, Morphology controlled synthesis of NiCo$_2$O$_4$ nanosheet array nanostructures on nickel foam and their application for

pseudocapacitors, *Electrochim. Acta*, 142(2014), 118-124.

21. A.K. Mondal, D. Su, S. Chen, A. Ung, H.S. Kim, G. Wang, Mesoporous $MnCo_2O_4$ with a flake-like structure as advanced electrode materials for lithium-ion batteries and supercapacitors, *Chem. A Eur. J.*, 21(2015), 1526-1532.

22. M. F. El-kady, Y. Shao, R. B. Kaner, Graphene for batteries, supercapacitors and beyond, *Nat. Rev. Mater.*, 1(2016), 1-14.

23. X. Xia, J. Tu, Y. Zhang, X. Wang, C. Gu, X. B. Zhao, H. J. Fan, High-quality metal oxide core/Shell nanowire arrays on conductive substrates for electrochemical energy storage, *acs nano*, 6(2012), 5531-5538.

24. R. P. Silva, S. Eugénio, T. M. Silva, M. J. Carmezim, Montemor M.F. Montemor, Fabrication of three-dimensional dendritic Ni-Co films by electrodeposition on stainless steel substrates, *J. Phys. Chem. C*, 116(2012), 22425-22431.

25. S-L. Chou, Y. Pan, J-Z. Wang, H-K. Liu, S-X. Dou, Small things make a big difference: binder effects on the performance of Li and Na batteries, *Phys. Chem. Chem. Phys.*, 16(2014), 20347-20359.

26. D. Liu, Q. Wang, L. Qiao, F. Li, D. Wang, Z. Yang, D. He, Preparation of nano-networks of MnO_2 shell/Ni current collector core for high-performance supercapacitor electrodes, *J. Mater. Chem.*, 22(2012), 483-487.

27. T. Fujita, P. Guan, K. McKenna, X. Lang, A. Hirata, L. Zhang, T. Tokunaga, S. Arai, Y. Yamamoto, N. Tanaka, Y. Ishikawa, Atomic origins of the high catalytic activity of nanoporous gold, *Nat. Mater.*, 11(2012), 775-780.

28. Y. Zhang, M. Ma, J. Yang, C. Sun, H. Su, W. Huang, X. Dong, Shape-controlled synthesis of $NiCo_2S_4$ and their charge storage characteristics in supercapacitors, *Nanoscale*, 6(2014), 9824-9830.

29. S. Sahoo, C.S. Rout, Facile electrochemical synthesis of porous manganese-cobalt-sulfide based ternary transition metal sulfide nanosheets architectures for high performance energy storage applications, *Electrochim. Acta*, 220(2016), 57-66.

30. H. Liu, Z. Guo, S. Wang, X. Xun, D. Chen, J. Lian, Reduced core-shell structured $MnCo_2O_4@MnO_2$ nanosheet arrays with oxygen vacancies grown on Ni foam for enhanced-performance supercapacitors" *J. Alloy. Compd.*, 846(2020), 156504.

31. M. He, L. Cao, W. Li, X. Chang, X. Zheng, Z. Ren, NiO nanoflakes decorated needle-like $MnCo_2O_4$ hierarchical structure on nickle foam as an additive-free and high-performance supercapacitor electrode, *J. Mater. Sci.*, 56(2021), 8613-8626.

32. J. Xu, Y. Sun, M. Lu, L. Wang, J. Zhang, E. Tao, J. Qian, X. Liu, Fabrication of the porous $MnCo_2O_4$ nanorod arrays on Ni foam as an advanced electrode for asymmetric supercapacitors", *Acta Mater.*, 152(2018), 162-174.

33. S. Tan, Y. Ji, F. Chen, and W. Ouyang, Three-dimensional sea urchin-like $MnCo_2O_4$ nanoarchitectures on Ni foam towards high-performance asymmetric supercapacitors, *Front. Mater. Sci.*, 15(2021), 611-620.

34. Z. Chaozheng, M. Yongzhi, B. Qingkai, Z. Yanting, W. Kai, Two-step synthesis and characterization of $mnco_2o_4$ composite and its electrochemical performance, *Int. J. Electrochem. Sci.*, 13(2018), 10207-10216.

35. C. Yuan, L. Yang, L. Hou, L. Shen, X. Zhang, X.W. Lou, Growth of ultrathin mesoporous Co_3O_4 nanosheet arrays on Ni foam for high-performance electrochemical capacitors, *Energ. Environ. Sci.*, 5(2012), 7883-7887.

36. A. Pramanik, S. Maiti, M. Sreemany, S. Mahanty, Carbon doped $MnCo_2S_4$ microcubes grown on ni foam as high energy density faradaic electrode, *Electrochim. Acta*, 213(2016) 672-679.

37. S.E. Moosavifard, S. Fani, M. Rahmanian, Hierarchical $CuCo_2S_4$ hollow nanoneedle arrays as novel binder-free electrodes for high-performance asymmetric supercapacitors, *Chem. Commun.*, 4(2016), 2-5.

38. A.A. Ensafi, S.E. Moosavifard, B. Rezaei, S.K. Kaverlavani, Engineering onion-like nanoporous $CuCo_2O_4$ hollow spheres derived from bimetal-organic frameworks for high-performance asymmetric supercapacitors, *J. Mater. Chem. A.*, 6(2018), 10497-10506.

39. H. Jiang, T. Zhao, C. Li, J. Ma, Hierarchical self-assembly of ultrathin nickel hydroxide nanoflakes for high-performance supercapacitors, *J. Mater. Chem.*, 21(2011), 3818-3823.

40. M. Amiri, S.E. Moosavifard, S.SH. Davarani, S.K. Kaverlavani, M. Shamsipur, MnCoP hollow nanocubes as novel electrode material for asymmetric supercapacitors, *Chem. Eng. J.*, 420(2021), 129910.

41. M. Khalili, M. Abedi, H.S. Amoli, S.A. Mozaffari, Comparison of chitosan and chitosan nanoparticles on the performance and charge recombination of water-based gel electrolyte in dye sensitized solar cells, *Carbohyd. Polym.*, 175(2017), 1-6.

42. E. Kouhestanian, S.A. Mozaffari, M. Ranjbar, H.S. Amoli, Enhancing the electron transfer process of TiO_2-based DSSC using DC magnetron sputtered ZnO as an efficient alternative for blocking layer, *Org. Electron.*, 86(2020), 105915.

43. M. Seifpanah Sowmehesaraee, M. Ranjbar, M. Abedi, S.A. Mozaffari, Fabrication of lead iodide perovskite solar cells by incorporating zirconium, indium and zinc metal-organic frameworks, *Sol. Energy*, 214(2021), 138-148.

44. M. Emadoddin, S.A. Mozaffari, F. Ebrahimi, An antifouling impedimetric sensor based on zinc oxide embedded polyvinyl alcohol nanoplatelets for wide range dopamine determination in the presence of high concentration ascorbic acid, *J. Pharm. Biomed. Anal.*, 205(2021), 114278.

45. M. Hosseinzadeh, S. A. Mozaffari, F. Ebrahimi, Porous 3D-graphene functionalized with MnO_2 nanospheres and NiO nanoparticles as highly efficient electrodes for asymmetric capacitive deionization: Evaluation by impedance-derived capacitance spectroscopy, *Electrochim. Acta*, 427(2022) 140844.

46. S. Khazaei, S.A. Mozaffari, F. Ebrahimi, Polyvinyl alcohol as a crucial omissible polymer to fabricate an impedimetric glucose biosensor based on hierarchical 3D-NPZnO/chitosan, *Carbohyd. Polym.* 266 (2021), 118105.

47. R. Shabani, S.A. Mozaffari, S.W. Husain, M.S. Tehrani, Selective nanosensing of copper (II) ion using l-lysine functionalized gold cysteamine self-assembled monolayer, *Iran. J. Sci. Technol. Trans A Sci.*, 33(2009), 335-347.

48. S.A. Mozaffari, S.H. Mahmoudi Najafi, Z. Norouzi, Hierarchical $NiO@Ni(OH)_2$ nanoarrays as high-performance supercapacitor electrode material, *Electrochim. Acta*, 368(2021) 137633.

49. A. Shahriari, H. Aghajani, M.Gh. Hosseini, A study of oxidation behavior of AZ91D alloy with YSZ coating using *EIS, Prog. Color Colorants Coat.*, 10(2017), 1-12.

50. M.Gh. Hosseini, K. Aboutalebi, Electrochemical evaluation of corrosion protection performance of epoxy/polyaniline-imidazole modified ZnO nanocomposite coating on mild steel, *Prog. Color Colorants Coat.*, 10(2017), 181-192.

51. E. Kouhestanian, M. Ranjbar, S.A. Mozaffari, H. Salaramoli, Investigating the effects of thickness on the performance of ZnO-Based DSSC, *Prog. Color Colorants Coat.*, 14(2021), 101-112.

52. S.A. Hashemi, S.M. Mousavi, H.R. Naderi, S. Bahrani, M. Arjmand, A. Hagfeldt, W.H. Chiang, S. Ramakrishna, Reinforced polypyrrole with 2D graphene flakes decorated with interconnected nickel-tungsten metal oxide complex toward superiorly stable supercapacitor, *Chem. Eng. J.*, 418(2021), 129396.

53. Z. Norouzi, S. H. Mahmoudi Najafi, S. A. Mozaffari, Silver-loaded carbon sphere-in-rod 3D nano-architectures as electrode material for supercapacitors, *Diam. Relat. Mater.,* 27(2021), 108734.

54. H.R. Naderi, A. Sobhani-nasab, M. Rahimi-nasrabadi, M.R. Ganjali, Decoration of Nitrogen-doped Reduced Graphene Oxide with Cobalt Tungstate Nanoparticles for Use in High-Performance Supercapacitors, *Appl. Surf. Sci.*, 423(2017), 1025-1034.

55. M. Rahimi-nasrabadi, H. Reza, N. Meisam, S. Karimi, Cobalt carbonate and cobalt oxide nanoparticles synthesis, characterization and supercapacitive evaluation, *J. Mater. Sci. Mater. Electron.*, 28(2017), 1877-1888.

56. H.R. Naderi, H.R. Mortaheb, A. Zolfaghari, Supercapacitive properties of nanostructured MnO_2/exfoliated graphite synthesized by ultrasonic vibration, *J. Electroanal. Chem.*, 719(2014), 98-105.

57. J. Pu, Y. Tong, S. Wang, E. Sheng, Z. Wang, Nickel-cobalt hydroxide nanosheets arrays on Ni foam for pseudocapacitor applications, *J. Power Sources*, 250(2014), 250-256.

58. S. W. Chou, J. Y. Lin, Cathodic Deposition of Flaky Nickel Sulfide Nanostructure as an Electroactive Material for High-Performance Supercapacitors, *J. Electrochem. Soc.*, 160(2013) D178-D182.

59. W. Hu, R. Chen, W. Xie, L. Zou, N. Qin, D. Bao, $CoNi_2S_4$ nanosheet arrays supported on Ni foams with ultrahigh capacitance for aqueous asymmetric supercapacitor applications, *ACS Appl. Mater. Inter.,* 6(2014), 19318-19326.

How to cite this article:
Z. Norouzi, S. H. Mahmoudi Najafi, S. A. Mozaffari, Facile One-pot Synthesis of Binder-free MnCo₂O₄ Nanosheets as Efficient Supercapacitor Electrode Material. Prog. Color Colorants Coat., 16 (2023), 271-281.

Color Changes, AFM and SEM Study of PVC/triorganotin (IV) - Cephalexin Complexes Samples Via UV Radiation

R. R. Arraq[1], A. G. Hadi[1], D. S. Ahmed[2], M. H. Al-Mashhadani[3], H. Hashim[4], A. A. Ahmed[5], A. Husain[5], S. J. Baqir[6], A. H. Jawad[7], E. Yousif[3*]

[1.] Department of Chemistry, College of Science, Babylon University, P.O. Box: 51002, Babil, Iraq

[2.] Department of Medical Instrumentation Engineering, Al-Mansour University College, P.O. Box: 62021, Baghdad, Iraq

[3.] Department of Chemistry, College of Science, Al-Nahrain University, P.O. Box: 62021, Baghdad, Iraq

[4.] Department of Physics, College of Science, Al-Nahrain University, P.O. Box: 62021, Baghdad, Iraq

[5.] Polymer Research Unit, College of Science, Al-Mustansiriyah University, P.O. Box: 62021, Baghdad, Iraq

[6.] Medical Laboratories Techniques Department, Al-Mustaqbal University College, P.O. Box: 51002, Babil, Iraq

[7.] Faculty of Applied Sciences, Universiti Teknologi MARA, P.O. Box: 40450, Shah Alam, Selangor, Malaysia

ARTICLE INFO

ABSTRACT

*T*hree organotin complexes were successfully produced in the presence of sodium hydroxide by the condensation reaction of cephalexin (ligand) and tri-organotin (IV) complexes. The complexes formed were given trigonal bipyramidal geometries based on spectrum measurements. These compounds were applied as additives (0.5 percent by weight) to reduce the photodegradation of polyvinyl chloride films (40 µm thickness) when exposed to ultraviolet light at a normal temperature (max = 313 at an intensity of light = 7.75×10^{-7} ein dm^{-3} S^{-1}). The weight changes of films before and after irradiation can be applied to investigate the effectiveness of organotin (IV) complexes as photo stabilizers. After irradiation, the morphology of poly(vinyl chloride) studied by the microscope, atomic force microscopy, and scanning electron microscope was shown to be less damaged in the films containing additives. These additives are effective UV absorbers, hydrogen chloride scavengers, and peroxide quenchers. Prog. Color Colorants Coat. 16 (2023), 283-294© Institute for Color Science and Technology.

1. Introduction

Organometallic compounds are substances that have directed greater or lesser polar connections between metallic and carbon atoms [1]. Thousands, if not millions, of compounds, have been synthesized during the last five decades, with organotin materials receiving the greatest attention, Organotin compounds are among the most commonly employed organometallic compounds [2]. These compounds have a tin atom and an anion that is often hydroxide, oxide, fluoride, chloride, or thiolate [3]. Due to their diverse structural makeup and numerous potential uses in a number of industries, organotin complexes are of tremendous interest [4, 5]. The research of various coordination modes, such as chelate, monodentate, or more subtle bridging, which can produce oligomeric or polymeric structures, is made possible by the coordination of carboxyl groups to organotin residues. Organotin (IV) carboxylates have been used in the stability of polyvinyl chloride (PVC), polyurethane synthesis, antifouling coatings, and silicone curing [6-8]. Organotin complexes are used as polyvinyl chloride stabilizers in the common of their applications due to their high reactivity.

When exposed to ultraviolet light, PVC photo oxidizes, with the autocatalytic dehydrochlorination process causing the majority of the damage [9-11]. Polymeric stretch, cross-links, and chain scissions develop when hydrogen chloride is removed from PVC, as a result, discoloration, fractures, losses in total molecular weight, transparency loss, and mechanical property changes occur [12, 13]. To improve polymer resistance to free radical scavengers, UV absorbers, hydroperoxide decomposes and exactions energy varied quantities are required to utilize effect additives [14, 15]. To successfully absorb ultraviolet light and create excited state molecules that are stabilized by resonance, a broad range of additives has been explored for their protective properties on polyvinylchloride films [16, 17]. Organotin (IV) carboxylates are the most recently developed and widely used PVC additives that are exceptionally stable and excellent HCl scavengers [18]. Cephalexin is a white solid containing aromatic rings and heteroatoms that are stable and non-toxic, when mixed with PVC; it is regarded as an ultraviolet absorbent with no color change or environmental difficulties [19]. They also function as antiviral medications, inflammatory agents, and antibacterial substances [20, 21]. Organotin compound efficiency was revealed as dependent on the kind and amount of substituents added to the tin. In this study, we describe the design, and use of new tin-cephalexin complexes as PVC additives to minimize photooxidation and photodegradation. These complexes are expected to be more efficient PVC photo stabilizers than those previously reported because they contain alkyl and aryl groups in addition to heteroatoms like nitrogen, oxygen, and sulfur.

2. Experimental

2.1. General

Petkim Petrokimya had an abundance of PVC (MV= about 165,000, K-value = 67, degree of polymerization = 800). (Istanbul, Turkey). The KBr disc method was used to record Fourier transform infrared spectroscopy on the Shimadzu FTIR spectrometer 8400 (Tokyo, Japan) in the spectral region of 4000 - 400 cm^{-1}. With the use of a Meiji Techno microscope (Tokyo, Japan), the PVC's surface morphology was examined, and Veeco equipment was used to log the atomic force microscope pictures (Plainview, NY, USA).

2.2. Synthesis of complexes 1–3

Tri-organotin(IV) complexes **1-3** (Figure 1) were made by reacting cephalexin with chloride triorganotin in MeOH under reflux for five hours, as was previously described [22]. Hence the molar ratios (metal: ligand) utilized to synthesize the complexes are 1:1, thus an suitable quantity of Ph$_3$SnCl (1.9273 g, 5.0, mmol), Bu$_3$SnCl (1.6275 g, 5.0 mmol), and Me$_3$SnCl (0.9964 g, 5.0 mmol) were dissolved in 20 mL of methanol and then added to a stirred solution of cephalexin (1.7369 g, 5.0 mmol) that dissolved in 30 mL of methanol with an equivalent amount of sodium hydroxide, After stirring for 10 minutes at room temperature, the mixture had been refluxed for 5 hours. The resultant solution was filtered, washed, dried, and recrystallized from methanol to produce pure target products (Scheme 1). Many spectroscopic and analytical findings supported the stated structures of synthesized compounds **1-3** and were compatible with them.
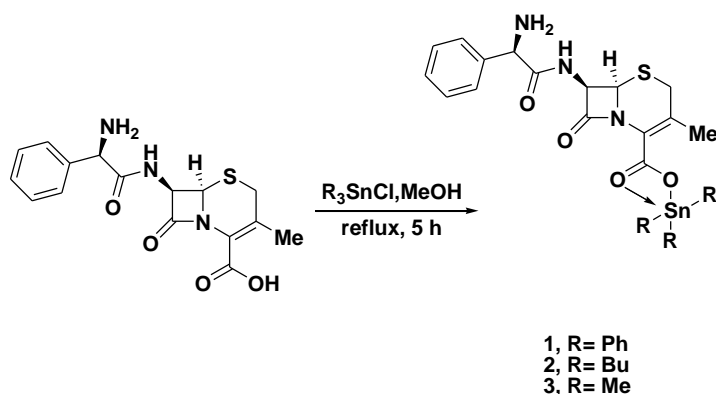

1, R= Ph
2, R= Bu
3, R= Me

Figure 1: Synthetic route of tin–cephalexin complexes **1–3**.

2.3. Preparation of PVC films

PVC (4 g) and tin complexes **1-3** (20 mg) were combined with 80 mL of THF and stirred for two hours. The final homogenous mixture was put into a glass plate with 15 holes that were approximately 40 micrometers thick. The plate was dried at room temperature overnight. To confirm that there were no remaining residues of THF, the generated films were dried in a vacuum oven at 50 °C for 6 hours.

2.4. IR spectroscopy of PVC

As a result of PVC photodegradation, tiny polymeric fragments with carbonyl (C=O) and alkene (C=C) moieties are produced. Dehydrochlorination, or hydrochloride (HCl) removal from the PVC chains, is the primary cause of this process [23]. PVC films were exposed to radiation at various exposure durations, and their FTIR spectra were captured. Both the C=O (1714 cm^{-1}) and C=C (1618 cm^{-1}) groups' absorption bands' intensities were measured and contrasted with a reference peak of C–H bonds; at 1332 cm^{-1}. Equation 1 was used to determine the functional group index (Is) for IC=O and IC=C groups from the absorbance of the functional group (As; AC=O or AC=C) and the reference peak (Ar; AC-H).

$$I_s = \frac{A_s}{A_r} \tag{1}$$

2.5. Polymeric films weight loss

The PVC polymeric films were weighed before (W_0) and after (W_t) irradiation at different times (t). The PVC weight loss (%) as a result of irradiation was calculated using Equation (2).

$$\text{Weight loss \%} = \frac{W_0 - W_t}{W_0} \times 100 \tag{2}$$

3. Results and Discussion

3.1. Polyvinyl chloride weight loss

While exposed to ultraviolet and/or high temperatures for longer, polyvinyl chloride (PVC) photodegrades. As a result of the release of hydrogen chloride (HCl) and the generation of molecular chains with double bonds, differences in the physical and mechanical properties of the polymer occur. When PVC is exposed to UV radiation (max = 313 at an intensity of light = 7.75×10^{-7} ein dm^{-3} S^{-1}) at ambient temperature, bonding breaks and unsaturated fragments with low molecular weights generate [24]. With time, Poly (vinyl chloride) discolors crosslinks and scissions. PVC weight loss becomes more visible as photodegradation progresses. The obtained and reported findings are depicted in Figure 2. The weight loss percentage is substantially reduced when additives were used in comparison to the blank PVC. After 300 hours of irradiation, the weight loss percentage of blank PVC is about 0.9 while for blended PVC films they are less than 0.3 in all cases. In comparison these results to previous studies [7] when the weight loss approach was used to investigate the efficiency of organotin(IV) complexes as photostabilizers of PVC after irradiation by UV light using Sulfamethoxazole as a ligand. It found that using triorganotin (IV)/cephalexin complexes demonstrated excellent results to reduce the photo-degradtion of PVC films after irradiation.
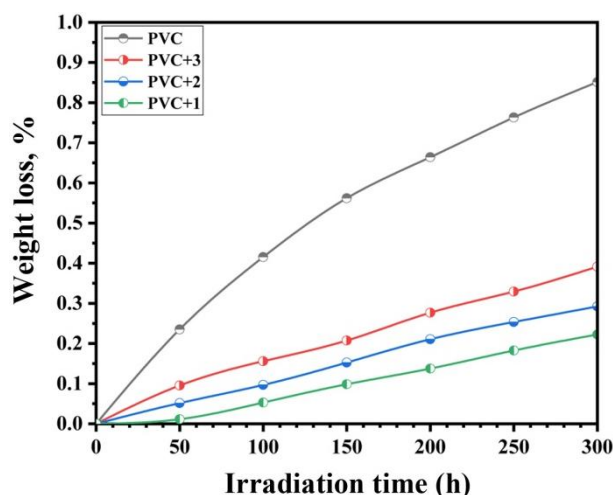
Figure 2: Shows how the UV exposure time affects the amount of weight loss in PVC films.

3.2. Fourier transforms infrared spectroscopy of PVC

The physical and chemical characteristics of polymers are impacted by ultraviolet light. Small fragments including hydroxyl, carbonyl, and polyene molecules are created during the photo-oxidation of polyvinylchloride. It is possible to measure and compare the intensity of peaks in the PVC films' fourier transform infrared spectra that are linked to the OH (3400 cm^{-1}), C=O (1730 cm^{-1}), and C=C (1620 cm^{-1}) groups with the intensity of a reference peak (1332 cm^{-1}) associated with the C-H bonds inside the polymer chains. This kind of comparison offers crucial knowledge regarding the pace at which PVC photodegrades [25].

Figures 3 and 4 illustrate the variations in the infrared wavelengths of PVC (pure) film and PVC+Me$_3$SnL film (mixed) after irradiation. The indices for the carbonyl (IC=O) and polyene (IC=C) groups were determined and displayed vs. irradiation time for each PVC film were shown in Figures 5 and 6. These values were substantially lower for the polymer films having organotin (IV) complexes **1-3** than for the blank film.
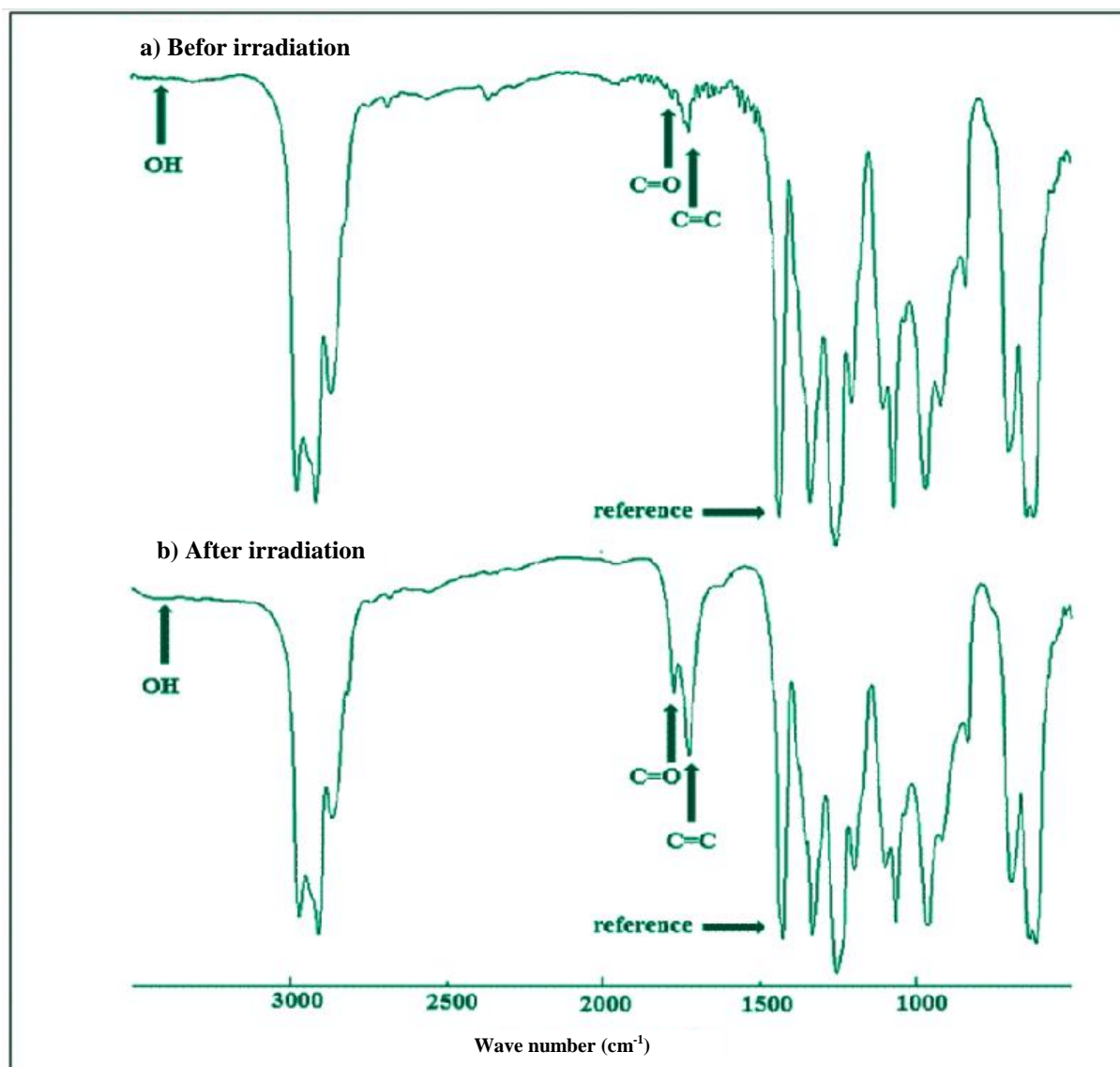
Figure 3: FT-IR spectra of blank PVC films.
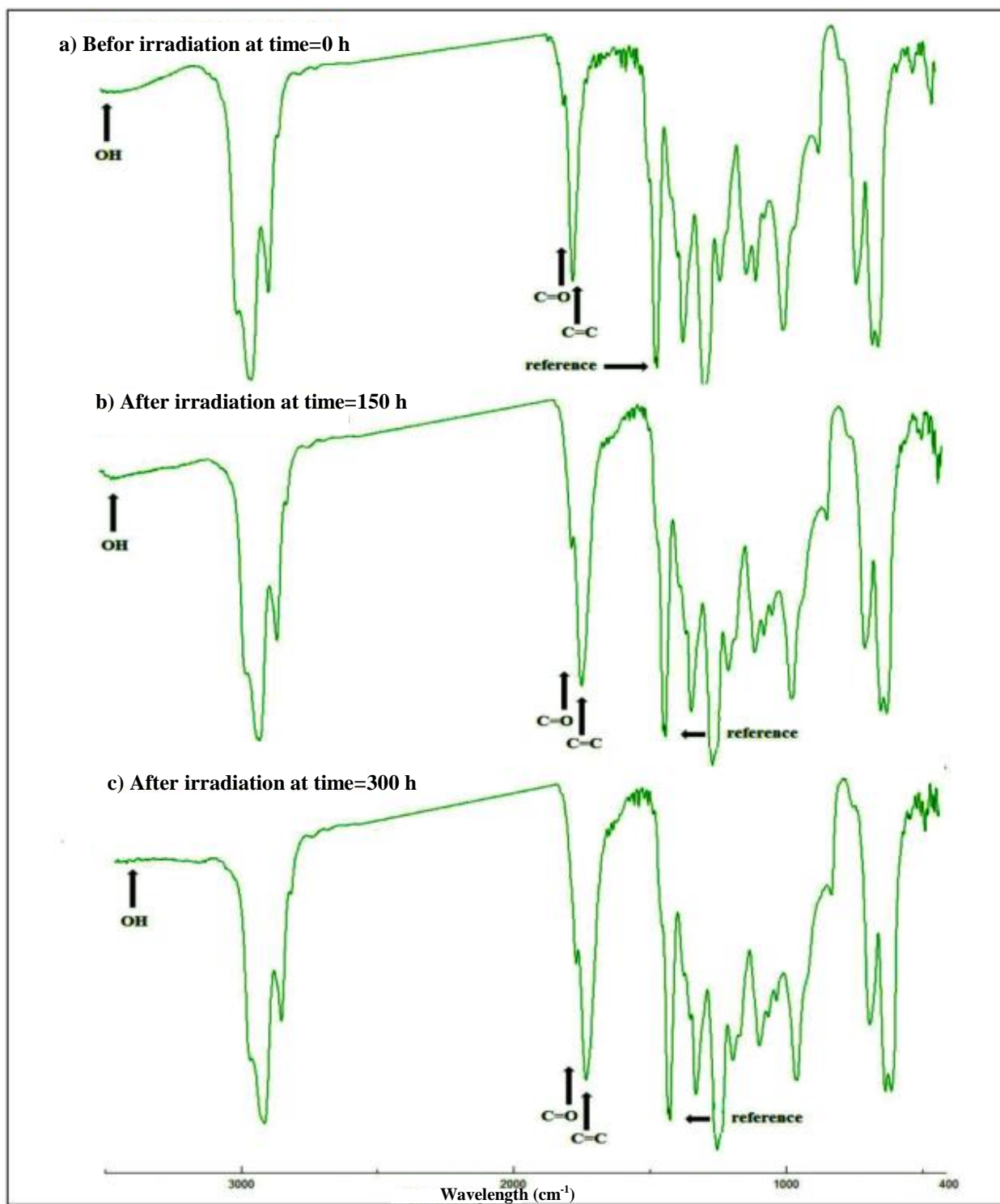
Figure 4: FT-IR spectra of doped PVC film containing Me₃SnL complex.
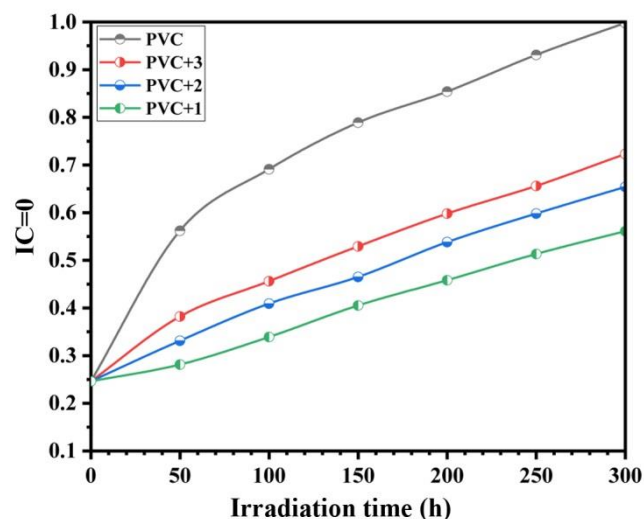
Figure 5: Irradiation's impact on the PVC films and growing of carbonyl group.
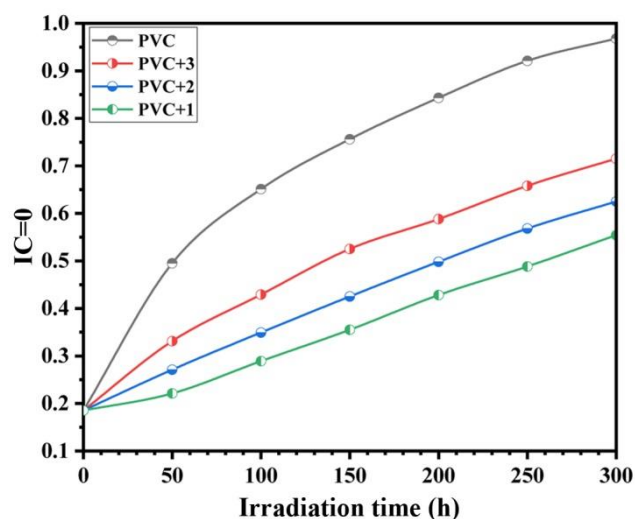
Figure 6: Irradiation's impact on the PVC films and growing of alkene group.

3.3. Surface morphology

3.3.1. Microscopic analysis

Morphological microscopy offers information on the roughness and irregularity of the surface of a polymeric film, as well as defects within the surface of a material [26, 27]. It identifies faults, fractures, damages, breakdowns, scission, and other modifications inside the polymer surface after 300 hours of exposure to UV radiation. Optical microscope images of the polyvinylchloride before irradiation revealed very few dark areas and a smooth surface with. While the polymer surface after irradiation had some surface damage, such as holes, and dark spots, as well as color changes due to photo-degradation. However, surface defects in organotin (IV) complexes **1-3** containing

PVC films were less visible as compared to those on the surface of the blank PVC film. Figure 7 depicts the fact that such compounds can slow down the photodegradation process and hence enhance the photostability of irradiated PVC films. The presence of bubbles, especially in the blank sample, is observed, which is probably related to the release of the solvent in the preparation of the sample and before irradiation. These bubbles can be seen in other images. Therefore, it seems that they cannot be attributed to dehydrochlorination.

3.3.2. Atomic force microscopy

According to the atomic force microscope with two- and three-dimensional images, the polymer (PVC) after

300 hours of irradiation has a rough surface with white spots and fractures. Although the polymer containing organotin (IV) complexes has smooth surfaces with fewer cracks as shown in Figure 8. The roughness factor (Rq) may be used to evaluate the roughness of the PVC surface, which measures the degree of photo-degradation produced by volatile reduction in response to irradiation. When Rq is large, dehydrochlorination and bond breakage results in a rough surface. Dehydrochlorination is usually carried out at high temperatures [28]. Interestingly, the roughness value of blank PVC is 1.08 before irradiation while it is 216.95 after 300 hours of irradiation. However, using the additives showed much lower roughness values especially for the Ph_3SnL complex (Rq = 26.18) as illuminated in Table 1. The synthesized three complexes demonstrated significant stability of PVC hence the Rq was much reduced in comparison to the blank PVC. However Ph_3SnL complex showed the best results, which is expected due to the presence of three phenyl groups that absorb UV light and prevent the photo-degradation of PVC chains.

3.3.3. Scanning electron microscope

The non-irradiated PVC films' SEM pictures revealed a smooth, clean surface with distinct grain boundaries and good particle homogeneity. Figure 9 shows that the PVC surface was damaged after 300 hours of irradiation. The damage was more obvious on the blank PVC than it was on the PVC with organotin additions. Additionally, the fissures were deeper and longer than they were in the non-radiated material. Such fractures may develop as a result of HCl and other volatile degradation chemicals' chain crosslinking and evaluation [29]. The PVC film with Ph_3SnLcomplex was clearly the one with the least surface damage.

Table 1: PVC roughness factor (Rq) following irradiation.

PVC Film	Rq
Blank PVC before irradiation	1.08
PVC	216.95
PVC+Ph₃SnL	26.18
PVC+Bu₃SnL	63.40
PVC+Me₃SnL	76.18
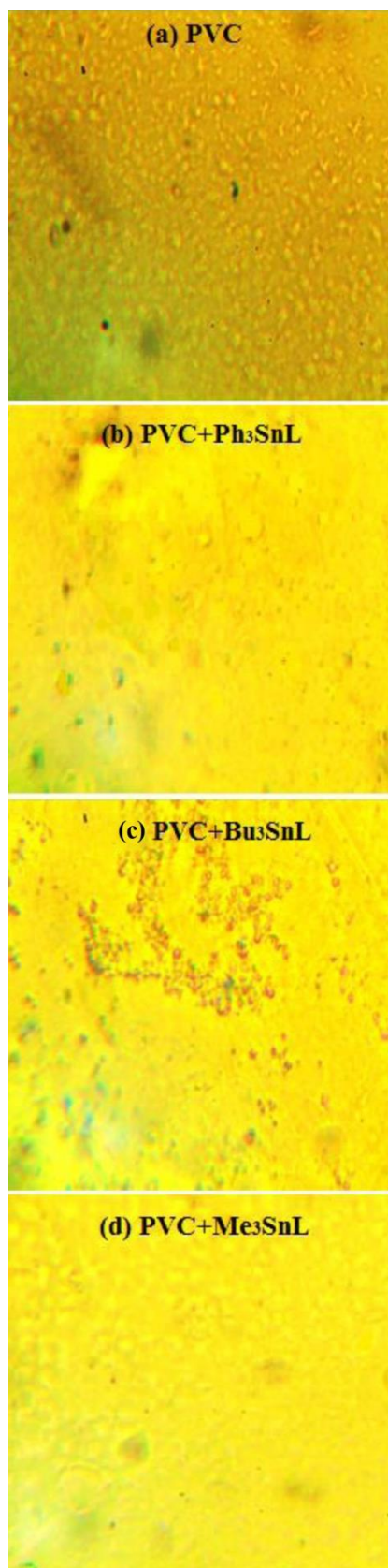
Figure 7: Microscope images of PVC and (PVC+Complexes) films after 300 h irradiation.

PVC

PVC+Ph₃SnL

PVC+Bu₃SnL

PVC+Me₃SnL
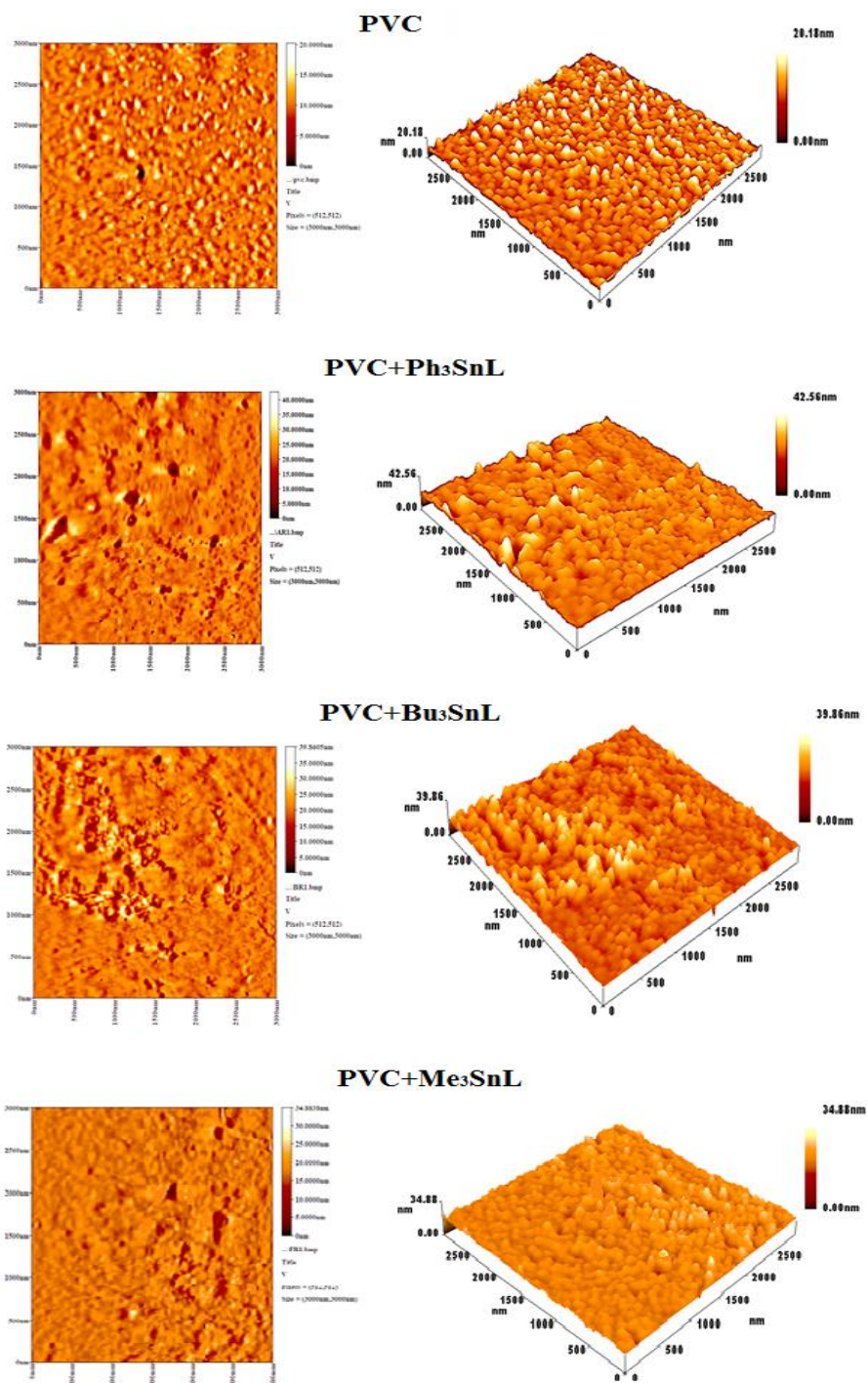
Figure 8: Atomic force microscopy images exhibit the effect of irradiation on PVC (pure) and (PVC + complexes).
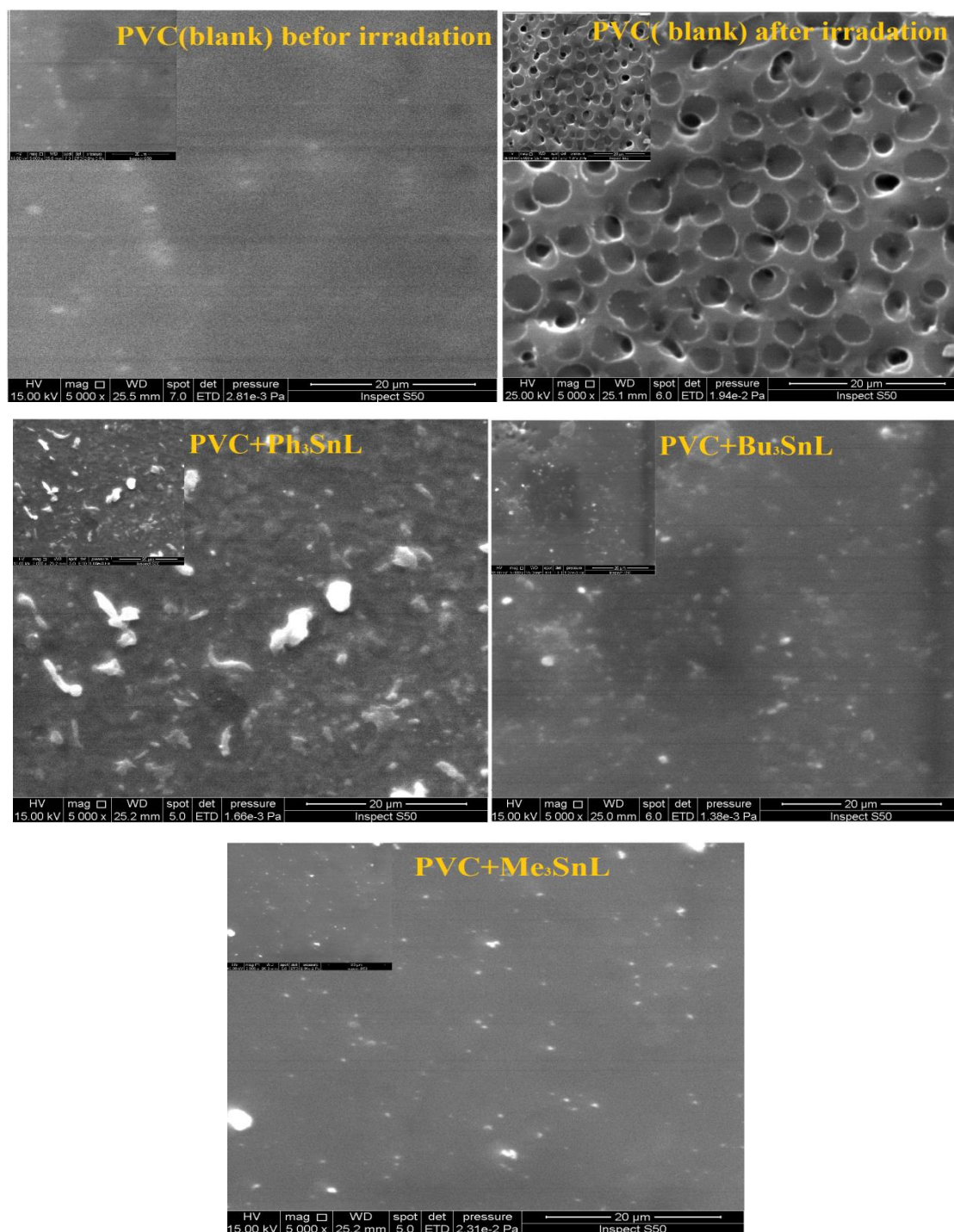
Figure 9: SEM images of PVC films.

3.4. Mechanisms of photo stabilization of PVC by triorganotin (IV)-cephalexin complexes

Compounds **1-3** decreased the amount of defect produced by photoirradiation to PVC and are consequently classified as PVC photo-stabilizers. The complex Ph₃SnL is the best because it includes three phenyl groups in addition to the aryl rings inside the cephalexin structure. Several approaches have been developed to characterize the activity of triorganotin (IV) complexes as photo stabilizers against PVC film photodegradation. PVC is dehydrochlorination after being exposed to UV light, because the tin atom is a Lewis acid, it can scavenge the hydrogen chloride that has been created, this action would decrease the
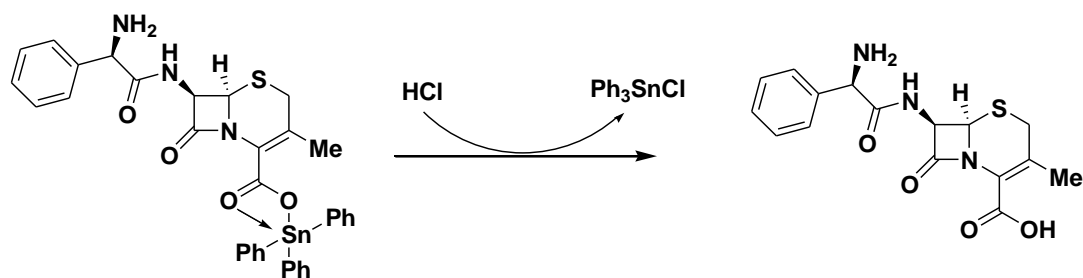
Scheme 1: Ph₃SnLcomplex as hydrogen chloride scavengers.
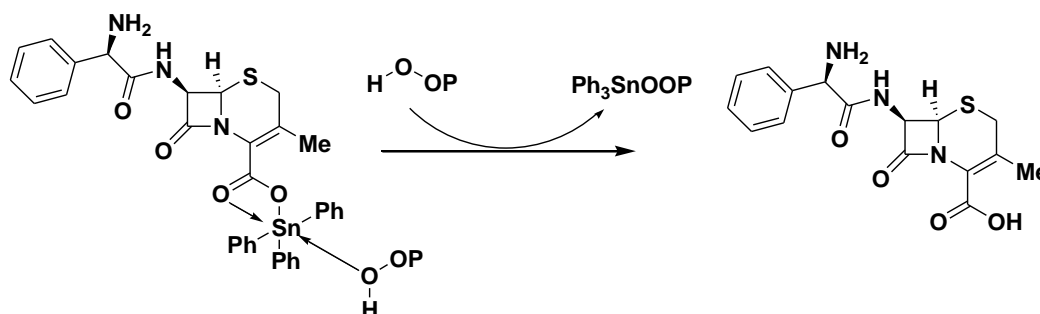
Scheme 2: Ph₃SnLcomplex as peroxide decomposers.

harmful effects of HCl on the polymeric chains Scheme 1. Photo-oxidation of PVC forms carbon radicals, that react with oxygen to form peroxide radicals [30]. As a result, complexes are expected to degrade peroxides (such as hydroperoxides) and inhibit PVC photodegradation (Scheme 2).

4. Conclusion

This research explains the production of appropriate quantities of new tin complexes containing cephalexin for photo stabilizers to limit the photodegradation of PVC films. Analytic and spectral techniques have been used to determine the structures of the tin (IV)-cephalexin complexes. Irradiation of PVC thin films causes changes throughout the infrared spectra because of the formation of tiny fragments carrying functional groups, material weight loss, and photodegradation-induced surface defects in the PVC. Such variations

were less distinct in the presence of tin complexes than in the blank PVC film. This additive decreased photodegradation and decreased the loss of weight of PVC film. The tri methyl tin complex also decreased the roughness factor of the irradiated materials by 2.18 the additions worked as UV absorption, chlorine scavengers, and hydroperoxide decomposers. To sum up, following irradiation, it was found that the poly(vinyl chloride) morphology was less harmed in the films containing additives. This was demonstrated by the microscope, atomic force microscopy, and scanning electron microscope. The UV absorbers, hydrogen chloride scavengers, and peroxide quenchers in these additives are all highly effective.

5. References

1. J. OuYang, J. Crassous, Chiral multifunctional molecules based on organometallic helicenes: recent advances, *Coord. Chem. Rev.*, 376(2018), 533-547.

2. U. Sair, A. Thakur, 119Sn NMR spectral data of organotin (IV) complexes–A review, *Mater. Today: Proc.*, 50(2021), 1862-1866.

3. L. Pellerito, L. Nagy, Organotin (IV)[n+] complexes formed with biologically active ligands: equilibrium and structural studies, and some biological aspects, *Coord. Chem. Rev.*, 224(2002), 111-150.

4. X. Ye, H. Pi, S. Guo, A novel route for preparation of PVC sheets with high UV irradiation resistance, *J. Appl. Polym. Sci.*, 117(2010), 2899-2906.

5. S. Hussain, S. Ali, S. Shahzadi, C. Rizzol, Polymeric three-dimensional crystal structure of a tributyltin (IV) derivative with acetylene dicarboxylic acid, *Phosph. Sulfur Silicon Related Elements*, 188.6(2013), 812-818.

6. WH. Starnes, Structural defects in poly (vinyl chloride), *J. Poly. Sci. Part A: Poly. Chem.*, 43(2005), 2451-2467.

7. E. Alhaydary, E. Yousif, MH. Al-Mashhadani, DS. Ahmed, AH. Jawad, M. Bufaroosha, AA. Ahmed, Sulfamethoxazole as a ligand to synthesize di-and tri-alkyltin (IV) complexes and using as excellent photo-stabilizers for PVC, *J. Poly. Res.,* 2(2021), 1-19.

8. K. Shahid, S. Ali, MH. Bhatti, M. Parvez, Organotin esterification of (E)-3-(3-fluoro-phenyl)-2-(4-chlorophenyl)-2-propenoic acid: synthesis, spectroscopic characterization and in vitro biological activities: Crystal structure of [Ph$_3$Sn (OC (O) C (4-ClC$_6$H$_4$)=CH (3-FC$_6$H$_4$))], *J. Organomet. Chem.*, 690(2005), 1396-1408.

9. A. N. Abed, R. N. Abed, Characterization effect of copper oxide and cobalt oxide nanocomposite on poly (vinyl chloride) doping process for solar energy applications, *Prog. Color Colorants Coat.*, 15(2022), 235-241.

10. A. Ahmed, M. Abdallh, MH. Al-Mashhadani, DS. Ahmed, M. Bufaroosha, AH. Jawad, E. Yousif, Environmental stability of poly (vinyl chloride) modified by schiff's base under exposure to UV, *Biointerf. Res. Appl. Chem.*, 11(2021), 13465-13473.

11. W. Rehman, MK. Baloch, A. Badshah, S. Ali, Synthesis and characterization of biologically potent di-organotin(IV) complexes of mono-methyl glutarate, *J. Chin. Chem. Soc.*, 52(2005), 231–236.

12. LP. Real, AM. Ferraria, AB. do Rego, Comparison of different photo-oxidation conditions of poly (vinyl chloride) for outdoor applications, *Poly. Test*, 27(2008), 743-751.

13. J. Yu, L. Sun, C. Ma, Y. Qiao, H. Yao, Thermal degradation of PVC: A review, *Waste Manag.*, 48(2016), 300-314.

14. MH. Al-Mashhadani, DS. Ahmed, H. Adil, A. Ahmed, H. Thamer, BA. Hamad, M. Abdallh, M. Bufaroosha, SA. Mohammed, N. Salih, RM. Yusop, A quantitative spectroscopic study of the bleaching phenomena in photo-stabilized formulations containing PVC exposed to outdoor conditions, *Mater. Today: Proc.*, 1(2021), 2686-92.

15. G. Gryn'ova, J.L. Hodgson, M.L. Coote, Revising the mechanism of polymer autooxidation, *Org. Biomol. Chem.*, 9(2011), 480-490.

16. H. Hashim, GA. El-Hiti, MH. Alotaibi, DS. Ahmed, E. Yousif, Fabrication of ordered honeycomb porous poly (vinyl chloride) thin film doped with a Schiff base and nickel (II) chloride, *Heliyon.*, 4(2018), e00743.

17. A. Ahmed, MH. Al-Mashhadani, DS. Ahmed, AA. Ahmed, E. Yousif, RM. Yusop, Preparation of Polymeric films containing Schiff base as UV-Absorber with Good Resistance against UV-Photoaging, *Biointerf. Res. Appl. Chem.*, 11(2021), 12743-12749.

18. GA. El-Hiti, MH. Alotaibi, AA. Ahmed, BA. Hamad, DS. Ahmed, A. Ahmed, H. Hashim, E. Yousif, The morphology and performance of poly (vinyl chloride) containing melamine Schiff bases against ultraviolet light, *Molecules*, 24(2019), 803.

19. T. Lu, E. Solis-Ramos, Y. Yi, M. Kumosa, UV degradation model for polymers and polymer matrix composites, *Polym. Degrad. Stab.*, 154(2018), 203-210.

20. M. Sirajuddin, S. Ali, Organotin(IV) carboxylates as promising potential drug candidates in the field of cancer chemotherapy, *Curr. Pharm. Des* 22(2016), 6665-6681.

21. M.M. Romero-Chávez, K. Pineda-Urbina, D.J. Pérez, F. Obledo-Benicio, A. Flores-Parra, Z. Gómez-Sandoval, Á. Ramos-Organillo, Organotin(IV) compounds derived from ibuprofen and cinnamic acids, an alternative into design of anti-inflammatory by the cyclooxygenases (COX-1 and COX-2) pathway, *J. Organomet. Chem.*, 862(2018), 58–70.

22. R.R. Arraq, A. G. Hadi, Enhanced the Antioxidant Activity of Tri Organotin (IV) Complexes derived from Cephalexin, *A.M.J*, 62(2022), 2197-2209.

23. DS. Ahmed, FM. Ibrahim, M. Bufaroosha, MH. Al-Mashhadani, AH. Jawad, RM. Yusop, N. Salih, SA. Mohammed, E. Yousif, Polyphosphates as thermal stabilizers for poly (vinyl chloride), *Mater. Today: Proc.*, 1(2021), 2680-5.

24. E. Arkış, D. Balköse, Thermal stabilisation of poly (vinyl chloride) by organotin compounds, *Poly. Degrad. Stab.*, 88(2005), 46-51.

25. Z. Fadhil, H. Adil, R. Alsayed, MH. Al-Mashhadani, AH. Jawad, DS. Ahmed, E. Yousif, Poly (vinyl Cchloride) containing gynostemma pentaphyllum as a photostabilizer, *Mater. Sci. Forum*, 1021(2021), 251-259.

26. LC. Sawyer, DT. Grubb, GF. Meyers, Specimen preparation methods, *Poly. Micros.,* (2008), 130-247.

27. L. Valko, E. Klein, P. Kovaˇrík, T. Bleha, P. Šimon, Kinetic study of thermal dehydrochlorination of poly(vinyl chloride) in the presence of oxygen: III. Statistical thermodynamic interpretation of the oxygen catalytic activity, *Eur. Polym. J.*, 37(2001), 1123-1132.

28. ET. Al-Tikrity, AA. Yaseen, E. Yousif, DS. Ahmed, MH. Al-Mashhadani, Impact on poly (vinyl chloride) of trimethoprim schiff bases as stabilizers, *Poly. Poly. Composites*, 14(2022), 09673911221094020.

29. S. Nikafshar, O. Zabihi, M. Ahmadi, A. Mirmohseni, M. Taseidifar, M. Naebe, The effect of UV light on the chemical and mechanical properties of a transparent epoxy-diamine system in the presence of an organic UV absorber, *Materials*, 10(2017), 180.

30. A. A. Ahmed, M. H. Al-mashhadani, H. Hashim, D. S. Ahmed, E. Yousif, Morphological, Color Impact and Spectroscopic Studies of New Schiff Base Derived From 1,2,4-Triazole Ring, *Prog. Color Colorants Coat.*, 14(2021), 27-34.

How to cite this article:
R. R. Arraq, A. G. Hadi, D. S. Ahmed, M. H. Al-Mashhadani, H. Hashim, A. A. Ahmed, A. Husain, S. J. Baqir, A. H. Jawad, E. Yousif, Color Changes, AFM and SEM Study of PVC/triorganotin (IV) - Cephalexin Complexes Samples Via UV Radiation. Prog. Color Colorants Coat., 16 (2023), 283-294.

Application of β-CD to Control the Release of ZnO Nanoparticles on the Silk Fabric Surface Along with Citric Acid as Eco-friendly Cross-linker

A. Zare

Department of Textile Engineering, Yazd University, P.O. Box: 89195-741, Yazd, Iran.

ABSTRACT

*O*ver the last two decades, the use of nanoparticles as textile substrates has been the subject of extensive research, aimed at producing finished fabrics with multi-functional performance. The novelty of this article is application of β-cyclodextrin (β-CD) to control the release of zinc oxide nanoparticles (NZnO) on the fabric surface, and therefore it increases the stability and effectiveness time of this substance on the fabric surface. The materials used to treat the silk fabrics were citric acid (CA) as an eco-friendly cross-linking agent and NZnO as a catalyst. In addition, the grafting of β-CD onto the silk fabrics occurred through a pad-dry-cure process. In the other hand, stability of NZnO on the fabric surface investigated by photocatalytic activity before and after of washing. These nanoparticles along with CA were found to be effective in enhancing the crease recovery performance of the silk fabric in wet (233°) and dry states (310°). As the SEM images suggested, the treated fibers had CA, as a cross-linking agent, NZnO deposited on their surface. The results indicated that the as-prepared silk fabric exhibits self-cleaning performance (ΔE>10) and excellent antibacterial activity (>99 % for both E. coli and S. areus). Prog. Color Colorants Coat. 16 (2023), 295-307© Institute for Color Science and Technology.*

1. Introduction

Silk fiber, known as "the queen of textiles", has been widely used in the textile industry. Excellent luster, softness, light weight, availability in different rich colors, aesthetic appearance, good absorbance, skin affinity, human friendliness, and superior wearing comfort are reasons for its use in the textile industry [1-3]. On the other hand, silk has some drawbacks, such as being easy to be dirtied, getting water spots, losing strength when wet [1-4], turning yellow, and even getting degraded by UV irradiation. These drawbacks greatly limit the extensive use of silk fabrics [5]. So, silk fibers are functionalized with other materials.

Certain metal oxides attract great attention as treatment agents to functionalize fabrics due to their withstanding harsh processing situations [6]. As a modifier in the textile industry, zinc oxide (ZnO) is widely applied to functionalize textile substrates. ZnO particles are among the most effective forms of photocatalytic, self-cleaning, antimicrobial, and UV-protective agents. Their high photocatalytic activity, thermal stability, and resistance to UV radiation are the reason for ZnO's usefulness [7-15]. Thus, the use of ZnO has recently increased extensively for producing sunscreens, beauty care products (cosmetics), safety garments, and all kinds of fabrics for the construction industry [16].

The application of nanoparticles to textile materials has been the subject of many studies over the last three

decades. Furthermore, nanoparticles have a large area-to-volume ratio compared to bulk materials, which significantly increases photocatalytic oxidation activity [17-23]. Due to its reasonable photocatalyst activity and nontoxicity, ZnO is suitable for functionalizing fabrics [21-25]. It has a band gap of 3.37 eV and photo-generated holes with adequately strong oxidizing power to decompose many small organic compounds [23-27].

UV-blocking and Superhydrophobic silk fabrics are usually fabricated by the in-situ synthesis of zinc oxide nanorods on silk fabrics, but n-octadecanethiol (ODT) modification process has been practiced by Huang et al. [5] too. As-prepared silk fabrics have superhydrophobic performance (Wrinkle Contact Angle (WCA) > 150°) and excellent anti-UV ability (Ultraviolet Protection Factor (UPF) over 50). The superhydrophobic surfaces have proved to possess excellent mechanical and chemical stability. As-prepared multi-functional silk fabrics will be used in advanced protective textiles and self-cleaning fields.

A Nano-ZnO sol solution was prepared with $Zn(CH_3COO)_2·2H_2O$ as a raw material, and β-cyclodextrin (β-CD) was added to it. Then, cotton fabric was treated with the sol by the pad-dry-cure technique. The results showed that the cotton fabric treated with the sol solution containing β-CD had a better ability to adsorb an essence, photocatalytic degradation to formaldehyde, antibacterial activity, and superior anti-UV property [29, 30].

In another study, citric acid (CA) and maleic acid (MA) as eco-friendly carboxylic acid-based formaldehyde-free cross-linkers were enhanced once three different types of metal oxide nanoparticle (ZnO, MgO, and CaO) were incorporated. The pad-dry-cure fixation method was used with and without UV irradiation. Zinc oxide, MA, and CA were found to be the most effective in enhancing the crease recovery of cotton fabrics [31].

Majumder et al. [13] tried to make biomimetic composite wound dressings by grafting acrylamide and acrylic acid on silk fibroin fabric. The wound dressings had a core layer of silk-woven fabric and an outer layer of poly(acrylic acid-co acrylamide) hydrogel. They were further coated sonochemical with zinc oxide nanoparticles. Salama [12] studied a chitosan/silk fibroin blend as a cost-effective, sustainable, bioactive material for embedding zinc oxide nanoparticles. The results revealed that the chitosan/silk fibroin/zinc oxide is a nanocomposite that can disinfect biomedical applications, such as effectively inhibiting bacterial growth and wound dressing.

Furthermore, poor wet resiliency of silk fabrics during laundering creates problems with washing and wear, a drawback for everyday use [4, 5, 32]. Nontoxic cross-linking agents such as carboxylic acids have been examined to cope with the problem. The most desired compounds for this purpose are citric acid (CA) and 1, 2,3,4-butane tetracarboxylic acid (BTCA). Also, polycarboxylic acids (PCA) are utilized on textile surfaces due to their multi-functional properties, such as high accessibility, environment-friendliness, and the ability for simultaneous antimicrobial and cross-linking finishing [5, 33, 34]. The carboxylic groups of PCA bio-friendly cross-linkers are potential sites for binding metal oxide nanoparticles [35].

As a cross-linking non-formaldehyde reagent and an eco-friendly and economical compound, CA is applied for the durable press finishing of artificial and natural fibers. It has three carboxylic acid groups, which can react with the reactive functional groups of silk, including hydroxyl and amine groups, and form a stable ester and amide bonds, respectively [36-40].

Cyclodextrins (CDs) are biodegradable and have no toxicity. Each CD unit has an interior cavity that can make a complex with a hydrophobic guest molecule. Hence, they can accommodate a variety of organic compounds in their cavities by host-guest complexation [40-44]. Among various types of CD, β-CD is the most accessible, most interesting, and the cheapest [45-47]. Grafting β-CD to fibers allows the properties of β-CD to become intrinsic to the fibers [47-51].

The permanent binding of β-CD onto textile fibers makes the properties of β-CD intrinsic to the fibers [30]. Salimpour [52] treated silk yarns using β-CD and cross-linked them with citric acid (CA). Then, the treated samples were dyed using natural dyes (extracted from carrots, oranges, and tomatoes). As the results showed, the color strength (K/S) of the finished samples had been improved compared to the control sample.

The scientific contribution of the present study is the modification of silk fabric with β-cyclodextrin and citric acid through a pad-dry-cure technique and its curing under UVC radiation. The treated samples were characterized with FTIR, FE-SEM, and DSC. Experiments were also conducted to study the influence of NZnO, β-CD, and CA concentrations in the appropriate percentages of these materials for the best

weight gain, recovery of wrinkle angles in dry and wet states, self-cleaning, and whiteness. The treated fabrics proved to have a good self-cleaning property for the degradation of methylene blue stains under UVA irradiation and the benefit of higher whiteness due to the photoactivity of white NZnO, which is called "nano-photo bleaching".

2. Experimental

As a domestic producer, woven silk fabric with a surface weight of 75 g/m^2 was supplied from Abrisham Guilan, Iran. Na$_2$CO$_3$ and NaOH were purchased from Merck Chemical Co., Germany. NZnO from the US Research Nanomaterials, Inc. (Houston, TX, 77084, USA) was used in this research. The product was a white powder (purity $\geq$ 99 %) with particle diameters ranging from 20 to 30 nm, as reported by the company. β-CD and methylene blue (CI Basic Blue 9) were supplied from Sigma Aldrich, Germany. A commercial anionic detergent was purchased from a domestic producer and applied through a degumming and laundering process.

2.1. Process of degumming the silk fabrics

For two hours, the silk fabrics were first degummed using 2 % Na$_2$CO$_3$ and a 10 % anionic detergent at 98 °C. Then, they were washed with an excessive amount of water and dried at 60 °C for 24 h.

2.2. Preparation of the silk fabric samples and assessment of the grafting percentages

The samples were immersed in finishing solutions with different concentrations of β-CD (0, 5, and 10 % w/w), CA (0, 5, 10 %), and NZnO (0, 0.5, 1 %) for 12 hours at 50 °C in an ultrasonic bath (220 V, 50W, 40 kHz). Then, the finished fabrics were squeezed on a two-roll padder to obtain 90 % wet pickup, dried on a pin frame at 65 °C for 10 minutes, and cured under UVC irradiation (120-300 nm) with an HPA 400S lamp (400W, Philips, Belgium) for 15 minutes. The finished samples were placed in water at 50 °C with 2 g/L detergent for 45 min to eliminate the unreacted β-CD and NZnO. This step was repeated for each finished fabric sample three times. They were dried at ambient temperature for 24 h. The weight of the samples before and after treatment was determined to estimate the percentage of the weight gain chemicals in the samples. The following equation measured it (Eq. 1):

$$\text{weight gain} = \frac{W_2 - W_1}{W_1} \times 100 \qquad (1)$$

W$_1$ and W$_2$ are the weights of the samples before and after the treatment, respectively.

2.3. Evaluation of the properties of the cross-linked silk

2.3.1. Crease recovery angle (CRA) in dry and wet conditions

The dry crease recovery angle (DCRA) and wet crease recovery angle (WCRA) of the warp (w) and filling (f) directions of the cross-linked samples were assessed based on the AATCC testing method 66-2003 [13].

2.3.2. Measurement of bending length (BL) and bending rigidity (BR)

As expressed in bending length, Fabric stiffness was measured according to the ASTM D testing method 1388-96 (2002) [53]. The fabric bending length was tested on a Shirley Bending Length apparatus (Shirley fabric stiffness tester, England). The bending rigidity of the fabrics was calculated using Equation 2 as follows:

$$G = M \times (C)^3 \qquad (2)$$

Where G is the bending rigidity (mg/cm), M is the fabric weight (mg/cm^2), and C is the average bending length (cm).

2.3.3. Self-cleaning properties

The photocatalytic activities of various samples were tested by discoloring an aqueous methylene blue solution before and after exposure to UV-A radiation for 18 hours. The photocatalytic activities were measured as previously suggested [36]. As previously reported [38], the color difference (ΔE) to determine photocatalytic activities were calculated by Equation 3:

$$\Delta E = \sqrt{(\Delta a^*)^2 + (\Delta b^*)^2 + (\Delta L^*)^2} \qquad (3)$$

Where ΔL^*, Δa^*, and Δb^* are the color lightness difference, redness/greenness difference, and yellowness/blueness difference, respectively.

2.3.4. Whiteness index properties

The Whiteness index (WI) was measured with the Hunter Lab spectrophotometer by using an illuminant

D65 and a 10° standard observer. The WIs of the treated and parent samples were evaluated based on the Berger formula as follows (Eq. 4):

$$WI_{Berger} = Y + (a \times Z) - (b \times X) \tag{4}$$

a and b are the numerical parameters with the values of 3.448 and 3.904 for a 10° observer, respectively. Also, X, Y, and Z are the tristimulus values for redness, greenness, and blueness, respectively. The following formula (Eq. 5) measured the changes in WI:

$$\Delta WI = WI_2 - WI_1 \tag{5}$$

WI_1 and WI_2 are the whiteness indices before and after exposure to UV radiation, respectively.

2.3.5. Antibacterial test

An antibacterial test was conducted using the AATCC standard method 100-1999 [52]. Two types of bacteria were used in this test, S. aureus as positive-gram bacteria and E. coli as negative-gram bacteria. The colonies were counted, and the bacteria reduction was calculated with Equation 6:

$$Reduction \text{ \%} = \frac{B-A}{B} \tag{6}$$

A and B are the counted colonies of the treated and parent silk fabrics, respectively [53, 54].

2.4. Fourier transform infrared spectroscopy (FTIR) analysis

The FTIR spectra were analyzed for the untreated and treated silk fabrics in KBr powder using Equinox 55 (Bruker, Germany). The FTIR curves were recorded in the spectral region of 4000–400 cm^{-1}, and KBr powder was applied to collect a background spectrum [55].

2.5. Field emission scanning electron microscopy (FE-SEM)

The surface morphology of the silk fabrics was investigated through field emission scanning electron microscopy (FE-SEM), MIRAIII model, Tescan, Czech Republic. The samples were observed after gold coating.

2.6. Differential scanning calorimetry (DSC)

The thermal properties of the untreated and selected fabrics were examined utilizing differential scanning calorimetry DSC (Q600/TA, USA) at the heating rate of 10°C/min in the temperature range of 25-350 °C.

3. Results and Discussion

3.1. Effects of citric acid, β-CD, and NZnO concentrations on weight gain

The data in Table 1 show that an increase in the concentrations of CA alone or the mixture of CA and β-CD would increase the finished fabrics' weight. The weight of the raw silk increased (from 0 to 15.53 %). As the table also indicates, this rise was due to an increase in CA and -CD concentrations, which is attributed to the ability of citric acid to form links between β-CD and polymeric chains [5]

Moreover, the weight gain values of the treated silk fabrics increased with an increase in the CA concentration, which could be due to the rise in the number of the available citric acid molecules to react with the silk and β-CD molecules [56]. Due to the blocking of NZnO particles by the cross-linking effect of CA, the highest weight gain belonged to the sample which contained the most CA [8, 39].

Table 1 further indicates that the weight gain of the silk fabric increased with an increase in the β-CD concentration by up to 10 %. To account for it, the presence of β-CD in a finishing solution probably promotes the grafting of PCA onto polymeric chains. As seen in the table, the increase of the NZnO concentration from 0 to 0.5 % led to increased weight gain in the treated samples, whereas a further increase in the NZnO concentration beyond 0.5 % in the finishing bath would lead to a decrease in DCRA and WCRA. It is concluded that the irradiation of NZnO with UV light in wet carboxylic acid leads to the formation of protons and positive holes on the surface of ZnO [28, 56]. An excessive quantity of ZnO nanoparticles can react with cross-linkers and block the active sites on them, thus decreasing the crease recovery angle in dry and wet states [31].

Table 1: Effects of CA, β-CD, and NZnO concentrations on the weight gain, DCRA, WCRA, BL, BR, ∆E, and ∆WI of the samples.

code	CA concentration (%)	β-CD concentration (%)	NZnO concentration (%)	Weight gain (%)	DCRA	WCRA	B.L. (cm)	B.R. (mg.cm)	∆WI
1	0	0	0	0	280	174	1.8	4374	-7. 149
2	0	0	0.5	0	280	174	1.8	4374	-7. 125
3	0	0	1	0	280	173	1.7	3685	-7. 045
4	0	5	0	1.1	278	174	1.8	4374	-7. 679
5	0	5	0.5	1.24	276	173	1.8	4374	-7. 637
6	0	5	1	1.39	275	173	1.8	4374	-7. 611
7	0	10	0	1.25	271	172	1.9	5144	-7. 688
8	0	10	0.5	1.44	272	173	1.9	5144	-7. 662
9	0	10	1	1.42	272	172	1.8	5144	-7. 616
10	5	0	0	3.92	290	210	2.3	10403	-7. 469
11	5	0	0.5	4.91	304	219	2.1	7918	-2.750
12	5	0	1	5.54	298	215	2.0	6840	-1. 321
13	5	5	0	10.75	288	204	2.5	13516	-6.951
14	5	5	0.5	11.89	298	211	2.3	10524	-2.268
15	5	5	1	11.92	295	198	2.2	14420	-1.815
16	5	10	0	12.29	284	208	2.8	9210	-6.418
17	5	10	0.5	12.45	293	208	2.5	13594	-2.215
18	5	10	1	12.80	288	202	2.1	8057	-1.318
19	10	0	0	6.11	297	218	2.8	18988	-7.852
20	10	0	0.5	7.10	310	233	2.5	13515	-2.917
21	10	0	1	7.83	301	226	2.2	9263	-1.405
22	10	5	0	11.66	289	214	3.0	23625	-7. 228
23	10	5	0.5	13.22	290	228	2.7	16829	-2.517
24	10	5	1	14.25	288	219	2.4	12303	-0.912
25	10	10	0	14.29	286	211	3.1	26514	-6.914
26	10	10	0.5	14.85	285	222	2.8	20503	-2.217
27	10	10	1	15.53	283	215	2.6	16521	-0.834

3.2. Effects of β-CD, CA, and NZnO concentrations on the DCRA and WCRA of the silk fabrics

Table 1 shows the differences in the properties of the silk materials both before and after treatment with various concentrations of β-CD, CA, and NZnO. The untreated fabric showed the DCRA and WCRA angles of 280° and 174°, respectively. The CRA increased in dry and wet conditions with a 10 % increase in citric acid concentration. Growing CRA was caused by a rise in the cross-links between the chains of silk polymers. The highest increase obtained in DCRA was 10.7 %, but it was 33.9 % for WCRA. However, after cross-linking, the DCRA of the silk fabrics increased less than their WCRA because silk has strong crease recovery in a dry condition, and it is challenging to raise its DCRA further. On this basis, a CA concentration of 10 % was chosen to optimize the other cross-linking conditions. As Table 1 illustrates, when the silk fabrics were treated with 10 % CA and NZnO but without β-CD, DCRA and WCRA increased to 310° and 233°, respectively. In general, all the fabrics treated with a mixture of CA and β-CD had DCRA and WCRA values higher than those of the control sample but lower than the DCRA and WCRA of the sample treated with CA only. NZnO did not significantly affect the DCRA and WCRA performance of the fabrics when applied alone in any concentration.

Citric acid could improve the crease recovery of the silk samples due to the ester (amide) cross-linking of the carboxylic group with the hydroxyl group (or the amine group) of the fabrics. Increasing the cross-linker concentration enhanced the cross-linking and, thus, the crease recovery [31]. Indeed, CA improved DCRA and WCRA gradually but considerably as its concentration rose from 0 to 10 %. Metal oxides are expected to facilitate the formation of hydrates due to photocatalytic activities and, as a result, to promote the cross-linking of carboxylic acid-based cross-linkers and cellulose [31]. This study achieved the best crease recovery angles of 310° and 233° by incorporating 0.5 % NZnO to 10 % CA.

3.3. Measuring the bending length (BL) and the bending rigidity (BR) of the parent and treated fabrics

A fabric handle is one of the key parameters in fabric selection. Bending length (BL) and bending rigidity (BR) are the major fabric handle indicators. Cross-linking agents can adversely affect the fabric handle. As it was found in this study, the incorporation of nanoparticles with CA not only improves the crease recovery angle of fabrics but also bears a positive effect on the fabric handle due to the reduction of inter-yarn friction. The sample treated with 10 % CA and 10 % β-CD proved to have the highest bending length and bending rigidity values. Adding 0.5 % ZnO NPs also improved the fabric handle by reducing the bending length and the bending rigidity (Table 1).

3.4. Changes in the whiteness index of the parent and treated samples before and after UV irradiation

This Measurement of the change in the whiteness index (ΔWI) of the samples before and after UV irradiation showed that the ΔWI was high without NZnO (Table 1), which can be explained by the ability of NZnO to protect the surface of fibers. When the concentration of CA and β-CD is very high, a layer is created on the fabric's surface due to the severe reaction of the finishing material with the fiber, reducing the fabric's whiteness. The layer covering the silk fibers' surface reduces UV irradiation's destructive effect. Hence, the ΔWI decreases.

3.5. FTIR analysis

A series of FTIR analyses were conducted on the parent silk fabric and the UV-cured fabrics treated with 10 % CA, 10 % CA + 10 % β-CD, and 10 % CA + 10 % β-CD+1 % NZnO. The results are shown in Figures 1a to 1d, respectively. The strong band at 1625 cm^{-1} in the spectrum of the parent fabric in Figure 1a is related to the silk fabric's carbonyl stretching (amide I band). Figures 1b and 1c show the removal of a "shoulder" in the higher-frequency regions of the spectra of the silk treated with CA and that treated with a combination of CA and β-CD. The peak at 1128 cm^{-1} (C–C and C–O vibration) is related to cyclodextrin in the grafted fabric. This peak suggests the esterification reaction of the carboxylic groups in CA with the hydroxyl groups in β-CD and silk fibroin. In addition, the peaks at 1002 cm^{-1} (C–O–C stretching vibration), 1039 cm^{-1} (C–O stretching vibration), and 2924 cm^{-1} (C–H stretching vibration) indicate the existence of β-CD on the silk fabric (Figure 1c). The stretch in the region around 690-880 cm^{-1} is considered due to the metal-oxygen

bonding vibration of NZnO (Figure 1d). Figure 2 proposes a suggested mechanism of the grafting reaction of β--CD on the silk fabric using NZnO as the catalyst.

3.6. Scanning electron microscope (SEM) analysis

The fabric treated with 10 % CA, 10 % β-CA, and 1 % NZnO had the best weight gain with optimum improvement in its photocatalytic property and whiteness. The SEM images of this sample helped to study its surface morphology compared to the parent sample and the sample treated with CA only.

Figure 3 shows the SEM images of the treated and the parent fabrics. As can be seen, the parent fabric is clean and without any coating (Figure 3a). However, the cross-linker coating is quite obvious on the surface of the fibers in the fabric treated with 10 % CA (Figure 3b).
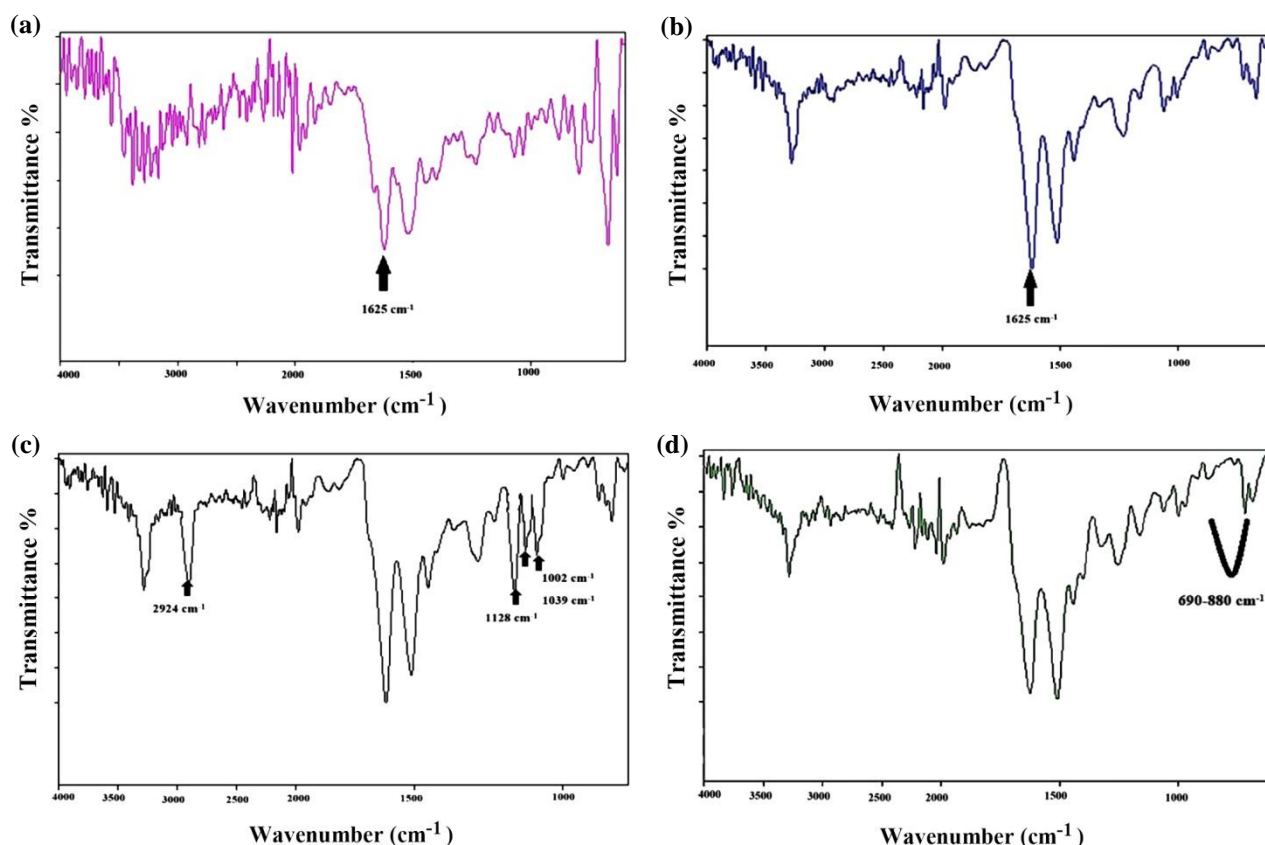

Figure 1: FTIR spectra of the selected samples in the presence of CA, β-CA, and NZnO: (a) untreated sample, (b) sample treated with (10 %) citric acid, (c) sample treated with (10 %) citric acid and (10 %) β-CD and (d) sample treated with citric (10 %) acid, (10 %) β-CD and (1 %) NZnO
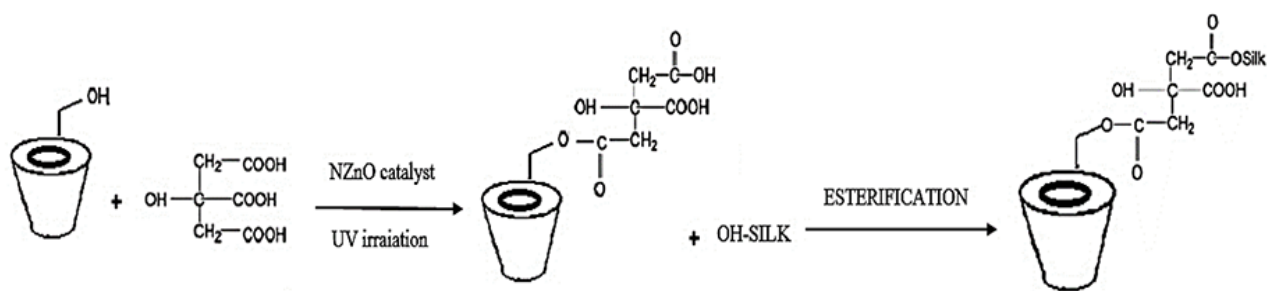

Figure 2: The suggested mechanism of the grafting reaction of β-CD on the silk fabric.
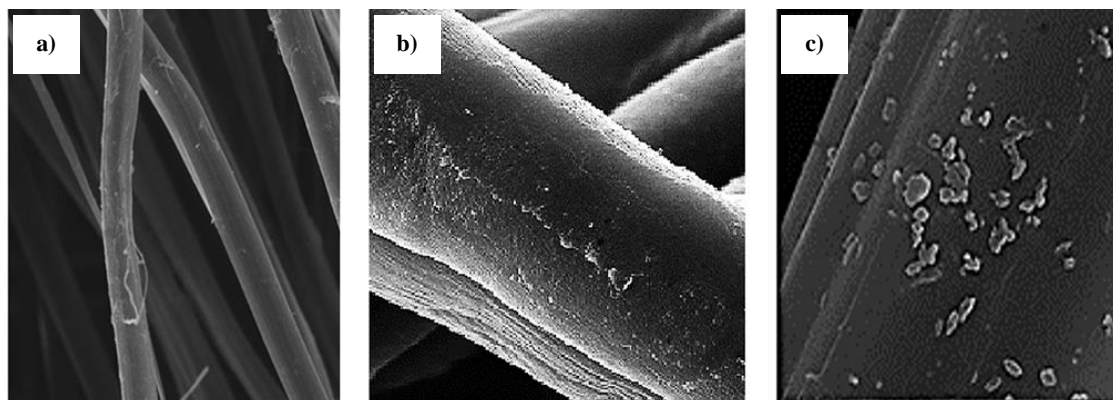
Figure 3: SEM images of the samples: (a) Untreated, (b) treated with CA and (c) treated with CA and NZnO.

Figure 3 c shows the sample treated with CA and NZnO. NZnO is found deposited on the fabric's surface treated with nano-ZnO sol, nano-ZnO/β-CD sol, and a CA cross-linker. It is concluded from the SEM images that the deposition of nanoparticles on a fabric surface can occur in the presence of CA.

3.7. DSC analysis

The DSC curves of the untreated silk fabric and the β-CD/CA-treated fabric are presented in Figure 3. The curve of the untreated fabric shows two endothermic peaks at 49 °C and 321 °C due to water loss and silk chains' thermal degradation, respectively (Figure 4 a). Following the cross-linking, the peak at 321 °C shifted to a higher temperature of about 7 °C, as shown in Figure 4 b. The exothermic peak at 210-280 °C is due to the conformational transition from a random coil to the β-sheet structure of the silk fiber. The non-grafted samples showed no trace of thermal transitions at low temperatures. In contrast, the grafted one had a broad endothermic temperature of about 177 °C, which is related to the degradation of citric acid.
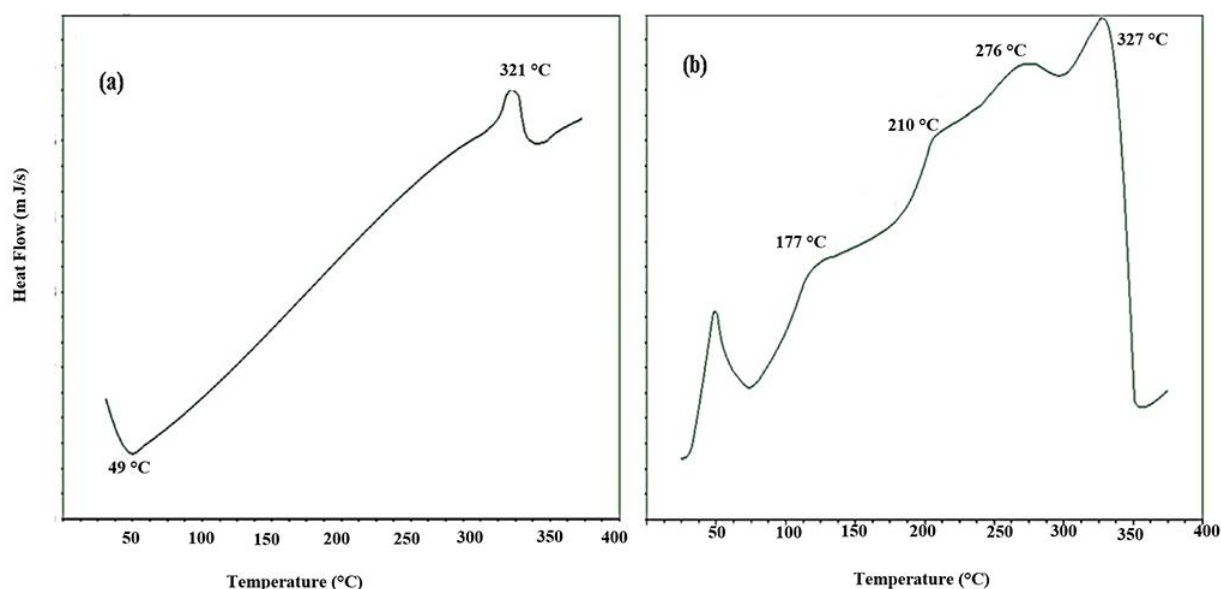

Figure 4: DSC curves of (a) the untreated silk fabric and (b) the β-CD grafted silk fabric (10 % β-CD, 10 % CA).

3.8. Antibacterial activity of the fabrics

Table 2 shows the reduction percentages of Escherichia coli (E.coli) and Staphylococcus aureus (S.aureus) bacteria of the samples treated with CA, β-CD, and NZnO under UV irradiation. It was found that an increase in the CA concentration would decrease both types of bacteria considerably. This reduction could be due to the carboxylic groups of CA that induced the higher absorption of NZnO particles on the fabric surface through electrostatic interaction. In addition, the presence of small quantities of NZnO with CA considerably improved the effectiveness of CA against S. aureus and E. coli. Therefore, it can be concluded that incorporating NZnO into CA makes the care of treated fabrics easy and improves their antibacterial function.

The untreated fabric was attacked by S. aureus and E. coli microbes and showed no inhibitory reaction. However, due to their acidic properties, the fabrics treated with CA had strong antimicrobial activity against both S. aureus and E. coli. A combination of NPs with cross-linkers had a better antibacterial effect than each of the components alone, which was evidence of the improved antibacterial activity of the cross-linker in the presence of NPs. The highest bacteria reduction was 98.81 % for E.coli and 98.25 % for S. aureus. These values belonged to the sample treated with 1 % NZnO and 10 % CA but no β-CD.

As can be seen in Table 2, S. aureus exhibited more resistance than E.coli. Gram-positive bacteria have thicker cellular walls than gram-negative microbes. Thus, they have a relatively higher resistance to antibacterial agents. In this study, CA and NZnO particles had a synergistic effect that significantly reduced E.coli and S.aueus bacteria. The B-CD treatment modified the silk fiber surfaces before applying the fabric with nano-ZnO and helped increase the nanoparticle absorption on the fabric surface. The nano-ZnO actually acted as an excellent antibacterial agent on the textile. The application of CA along with nano-ZnO powder in the finishing bath helped to load ZnO on the treated silk fabric, which enhanced the functional properties of the resulting fabrics.

3.9. Photocatalytic decomposition of methylene blue under UV irradiation

The color differences (ΔE^*) of the fabrics treated with CA, β-CD, and NZnO are reported in Table 3. The ΔE^* symbol denotes the difference between the color indices before and after 18 h of UV irradiation. As indicated, ΔE^* increased when the CA and NZnO concentrations were grown. The treated samples had considerable color differences from the untreated ones because their surface was prepared by polycarboxylic acid to attract more NZnO particles. Furthermore, the reactions of CA and hydroxyl with the amine groups of silk fibroin chains created more carboxylic acid on the silk surface, which led to the salt attraction of NZnO. Having three functional groups, CA could introduce strong cross-links that assisted the absorption of more NZnO on the fabric surface. As it was found, more NZnO particles on the fabric's surface can increase the photodegradation of methylene blue dye by UV irradiation [34].

The self-cleaning properties of ZnO-loaded textiles are due to the highly oxidative intermediates created on the surface of the fabrics [57]. Citric acid is a good cross-linking agent with three carboxylic groups, which help form strong ZnO attachments to the fabric surface. Also, the photocatalytic decomposition of CA-treated fabrics yields better results than that of untreated ones [57-59].

Table 2: Bacterial reduction by the selected samples.

Code	Reduction of E.coli (%)	Reduction of S.areus (%)
1	0.00	0.00
7	0.00	0.00
19	75.54	72.93
20	87.33	82.48
21	98.81	98.25
27	99.90	99.76

Irradiation of ZnO with UV generates electron-hole pairs which induce redox reactions at the surface of the photocatalyst (Figure 5). Thus, nano-ZnO can decompose common organic matter, dye molecules, and bacterial cell membranes [60].
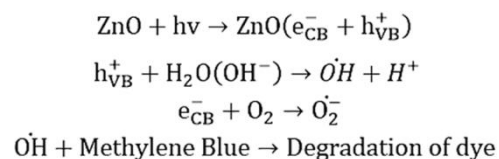
$$ZnO + hv \rightarrow ZnO(e_{CB}^{-} + h_{VB}^{+})$$
$$h_{VB}^{+} + H_2O(OH^{-}) \rightarrow \dot{O}H + H^{+}$$
$$e_{CB}^{-} + O_2 \rightarrow \dot{O}_2^{-}$$
$$\dot{O}H + \text{Methylene Blue} \rightarrow \text{Degradation of dye}$$

Figure 5: Photocatalytic mechanism of ZnO

Table 3: Effects of CA, β-CD, and NZnO concentrations on the color difference (ΔE*) of the silk fabrics dyed with methylene blue in different UV exposure times.

Code	ΔE* for 18 h before washing	ΔE* for 18 h after washing
1	0.0	0.0
2	0.0	0.0
3	0.0	0.0
4	0.0	0.0
5	0.4	0.0
6	0.5	0.0
7	0.0	0.0
8	0.8	0.0
9	0.9	0.0
10	0.0	0.0
11	4.5	4.2
12	9.0	8.8
13	0. 0	0.0
14	4.5	4.3
15	9.2	9.0
16	0.3	0.0
17	4.5	4.4
18	9.3	9.3
19	0.4	0.1
20	4.7	4.4
21	10.1	9.8
22	0.4	0.2
23	5.8	5.6
24	11.3	10.9
25	0.6	0.2
26	7.5	7.5
27	12.3	12.3

The silk fabric treated with β-CD had better anti-ultraviolet radiation and antibacterial and photocatalytic degradation. This treatment proved to be an effective method of providing multi-functional properties for textiles. After 18 h, the self-cleaning properties of the samples were evaluated before and after washing (Table 3) to assess the stability of nanoparticles on the fabric surface. The results suggested that the samples treated with CA along NZnO have appropriate photocatalytic activity even after washing. Generally, samples treated with CA with or without β-CD haven't significant difference ΔE* before and after washing. Conversely, the β-CD-treated silk fabric, along with CA, could preserve the photocatalytic property of the samples because β-CD has a hydrophobic internal cavity that can adsorb nano-ZnO particles by the host-guest complex and release them slowly.

4. Conclusion

Eliminating the need for toxic catalysts and high temperatures helped to provide better crease recovery angles. The proposed process is environmentally friendly, inexpensive, and suitable for common and large-scale industrial applications. The present study sought advantages such as appropriate DCRA and WCRA and photocatalytic activities without negative effects on the handle and whiteness indices of treated silk fabrics. For this purpose, β-CD and CA, as cross-linking agents, were used on silk fabric to enhance their photocatalytic and antibacterial properties through the adsorption of nanoparticles. As the results showed, CA and NZnO under UV curing could synergistically enhance the cross-linking process, DCRA and WCRA, and the self-cleaning property of the fabrics. The textiles produced through treatment with CA and β-CD proved applicable in drug delivery systems.

5. References

1. N. Balci, Z. Ömerogulallari, D. Kut, H. A. Eren, Effects of plasma and ozone treatments on tensile and whiteness properties of 100% silk, *J. Fac. Ing.,* 20(2015), 43-56.
2. G. Li, H. Liu, T. D. Li, J. Wang, Surface modification and functionalization of silk fibroin fibers/fabric toward high performance applications, *Mater. Sci. Eng. C,* 32(2012), 627–636.
3. Zh. Hadisi, M. Farokhi, H. R. Bakhsheshi-Rad, M. Jahanshahi, S. Hasanpour, E. Pagan, A. Dolatshahi-Pirouz, Y. Sh. Zhang, S. C. Kundu, M. Akbari, Hyaluronic acid (HA)-based silk fibroin/zinc oxide core–shell electrospun dressing for burn wound management, *Macromol. Biosci.,* 2020, 1-17.
4. N. Reddy, K. Warner, Yi. Yang, Low-temperature wet-crosslinking of silk with citric acid, *Ind. Eng. Chem.*, 50(2011), 4458-4463.
5. J. Huang, Y. Yang, L. Yang, Y. Bu, T. Xia, Sh. Gu, H. Yang, D. Ye, W. Xu, Fabrication of multifunctional silk fabrics via one step in-situ synthesis of ZnO, *Mater. Lett.*, 237(2019), 149-151.
6. A. M. Nafchi, A.K. Alias, S. Mahmud, M. Robal, Antimicrobial, rheological, and physicochemical properties of sago starch films filled with nanorod-rich zinc oxide, *J. Food Eng.,* 113(2012), 511-519.
7. A. Amani, M. Montazer, M. Mahmoudirad, Synthesis of applicable hydrogel corn silk/ZnO nanocomposites on polyester fabric with antimicrobial properties and low cytotoxicity, *Int. J. Biol. Macromol.* , 123(2019), 1079-1090.
8. A. Nazari, M. Montazer, A. Rashidi, M. Yazdanshenas, M. Anary-Abbasinejad, Nano TiO2 photo-catalyst and sodium hypophosphite for cross-linking cotton with poly carboxylic acids under UV and high temperature, *Appl. Catal. A-Gen,* 371(2009),10-16.
9. A. Verbič, M. Gorjanc, B. Simoncic, Zinc oxide for functional textile coatings: recent advances, *Coatings*, 9(2019), 1-26.
10. S. Kathirvelua, L. D'Souza, B Dhurai, UV protection finishing of textiles using ZnO nanoparticles, *Indian. J. Fibre Text. Res.*, 34(2009), 267-273.
11. S. M. Gawish, A.M. Ramadan, S.M. Abo El-Ola, A.A. Abou El-Kheir, Citric acid used as a cross-linking agent for grafting β-cyclodextrin onto wool fabric, *Polym. Plast. Technol. Eng.*, 48(2009), 701-710.
12. A. Salama, Chitosan/silk fibroin/zinc oxide nanocomposite as a sustainable and antimicrobial biomaterial, *Cellul. Chem. Technol.,* 52(2018), 903907.
13. S. Majumder, U.R. Dahiya, S. Yadav, P. Sharma, D. Ghosh, G.K. Rao, V. Rawat, G. Kumar, A. Kumar, Ch.M. Srivastava, Zinc oxide nanoparticles functionalized on hydrogel grafted silk fibroin fabrics as efficient composite dressing, *Biomolecules*, 10(2020), 710-723.
14. M. T. Noman, N. Amor, M. Petru, A. Mahmood, P. Kejzlar, Photocatalytic behaviour of zinc oxide nanostructures on surface activation of polymeric fibres, *Polym. J.,* 13(2021), 1227-1244.
15. M. Mazarji, Gh. Nabi Bidhendi, N. M. Mahmoodi, Mathematical modelling of an annular photocatalytic reactor for methylene blue degradation under UV light irradiation using rGO-ZnO hybrid, *Prog. Color Colorants Coat.,* 4(2011), 85-94
16. B. Malaikozhundan, J. Vinodhini, Nanopesticidal

effects of pongamia pinnata leaf extract coated zinc oxide nanoparticle against the Pulse beetle, callosobruchus maculatus, *Mater. Today Commun.,* 14(2018), 106-115.

17. N Durán, P. D. Marcato, GIH De Souza, O. L. Alves, E. Esposito, Antibacterial effect of silver nanoparticles produced by fungal process on textile fabrics and their effluent treatment, *J. Biomed. Nanotech*, 3(2007), 203-208.

18. B. Fei, Z. Deng, J. H. Xin, Y. Zhang, G. Pang, Room temperature synthesis of rutile nanorods and their applications on cloth, *Nanotechnology*, 17(2006), 1927-1931.

19. J. H. Xin, W. A. Daoud, Y. Y. Kong, A new approach to UV-blocking treatment for cotton fabrics, *Text. Res. J.,* 74(2004), 97-100.

20. H. J. Lee, S. Y. Yeo, S. H. Jeong, Antibacterial effect of nanosized silver colloidal solution on textile fabrics, *J. Mater. Sci.,* 38(2003), 2199-2204.

21. A. Yadav, V. Prasad, A. A. Kathe, S. Raj, D. Yadav, C. Sundaramoorthy, N. Vigneshwaran, Functional finishing in cotton fabrics using zinc oxide nanoparticles, *Bull. Mater. Sci.,* 29(2006), 641-645.

22. M. Khajeh Aminian, F. Sajadi, M. R. Mohammadizadeh, S. Fatah, Hydrophilic and photocatalytic properties of TiO$_2$/SiO$_2$ nano-layers in dry weather, *Prog. Color Colorants Coat,.* 14 (2021), 221-232.

23. S. Rasouli, Sh. Saket, One step rapid synthesis of nano-crystalline ZnO by microwave-assisted solution combustion method, *Prog. Color Colorants Coat.,* 3(2010), 19-25.

24. H. Sudrajat, Superior photocatalytic activity of polyester fabrics coated with zinc oxide from waste hot dipping zinc, *J. Clean. Prod.,* 172(2018), 1722-1729.

25. A. Hatamie, A. Khan, M. Golabi, A. P. F. Turner, V. Beni, W. Cheung Mak, A. Sadollahkhani, H. Alnoor, B. Zargar, S. Bano, O. Nur, M. Willander, Zinc oxide nanostructures modified textile and its application to biosensing, photocatalytic and as antibacterial material, *Langmuir*, (2015), 1-23.

26. R. Sahaa, S. Karthika, P. M. R. Subbiah, A. Kumar, R. Suriyaprabha, V. Rajendran, Psidium guajava leaf extract-mediated synthesis of ZnO nanoparticles under different processing parameters for hydrophobic and antibacterial finishing over cotton fabrics, *Prog. Org. Coat,* 124(2018), 80-91.

27. M. Rastgoo, M. Montazer, T. Harifia, M. Mahmoudirad, In-situ sonosynthesis of cobblestone-like ZnO nanoparticles on cotton/polyester fabric improving photo, bio and sonocatalytic activities along with low toxicity and enhanced mechanical properties, *Mater. Sci. Semicond. Proc.,* 66(2017), 92-98.

28. A. Amani, M. Montazer, M. Mahmoudirad, Low starch/corn silk/ZnO as environmentally friendly nanocomposites assembling on PET fabrics, *Int. J. Biol. Macromol.*, 170(2021), 780-792.

29. H. Poortavasoly, M. Montazer, T. Harifi, Aminolysis of polyethylene terephthalate surface along with in situ synthesis and stabilizing ZnO nanoparticles using triethanolamine optimized with response surface methodology, *Mater. Sci. Eng. C.*, 58(2016), 495-503.

30. Ch.Wang, J. He, Research on the multifunction fabric loaded with Nano-ZnO and β-cyclodextrin, *Adv. Mater. Res.*, 332-334(2011), 1439-1442.

31. N. Sarwar, M. Ashraf, M. Mohsin, A. Rehman, A. Younus, A. Javid, K. Iqbal, Sh. Riaz, Multifunctional formaldehyde free finishing of cotton by using metal oxide nanoparticles and ecofriendly cross-linkers, *Fiber. Polym.*, 20(2019), 2326-233.

32. A. Zare, Citric acid as environment friendly crease-resistance finishing agent for silk fabric combined by β-cyclodextrin, *Res. J. Text. Appar.,* 26(2022), 238-254.

33. Y. Yang, S. Li, Silk fabric non-formaldehyde crease-resistant finishing using citric acid, *J. Text. Inst.,* 84(1993), 638-644.

34. A. Nazari, M. Montazer, N. Nasirizadeh, B. Namiranian, Cellulase pretreatment on mercerized cotton to enhance x-linking, self-cleaning, and antibacterial properties Using Nano TiO$_2$/CA/BTCA: statistical approaches, *J. Eng. Fibers Fabr.,* 8(2013), 114-125.

35. M. A. Shirgholami, A. Nazari, M. Mirjalili, Statistical optimization of self-cleaning technology and color reduction in wool fabric by nano zinc oxide and eco-friendly cross-linker, *Clean. Technol. Environ. Policy,* 17(2014), 1-15.

36. A. Zare, P. Payvand, The prediction of optimal conditions for the surface grafting of b -cyclodextrin onto silk fabrics by an artificial neural network (ANN), *Pigm. Resin Technol.,* 52(2023), 183-191.

37. A. Dixit, K. Wazarkar, A. S.Sabnis, Antimicrobial UV curable wood coatings based on citric acid, *Pigm. Resin Technol.*, 5(2021), 1-10.

38. B. Martel, M. Weltrowski, D. Ruffin, M. Morcellet, Polycarboxylic acids as crosslinking agents for grafting cyclodextrins onto cotton and wool fabrics: Study of the process parameters*, J. Appl. Polym. Sci.,* 83(2002), 1449-1456.

39. B. Voncina, M. A. Marechal L, Grafting of cotton with β-cyclodextrin via poly(carboxylic acid), *J. Appl. Polym. Sci.*, 96(2005), 1323-1328.

40. A. Abou Okeil, Citric acid crosslinking of cellulose uUsing TiO$_2$ catalyst by pad-dry-cure method, *Polym. Plast Technol. Eng.*, 47(2008), 174-179.

41. M. Nazi, R. M. A. Malek1, M. B. Moghadam, Effect of processing conditions on producing a reactive derivative from b-cyclodextrin with itaconic acid, *starch*, 64(2012), 794-802.

42. W. Misiuk, M. Zalewska, Study on the inclusion interactions of β-cyclodextrin and its derivative with clomipramine by spectroscopy and its analytic application., *Anal. Lett.,* 41(2008), 543–560.

43. T. Loftsson, M. Masson, Cyclodextrins in topical drug formulations: theory and practice, *Incl. Phenom. Macrocycl. Chem.*, 225(2001), 15-30.

44. H. J. Buschmann, D. Knittel, E. Schollmeyer, New

textile applications of cyclodextrins, *J. Incl. Phenom. Macrocycle. Chem.,* 40(2001), 169-172.

45. J. Szejtli, Utilization of cyclodextrins in industrial products and processes, *J. Mater. Chem.*, 7(1997), 575-587.

46. F. M. Bezerra, M. J. Lis, H. B. Firmino, The role of β-cyclodextrin in the textile industry-Review, *Molecules*, 25(2020), 3624-3651.

47. M. Rehana, S. A. Mahmoudb, H. M. Mashalyb, B. M. Youssef, β-Cyclodextrin assisted simultaneous preparation and dyeing acid dyes onto cotton fabric, *React. Funct. Polym.,* 151(2020), 1-9.

48. M Shabbir, SH. Ahmed, J. N. Sheikh, In frontiers of textile materials: polymers, nanomaterials, enzymes, and advanced modification techniques, Wiley-Scrivener, New York, 2020, 87-98.

49. G. Ibrahim, Fragrance finishing of cellulosic fabrics, *Int. Des. J.,* 6(2016), 251-259.

50. U. R. Bhaskara, A.Tourrette, D. Jocic, M. M. C. G. Warmoeskerken, Attachment of β-cyclodextrins on cotton and influence of β-cyclodextrin on ester formation with BTCA on cotton, *AATCC J. Res.,* 1(2014), 28-38.

51. M. Nazi , R. M. A. Malek, R. Kotek, Modification of β-cyclodextrin with itaconicacidand application of the newderivative to cotton fabrics, *Carbohydr. Polym.*, 88(2012), 950-958.

52. S. Salimpour Abkenar, Dyeing properties of natural dyes on silk treated with ß-cyclodextrin, *Int. J. Mater. Eng.,* 15(2021), 37-42.

53. L. Ammayappan, J. J. Moses, An overview on application of cyclodextrins in textile product enhancement, *J. Text. Assoc.,* 70(2009), 9-16.

54. M. Khajeh Mehrizi, F. Malekan, M. Veysian, Z. Shahi, The effect of different nanoparticles on dyed wool carpet with walnut shell natural dye, *Prog. Color Colorants Coat.*, 16 (2023), 231-241.

55. L. Mehraz , M. Nouri, Preparation and characterization of β-cyclodextrin grafted silk fabric, *J. Nat. Fibers*, 17(2020), 371-381.

56. S. Periyasamy, M. L. Gulrajani, D. Gupta, Preparation of a multifunctional mulberry silk fabric having hydrophobic and hydrophilic surfaces using VUV excimer lamp, *Surf. Coat. Technol.,* 201(2007), 7286-7291.

57. M. Montazer, S. Seifollahzadeh, Enhanced self-cleaning, antibacterial and UV protection properties of nano TiO$_2$ treated textile through enzymatic pretreatment, *Photochem. Photobiol.,* 87(2011), 877-883.

58. I. K. Konstantinou, T. A. Albanis, TiO$_2$-assisted photocatalytic degradation of azo dyes in aqueous solution: Kinetic and mechanistic investigations a review, *Appl. Catal. B*, 49(2004), 1-14.

59. A. Fujishima, X. Zhang, D. A. Tryk, TiO$_2$ photocatalysis and related surface phenomena, *Surf. Sci. Rep.,* 63(2008), 515-582.

60. R. Dastjerdi, M. Montazer, S. Shahsavan, A novel technique for producing durable multifunctional textiles using nanocomposite coating, *Colloids Surf. B.,* 81(2010), 32-41.

Dispersion of Silica Aerogel Particles in Thermal Insulating Waterborne Coating

F. Raoufi[1], Sh. Montazeri[*1], S. Rastegar[2], S. Asadi[3], Z. Ranjbar[1,4]**

[1.] Department of Surface Coatings and Corrosion, Institute for Color Science and Technology, P.O. Box: 16765-654, Tehran, Iran

[2.] RadSys Pooshesh Co., P.O. Box: 16765-654, Tehran, Iran

3. Department of Architectural Engineering, The Pennsylvania State University, P.O. Box: 16880, Pennsylvania, USA.

[4.] International Scientific Studies and Collaboration (CISSC), P.O. Box: 131498365, Tehran- Iran

ABSTRACT

Nowadays, thermal insulation coatings have attracted considerable attention as they are one of the most practical solutions to reduce energy consumption, by which greenhouse gas emissions are reduced. To prepare this composite, water-borne acrylic resin containing nano porous structures i.e. silica aerogel with two different particle sizes were considered. Firstly, the dispersion of the nano porous particles in water-borne acrylic resin was investigated. The main challenge was wetting and dispersing of aerogel particles in the waterborne resin, without any penetration of the dispersion medium in the nano pores. Three types of dispersant were used, and the dispersing process efficiency was characterized by a particle size analyzing, rheological behavior, zeta potential, and electron microscopy. The experimental results indicated that an anionic surfactant (sulfosuccinate) was more efficient than non-ionic surfactants (alkyl EO/PO copolymer and octylphenol ethoxylate). Additionally, the sufficient method to disperse the particles in water, and acrylic resin was studied. Owing to the consequences of the final particle size, the rheological behavior of the dispersion, and the diffusion of the medium into the nano pores, mechanical mixing with a mild shear rate and short mixing time was adopted. The thermal conductivity of the prepared coatings containing 2, 4, and 6 wt. % of aerogel particles was measured. The effect of concentration and size of aerogel particles on the thermal conductivity of acrylic film was evident. The results showed that it was possible to reduce 37-46 % of thermal conductivity using 6 wt. % of silica porous aerogels in the coating. Finally, the thermal transmittance (u-value) of a typical wall with the optimum insulating coating was calculated according to ISO 9869 standard. The results showed that the u-value would decrease by 24 % if the optimum coating was used with a thickness of 1.5 mm. Prog. Color Colorants Coat. 16 (2023), 309-317© Institute for Color Science and Technology.

1. Introduction

There has been an increasing need for innovative thermal insulating coatings with high thermal properties to achieve energy efficiency on façades of buildings. This can be accomplished through the incorporation of nano porous materials in new thermal

insulating coating formulations [1, 2].

Silica aerogel is a nano porous structure whose unique features such as very low density, high porosity, high specific surface area, and very low thermal conductivity coefficient have caused it to be widely used in thermal insulation coating applications [3-7]. The main challenge in using silica aerogel in water-borne thermal insulation coatings is the dispersion of these hydrophobic particles. Silica aerogels should be hydrophobic to maintain the stagnant air inside the pores, which is responsible for low thermal conductivity. Therefore, the pores should not be filled with water/water-borne resin. Furthermore, the hydrophobicity of silica aerogel prevents their wetting, homogenous distribution, and dispersion stability [8-11].

Pidhurney and Pescatore [12] compared the effect of aerogel and hollow microspheres on the thermal conductivity of water-borne acrylic-styrene latex resins. They showed that hollow microspheres were more effective in reducing the thermal conductivity of the coating. This result was surprising for them as the density of aerogel is lower than microspheres; hence, the coating based on aerogel should have a lower density, so that the more the stagnant air is, the lower the thermal conductivity is. They attributed this observation to the penetration of the polymers into the open pore structure of silica aerogel and replaced it with stagnant air. Moreover, Burchill [13] observed that it was practically impossible to include more than 0.5 wt. % of hydrophobic aerogels inside the water-borne acrylic dispersion due to the superhydrophobicity and fragility at the high shear rate of aerogel particles. In addition, he stated that the inclusion of these particles into the dispersion significantly increased the viscosity of the dispersion and practically made the application of the coating impossible. To solve the problems, he used surface active agents to disperse the aerogel particles inside the system. Liao et al. [14] made a thin film composite containing surface-modified silica hollow spheres and water-borne polyurethane with excellent insulating properties. Zhao et al. [15] fabricated an insulating composite based on epoxy resin and silica aerogel. They used silica aerogel with different particle sizes in a thermosetting epoxy resin. They achieved a thermal conductivity of 0.105 W/(m·K) in 60 wt. % of silica aerogel in the coating. He et al. [16] made a thermal insulation coating by mixing silica aerogel and emulsion acrylic and investigated the relationship

between thermal conductivity and volume fraction, density, and particle size in the composites. They reported that aerogels only improved the thermal conductivity in volume fractions of more than 30 wt. %. Chukhlanov et al. [17] studied the heat insulation coating based on poly-organosiloxane composites and hollow glass microsphere fillers. They reported that the lower the thermal conductivity, the higher the filler concentration. Bahrami et al. [18] made epoxy-based thermal insulation coatings containing three types of hollow glass microspheres with different particle sizes in epoxy base coatings. They found that the larger the hollow microspheres, the better the insulating performance. Kang et al. [19] improved the polyacrylate film properties using hollow titanium dioxide spheres with physical mixing. They obtained the optimal shell thickness of hollow titanium dioxide spheres of 43 nm.

In studies conducted to investigate the thermal behavior of insulation coatings, different models have been proposed to explain the effective thermal conductivity. The core-shell model is one of the most commonly used models [20]. In this model, aerogel particles inside the resin dispersion are considered spheres whose core are dry aerogel and have a different heat transfer coefficient than the shell. In this case, the shell is a part of the aerogel particle that is penetrated by resin and has a different heat transfer coefficient from the core and the resin part [11, 15].

The diameter of the shell can completely affect the final heat transfer coefficient, and this diameter is dependent on the penetration rate of the resin dispersion into the pores inside aerogel particles. The present research has tried to reach the optimal state between aerogel dispersion and its stability and the insulating properties of the final composite in the form of a dry coating film.

The main purpose of this research is Dispersing of hydrophobic silica aerosol in water born acrylic coating to have a stable dispersion, without any penetration of the dispersion medium in the pores for preparing an efficient insulating composite coating. It has been added to the last paragraph of the introduction.

2. Experimental

2.1. Materials

In this study, aerogel particles were dispersed in water borne acrylic resin by different methods. Then, coating applied on the surface and thermal conductivity of

water-borne acrylic coatings containing aerogel particles was measured. Finally, the effect of prepared insulative coatings on the saving energy has been reported.

In this study, two types of hydrophobic aerogel particles (Figure 1), ENOVA IC3110 (20-40 mμ) and ENOVA IC3100 (100-700 μm), Cabot Co. (USA) were used (Thermal conductivity = 0.012 W/m.K).

Polyfam 748 acrylic resin, an emulsion acrylic copolymer based on methacrylic acid esters and without any plasticizer, purchased from Resinfam Company (Iran), was used as a water-borne acrylic resin (Solid content: 54 %, Viscosity: 200 cP).

Sodium sulfosuccinate ester (TRITON^TM GR-5M), an anionic dispersing agent, alkyl EO/PO copolymer (TERGITOL^TM XD), and octylphenol ethoxylate (TRITON L^TM X100), two nonionic surfactants, from DOW Co., USA, were used for wetting and dispersing aerogel particles and TroyKyd D720, an anti-foam additive from Troy Co. were used as received.

2.2. Dispersing aerogels in acrylic resin

Three methods for dispersing were used as follows:

Method 1- The desired amount of the dispersing agent and anti-foam is added to the acrylic resin, and mixed well. Then, the specific amount of aerogel is added to the mixture and then mixed for 4 hours at 2800 rpm using a mechanical stirrer (Heidolph, RZR2020, UK).

Method 2- Aerogel particles are dispersed in water containing the dispersing agent (0.3 wt. %) and anti-foam additive (0.5 wt. %) and then mixed for 2 hours at 2800 rpm in a mechanical stirrer. Afterward, the resin is added to the dispersion and mixed for 1 hour more at the same rpm.

Figure 1: Image of silica aerogel particles.

Method 3- The dispersing, and anti-foaming agents mixed with resin for 10 minutes at 400 rpm, then, at 800 rpm, the calculated amount of aerogel particles were added to the mixture in three stages, once every 20 minutes and mixed properly [9].

2.3. Evaluation of aerogel dispersion in water

To study the dispersion of aerogel particles in water, a mechanical mixing (400 rpm) for 20 minutes was used. Firstly, 0.5 wt.% of antifoam and 0.3 wt.% of each of the surfactants were added) to water, then, 2 wt.% of aerogel was added to the aqueous solution.

2.4. Scanning electron microscopy

After drying the dispersion of samples containing aerogel particles on hot aluminum foil, the particles were investigated through a scanning electron microscope (Hitachi S-4160, England).

2.5. Zeta potential measurements

Zeta potential in colloidal dispersions is the electric potential in the interfacial double layer relative to a point in the bulk. Zeta potential measurement is one of the important factors in the evaluation of the stability of colloidal materials. For this purpose, the zeta potential of IC3100 and IC3110 samples was measured in a water medium in presence of XD, X100, and GR5M surfactants using a Horiba NanoPartica SZ-100 device (France).

2.6. Evaluation of aerogel/ acrylic dispersion

2.6.1. Particle size measurement

The particle size of the samples and their distribution were measured by a MALVERN, Particle size analyzer, Mastersize 2000, UK (ISO 13320).

2.6.2. Rheological measurements

The rheological properties of the samples were investigated by a Physica MCR 300 device, Anton Paar Co., Austria. In this measurement, first, a pre-run was applied to the samples for 60 seconds. Then, the rheology of the samples was measured from 0.01 to 1000 (1/s) shear rates and then from 1000 to 0.01 in return.

2.7. Thermal conductivity measurement and energetic analysis of coatings

The thermal conductivity of the dried film was measured by an HFM436 device, Netzsch Company. The sample was placed between two hot and cold plates, and the heat flow resulting of the temperature difference was measured using a highly accurate temperature sensor. Thermal transmittance of a wall of building element (U-value) was measured according to IS0 9969:1994 (E). A uniform coating film was applied on concrete. Then the applied samples were kept at room temperature for one week until they were completely dried, and then their thermal conductivity was measured.

3. Results and Discussion

Figure 2 shows the SEM images of two types of aerosol particles in the aqueous dispersion. As the images show, the particles well dispersed and there is no accumulate or flocculation.

To investigate the stability of silica aerogel dispersion in water, the zeta potential of the dispersions was measured. The ionic surfactant created an effective electric charge on the particles by adsorbing on their surface, causing the creation of an electric double layer around the particles, electrostatic repulsion force, and dispersion stability [21, 22]. Table 1 presents the zeta potential of the dispersions.

Table 1: Zeta potential of aerosol dispersions containing different surfactants.

Aerosol/ surfactant	TRITON GR5M (mv)	TRITON X100 (mv)	TERGITOL XD (mv)
IC3100	38.5	31.5	23.6
IC3110	25.5	23.6	19.4

The comparison of the results of Table 1 reveals the better performance of the anionic surfactant than the non-ionic surfactant. Therefore, this anionic surfactant was used in the next experiments.

3.1. Evaluation of aerogel/acrylic dispersion

Figure 3 shows the rheological behavior of acrylic resin in terms of viscosity as a function of shear rates and Figure 4 shows the shear stress as a function of shear rates in reciprocating mode.
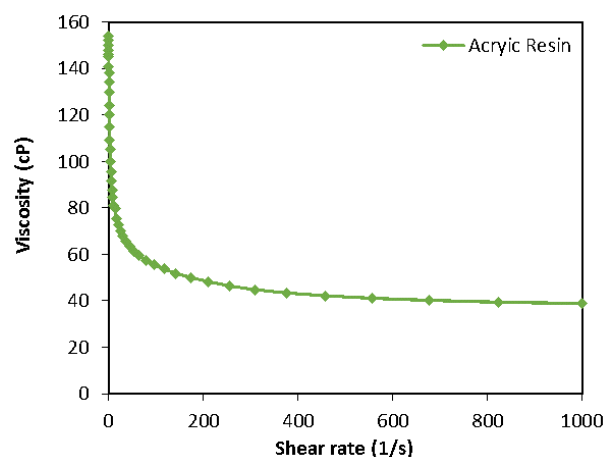

Figure 3: Viscosity of acrylic resin as a function of shear rates.

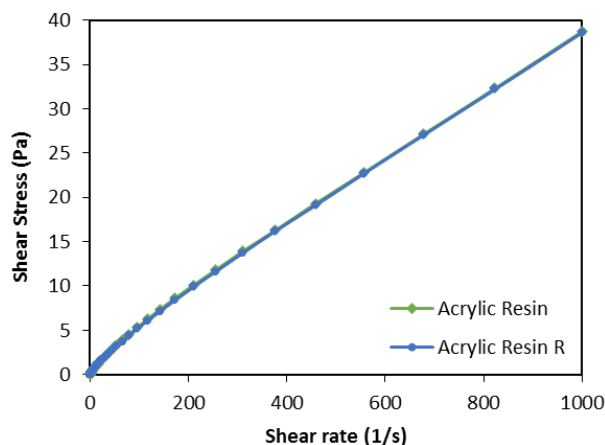**Figure 2:** SEM images of dispersed aerogel particles a) IC3110 and b) IC3100.

Figure 4: Shear stress of acrylic resin as a function of shear rates.

The acrylic resin exhibits shear thinning behavior at a low shear rate (Figure 2). The behavior becomes less effective at higher shear rates, and approaches Newtonian fluids. The shear thinning behavior of the resin at a low shear rate can be attributed to steric immobilization, where the water inside the resin is trapped between the dispersed polymer particles. As the shear rate raises, the mobility of polymer chains increases and the trapped water may release, and the apparent viscosity decreases [23, 24] resulting in the pseudo-plastic behavior of the resin. The shear stress / shear rate diagram in a reciprocating cycle for the acrylic resin is the same, indicating that the rheological behavior of the resin is time-independent and no thixotropic behavior exists.

In the first method of dispersion, 0.5 wt. % of the dispersing agent is added to the acrylic resin, and then 2 and 4 wt. % of each aerogel is added and mixed for 4 hours at 2800 rpm. The result of this method is a paste-like mixture, which may be attributed to the instabilization of the acrylic polymer emulsion at high shears, a structure may form, and the acrylic/aerogel mixture shows a rheopectic behavior [25]. This behavior is not favorable; therefore, changing the dispersing method is necessary.

In the second method, 2 and 4 wt. % aerogel dispersion in water is prepared with the aid of dispersing and antifoam additives and is mixed for 2 hours utilizing a mechanical stirrer at 2800 rpm. Then, the resin is added to the system and mixed for 1 hour more at the same rpm. The resin dispersion made in this way at a concentration of 4 wt. % was again shows high viscosity and paste like dispersion. Figure 5 shows the viscosity diagram of the resin dispersion made by this method at a concentration of 2 wt. % in terms of shear rates for two types of aerogel particles.

Figure 5 shows the shear thinning behavior of aerogel/acrylic dispersion, which can be attributed to steric immobilization and the release of water between the particles at higher shear rates. Additionally, the difference in the rheological behavior of larger particles and smaller can be noticed. Dispersion of larger particles exhibits higher apparent viscosity at the lower shear rates. However, with the increase in the shear rate, the viscosity of the larger particle dispersion decreases remarkably. This behavior can be attributed to the more population of particles in the dispersion of smaller particles. Figure 6 shows the shear stress as a function of shear rates for two types of dispersions

through reciprocating measurement.

The rheological behavior of the dispersion containing IC3100 particles is unstable (Figure 6), revealing the low quality of the larger aerogel particle dispersion in acrylic resin. To disperse smaller particles, in low shear rates until 450 s^{-1}, the dispersion shows shear thinning behavior, as well as the Newtonian behavior of dispersion. It shows a thixotropic behavior of the dispersion.

The high viscosity and the thixotropic behavior of the 4 wt. % aerogel particle dispersion, as well as the unstable rheological behavior of the dispersion containing 2 wt.% of larger particles, once again establish the requirement to change the mixing method. In Method 3, aerogel particles dispersed inside the acrylic resin at a lower rpm and in a shorter time.
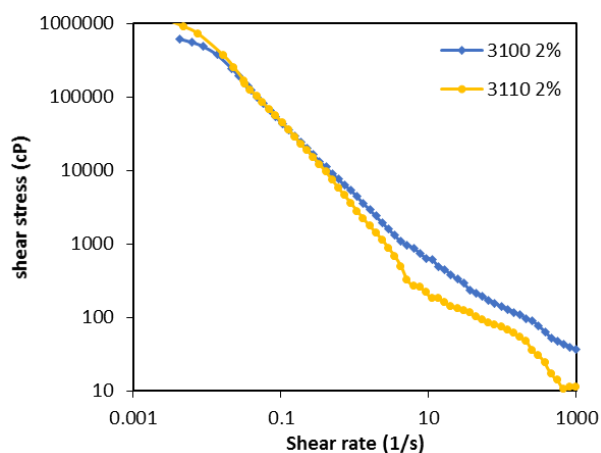

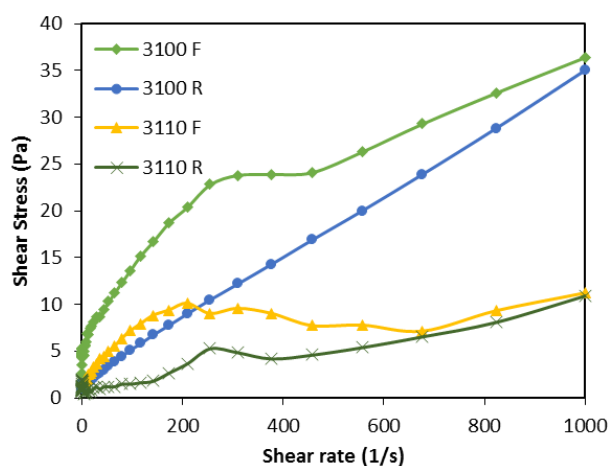**Figure 5:** Viscosity of dispersion (method 2) as a function of shear rates (2 wt.% aerogel).

Figure 6: Shear stress of resin dispersion as a function of shear rates (2 wt.% aerogels was dispersed in resin by Method 2).

First, 0.5 wt.% of the dispersing agent is mixed with the calculated amount of resin for 10 minutes at a speed of 400 rpm, and then mixing was continued at 800 rpm using a mechanical stirrer. In the next step, the calculated amount of aerogel particles was added to the dispersion at three stages and once every 20 minutes. The mixing time in this case was one hour. The prepared dispersion via Method 3 exhibited proper viscosity and stability. Figure 7 shows the viscosity diagram for 4 different dispersions as a function of shear rates.

As Figure 6 shows, the higher aerogel particles, the higher the viscosity. Another point is that the dispersion viscosity of larger particles is higher at very low shears, and then the dispersion viscosity of these particles decreases compared to the dispersion of smaller particles at higher shear rates. Figures 8 and 9 shows the shear stress as a function of shear rates for two dispersions of smaller and larger particles in reciprocating cycles, respectively.

As the rheological behavior of dispersions showed, Method 3 indicated the proper quality of the dispersions. However, the shear thinning behavior is still observed in all samples. The diagrams of shear stress as a function of shear rates in reciprocating cycles are close together for all samples, indicating the reduction of the thixotropic behavior of the dispersions. Hence, the mechanical mixing at a lower rpm and in a shorter time (Method 3) is considered for the next experiments. Table 2 shows the particle size distribution of the 4 wt. % of IC3100 and IC3110 dispersions. Prepared according to Method 3.

Two regions can be distinguished in both IC3100 and IC3110 samples. The first region is between 0.1 and 1 microns, which may have related to polymer emulsion particles, and the second region is related to aerogel particles, the peak of which is visible for IC3100 aerogel at around 35 µm and IC3110 particles

Table 2: Particle size distribution of the resin dispersions.

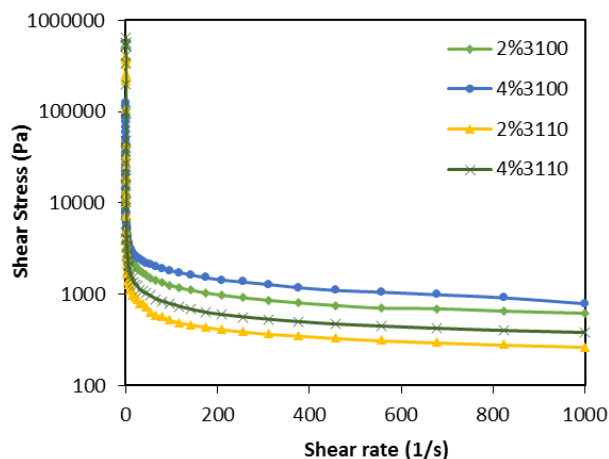| Sample	Area (1)	Peak (1)	Area (2)	Peak (2)
IC3100	− 1 (µ)	200 nm	10-100 (µ)	35 µm
IC3110	− 1 (µ)	200 nm	50-500 (µ)	150 µm
Acrylic resin	− 1 (µ)	200 nm	1-1.5 (µ)	850 nm

Figure 7: Viscosity of resin dispersion as a function of shear rates (2 and 4 wt. % aerogels was dispersed in resin by Method 3).
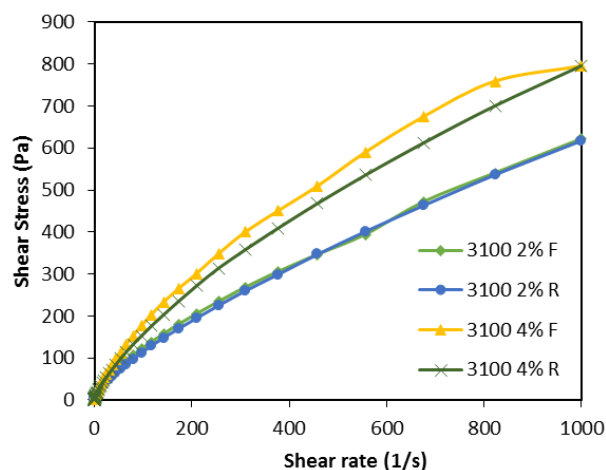

Figure 8: Shear stress of resin dispersion as a function of shear rate (2 and 4 wt. % of 3100 aerogels dispersed in resin according to Method 3)
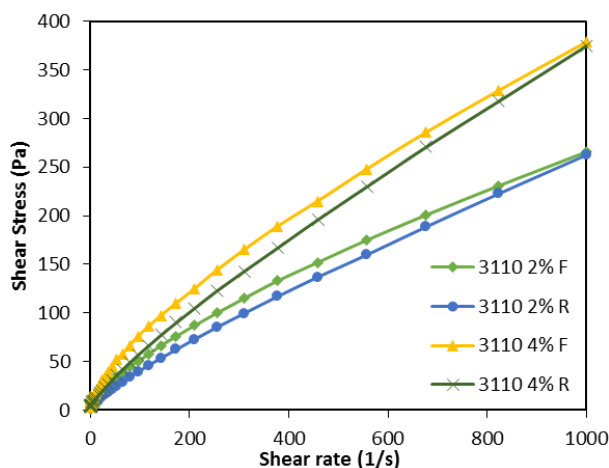

Figure 9: Shear stress of resin dispersion at different shear rates (3110 aerosols with 2 and 4 % weight was dispersed in resin by Method 3).

at around 150 μm. They confirm the size of aerogel particles in powder form before dispersing them in the acrylic resin, indicating the favorable quality of the dispersion for use as thermal insulation coating. Due to the size of resin emulsion particles is larger than the pore size of the aerogel particles, it is not possible for the emulsion to penetrate into the pores and only the aqueous medium will penetrate into the aerogel.

3.2. Thermal conductivity measurement

The thermal conductivity of the dried composite film was measured via the HFM436 device, Netzsch Co. according to the ASTM C518 standard test method. Table 3 represents the results of the thermal conductivity measurements for different coatings with a thickness of 3.8 ± 0.2 mm.

According to Table 3, the thermal conductivity of the acrylic film without any aerogel (Polyfoam 748) is equal to 160 ± 5 mW/mK that is in agreement with the values reported in the similar research [26].

As Table 3 shows, the effect of porous silica particles on the thermal conductivity of the acrylic resin is evident, and the thermal conductivity decreases as a function of the aerogel particles in the film. It can have observed 37 % and 46 wt. % reduction in the thermal conductivity for 6 wt.% of IC3100 and IC3110 aerogels in dry composite coating respectively. The performance superiority of IC3110 aerogel particles, with an average particle size ten times larger than IC3100, was evident for all samples.

This finding has also been confirmed in another study [11], in which the thermal properties of the epoxy aerogel composite were studied, and two aerogels of different sizes, one with a particle diameter smaller than 0.2 mm and the other with a particle diameter between 0.2 and 2 mm, were used. The larger particles exhibited better thermal performance than the smaller particles. In Zhao's study, this behavior is attributed to the penetration of epoxy into the pores of aerogel particles. The study assumed that the composite was made of three parts: an epoxy matrix, an interface containing penetrated resin in aerogel pores (shell part), and an aerogel core free from any penetrated resin or medium.

Based on this model, the penetration length of the epoxy matrix into the aerogel is independent of the size of the aerogel particles and is considered the same for both aerogels. The aerogel core of larger particles, resulting in the better thermal performance of the

Table 3: Thermal conductivity of the coatings.

Aerosol based composite	wt. %	Thermal conductivity (mW/mK) ±5
Blank	-	160
IC3100	2	135
IC3100	4	116
IC3100	6	101
IC3110	2	126
IC3110	4	101
IC3110	6	87

particles. This study [11] does not report the average pore size for each of the two aerogels.

3.3. Energetic analysis

As mentioned, in order to measure the U-value (thermal transmittance), the coating film was applied on a flat concrete with a thickness of 20 cm (30×30 cm Length and width). The coating was applied with a thickness of 1.5 mm. The thermal conductivity of concrete substrate was measured via HFM device, and calculated as 23 $mWm^{-1}K^{-1}$. Therefore, its thermal resistance was 0.97 m^2KW^{-1}. After applying the coating on the substrate, the coating film also behaved as a thermal resistance, which is in series with the thermal resistance of the concrete substrate.

Therefore, R_{total} in the above equation, contact resistance, can be written as follows (Eq. 1):

$$R_{total} = R_{coating} + R_{concrete} + \text{TCR} \qquad (1)$$

TCR is the contact resistance between the coating film and the substrate. To determine the resistance of the coating film accurately by considering the contact resistance, each measurement can be performed twice and with two different thicknesses of the film as reported in the other research works [27, 28]. In this case (Eqs. 2 and 3):

$$R_{total1} = R_{conccrete} + R_{coating1} + \text{TCR} \qquad (2)$$

$$R_{total2} = R_{concrete} + R_{coating2} + \text{TCR} \qquad (3)$$

By subtracting the above two equations and assuming the contact resistance to be equal in the two measurements, the thermal conductivity of the coating

film is determined. Based on the experimental results, applying a coating containing 6 wt. % IC3100 aerogel can increase the thermal resistance up to 42 % and reduce the U-value by 24 %, which consequently reduces energy consumption in the buildings and saves it.

4. Conclusion

We can conclude that:

I. The anionic surfactant, sodium sulfosuccinate esters, is a much more efficient than the nonionic surfactants in dispersing aerogels in waterborne acrylic resin

2. Rheological measurements showed that the mechanical method with low intensity and a shorter time is more sufficient for dispersing aerogel particles in waterborne acrylic resin.

3. The presence of aerogels has a significant effect on the thermal conductivity of acrylic coating. The higher amount of aerogels, the lower thermal conductivity of the coatings. The results show 37 and 46 % reduction in thermal conductivity for smaller and larger aerogel particles in the coatings, respectively.

4. Based on the experimental results, the thermal transmittance (U-value) for a coating containing 6wt.% aerogel IC3100 can reduced by 24 %.

5. The dispersion of porous nano silica was prepared with optimum dispersing property and thermal insulting behavior.

5. References

1. M. Pedroso, I. Flores-Colen, J. D. Silvestre, M. Glória. Gomes, L. Silva, L. Ilharco, Physical, mechanical, and microstructural characterization of an innovative thermal insulating render incorporating silica aerogel, *Energy Build.*, 211(2020), 109793-109804.

2. M. Balarin, O. Gamulin, M. Ivanda, M. Kosović, D. Ristić, M. Ristić, S. Musić, K. Furić, D. Krilov, J. Brnjas-Kraljević, Structural, optical and electrical characterization of porous silicon prepared on thin silicon epitaxial layer, *J. Mol. Struc.*, 924(2009), 285-290.

3. H. Maleki, L. Duraes, A. Portugal, An overview on silica aerogels synthesis and different mechanical reinforcing strategies, *J. Non-crystalline Solid.*, 385(2014), 55-74.

4. R. Baetens, B. P. Jelle, A. Gustavsen, Aerogel insulation for building applications: a state-of-the-art review, *Energy Build.*, 43(2011), 761-769.

5. G. Wei, Y. Liu, X. Zhang, F. Yu, X. Du, Thermal conductivities study on silica aerogel and its composite insulation materials, *Inter. J. Heat Mass Trans.*, 54(2011), 2355-2366.

6. F. Raoufi, Z. Ranjbar, S. Rategar, E. Nowak, B. Nazari, Wettability study of super-hydrophobic silica aerogel powders, *Prog. Color Colorants Coat.*, 13(2020), 75-83.

7. J. Gu, R. Fu, Sh. Kang, X. Yang, Q. Song, Ch. Miao, M. Ma, Y. Wang, H. Sai, Robust composite aerogel beads with pomegranate-like structure for water-based thermal insulation coating, *Cons. Buil. Mater.*, 341(2022), 127722-127733.

8. S. Achar, J. Procopio, Developments in waterborne thermal insulation coatings, *J. Pro. Coat. Lin*, 27(2013), 48-59.

9. F. Raufi, Dispersion of silica aerogel particles in water-based acrylic resin for use in Heat insulation coatings, Ph.D. thesis, Institute for Color Science and Technology, Iran, 2019.

10. S. Kiil, Drying of latex films and coatings: Reconsidering the fundamental mechanisms, *Prog. Org. Coat.*, 57(2006), 236-250.

11. J. Pidhurney, P.F. Pescatore, Aerogel for highly thermally insulative coatings, *J. Coat. Technol.*, 9(2012), 46-48.

12. G. Stuart Burchill, Composition for Thermal Insulating Layer, United States Patent, patent no. US 7,144,522 B2 Dec. 5, 2006.

13. Y. Liao, Xi. Wu, Zh. Wang, R. Yue, G. Liu, Y. Chen, Composite thin film of silica hollow spheres and waterborne polyurethane: Excellent thermal insulation and light transmission performances, Mater. Chem. Phys., 133(2012), 642-648.

14. J. Zhao, D. Ge, S. Zhang, Xi. Wei, Studies on thermal property of silica aerogel/epoxy composite, *Mater. Sci. Forum*, 546-549(2007), 1581-1584.

15. F. He, Z. Qi, W. Zhen, G.Wu, Y. Huang, Xe. Xiong, R.Zhang, Thermal conductivity of silica aerogel thermal insulation coatings, *Inter. J. Therm.*, 40(2019), 92-99.

16. V. Yu Chukhlanov, O.G. Selivanov, T. A. Trifonova, M. E. Ilina, N. V. Chukhlanova, Thin-layer thermal insulation coatings based on high-filled spheroplastics with polyorganosiloxane binder, IOP Conference Series: Earth and Environmental Science, 90(1):012061.

17. M. Bahrami, Z. Ranjbar, R. A. Khosroshahi, Sh. Ashhari, Investigating corrosion protection properties

of epoxy thermal insulators through cyclic corrosion test, *Prog. Org. Coat.*, 113(2017), 25-30.

18. Q. Kang, Y. Bao, M. Lia J. Ma, Effect of the wall thickness of hollow TiO$_2$ spheres on properties of polyacrylate film: Thermal insulation, UV-shielding and mechanical property, *Prog. Org. Coat.*, 112(2017), 153-161.

19. S. Kill, Quantitative analysis of silica aerogel-based thermal insulation coatings, *Prog. Org. Coat.*, 89(2015), 26-34.

20. RT. Pugh, Dispersion and stability of ceramic powders in liquids. L (eds.) surface and colloid chemistry in advance ceramics processing, surfactant science series, Vol. 51, Chapter 4. Marcel Dekker, New York (1944).

21. T. Sato, R. Ruch, Stabilization of colloidal dispersions by polymer adsorption. surfactant science series, Vol. 9, Chapter 2. Marcel Dekker, New York (1980).

22. D. T. Nguyen, Use of novel polyetheralkanolamine comb polymers as pigment dispersants for aqueous coating systems, *J. Coat. Technol. Res.*, 4(2007), 295-309.

23. Y. Zhou, D. Yu, C. Ling Wang, Sh. Lin Chen, Effect of ammonium salt of styrene-maleate copolymer on the rheology of quinacridone red pigment dispersion, *J. Dispersion Sci. Technol.*, 25(2004), 209-215.

24. H. A. Barnes, Thixotropy a review, J. Non-Newtonian Fluid Mech., 70(1997), 1-33.

25. J.D. Muzzy, Thermoplastics – properties, thermoplastics-properties, in: A.Kelly, C. Zweben (Eds.), Comprehensive Composite Materials (6 vols.), vol. 2, Elsevier Science, Amsterdam, 2000, Chapter 2.

26. A. Hoseini, C. McCague, M.Andisheh-Tadbir, M. Bahrami, Aerogel blankets: From mathematical modeling to material characterization and experimental analysis, *Inter. J. Heat Mass Trans.*, 93(2016), 1124-1131.

27. M. Rouhani, W. Huttema, M. Bahrami, Effective thermal conductivity of packed bed absorbers: Part 1 – Experimental study, *Inter. J. Heat Mass Trans.*, 123(2018), 1204-1211.

PROGRESS
IN COLOR, COLORANTS AND COATINGS

CONTENTS